Relieving Loading on Tidal Turbines Operating in a Turbulent Environment

Proposal for Load Alleviation Device for a Marine Turbine

Sarah Rosaline Garden

School of Energy, Environmental Technology and Agrifood

Cranfield University

This dissertation is submitted for the degree of

Masters by Research

May 2016

Abstract

Tidal turbines operate in marine currents characterised by strong turbulence. This environment impacts on the life of the device, blades, transmission and running train ancillaries, bearings and seals, for example. The reduction of the transient load on the turbine blade can be achieved through a range of measures; in this investigation, modifications to the blade comprising blowing actuators will be modelled using the FLUENT CFD RANS solver with the k-ω SST turbulence model.

Different locations on the suction side for the blowing are explored. Different angles and pressures of the blowing are explored for steady state cases. The final chosen location for the ejection was near the trailing edge (TE) for unsteady simulations with sinusoidal jet excitation and an oscillating-flow inlet boundary condition.

The most obvious effectiveness is at low actuation frequency and mid-to-high jet-strength. This results in reduction of lift at the higher angles of attack, α, and reduction of $\frac{\Delta L}{\Delta \alpha}$. The action of the unsteady ejection re-shapes the hysteresis lift curve with little change in drag and reduces drag in some cases. A counter-rotating pair of vortices is formed due to the TE ejection, which altered the direction of flow leaving the TE due to a small region of induced recirculating flow behind the TE. One of the vortices takes the form of a curtailed TE vortex. It is thought that this could, under the right conditions, be caused to merge with the wake and shed to result in a more docile stall.

The CFD validation study performed first of all, consisted of a comparison between the two relative types of motion - a pitching aerofoil and static aerofoil subjected to flow oscillation. This study uncovered substantial differences in the dynamic stall mechanics between wind tunnel experiments on a pitching aerofoil and the kind experienced by a turbine blade due to oscillating loads in highly unsteady flow. Many wind turbine data currently depends on the relative motion between aerofoil and flow.

Acknowledgements

First and foremost, I would like to sincerely thank my supervisor Joao Amaral Teixeira who has gone above and beyond in supporting me, such as I could never have expected of a supervisor. His knowledge, humour, zeal, helpful insight, encouragement and tireless patience made the completion of this thesis possible.

I would like to express my gratitude to and to acknowledge the contribution of Luca Camosi. Thanks to him early on, for helping me get the work off the ground, then for long nights spent fine-tuning the model. Also for giving me a crash course in MATLAB and the joys of automating many things. His generosity with his knowledge and skill was much appreciated.

Heartfelt thanks also go to my loving parents Eva and Ken and sister Samantha who supported me through thick and thin. Also to Ted, our most cherished cat.

Table of contents

List of figures

List of tables

Nomenclature

Roman Symbols

b turbine blade length (variable blade length)

C Courant number, C (language)

c aerofoil chord

C_D or C_d drag coefficient

C_L or C_l lift coefficient

C_Lhys hysteresis lift

C_Lmax maximum lift coefficient reached before stall

C_max maximum Courant number

C_m pitching moment coefficient

C_p pressure coefficient

C_k/C_ω dissipation of k/ω

D a characteristic length

D_k/C_ω cross diffusion term of k/ω

E a source term

F blending function

f frequency

k reduced frequency or turbulent kinetic energy in k-ω model

L sectional lift

M piching moment about an axis of rotation

n flow velocity (variable speed rotor)

P, p pressure

$P_k/\omega/\gamma$ production of $k/\omega/\gamma$

Re Reynolds number

Re_θ momentum thickness Reynolds number

Re_c chord Reynolds number

S strain rate (or strain rate magnitude if unsubscripted), or source term, depending on context

$t_{\max}$ maximum thickness

T period (of oscillation)

U, u velocity

U_∞ freestream velocity - flow velocity a distance far enough away from any interference, or the unaffected direction of the stream

W Work

y^+ 'Y plus' - nondimensional distance from first grid point to the wall

Greek Symbols

α angle of attack (degrees)

$\alpha_{\max}$ angle of attack at which maximum lift reached

α_0 initial angle of attack

α_0 (α_{mean}) mean angle of attack

α_1 amplitude of oscillation

Δ change or difference

δ_{ij} Kronecker Delta Function

ε turbulent dissipation rate

Γ diffusion coefficient

γ intermittency

μ dynamic viscosity

μ_T turbulent- or eddy- viscosity

Ω vorticity

ω angular frequency or specific dissipation rate in k-ω model

ϕ phase, flow angle

ρ air density

σ turbulent Prandtl number

τ_w skin friction

τ shear stress, or time delay, depending on context

τ_0 pitch-damping coefficient

θ (θ_{pitch}) blade incidence angle (variable pitch angle)

Subscripts

0 initial

a axial

c chord

∞ condition upstream

max maximum

rel relative

rot rotor

Other Symbols

$\vec{A}$ surface area vector

$\nabla \times v$ curl of velocity vector

$\nabla \cdot v$ divergence of velocity vector

∇^2 Laplace operator

$\hat{n}$ unit normal

$\mathbb{R}$ the set of real numbers

$\vec{u}$ velocity vector

Acronyms / Abbreviations

(A)(P)FC (Active)(Passive) Flow Control

AoA Angle of Attack (British Angle of Incidence)

APG Adverse Pressure Gradient

(L)(T)BL (Laminar)(Turbulent) Boundary Layer

BC Boundary Condition

BEM Blade Element Momentum

BL(C) Boundary Layer (Control)

CAD Computer-Aided Design

CFD Computational Fluid Dynamics

CFJ Co-Flow Jet

CFL Courant-Friedrichs-Levy condition

DS(V) Dynamic Stall (Vortex)

EVM Eddy Viscosity Model

FST(I) Free Stream Turbulence (Intensity)

FT Fourier Transform

HA[WT] Horizontal Axis [Wind Turbine]

HWA Hot Wire Anemometry

IC Initial Condition

LDV Laser Doppler Velocimetry

LE Leading Edge

LSB Laminar Separation Bubble

MC Mid-Chord

MCT Marine Current Turbine

NACA National Advisory Committee for Aeronautics

NPL National Physical Laboratory

NREL National Renewable Energy Laboratory

NWTC National Wind Technology Centre

RA(NS) Reynolds-Averaged (Navier-Stokes) equations

OSU Ohio State University

PDE Partial Differential Equation

PIV Particle Image Velocimetry

RSM Reynolds Stress Model

SP Separation point

SST Shear Stress Transport

TE Trailing Edge

TKE Turbulent Kinetic Energy

TSR Tip Speed Ratio

TVR Turbulent Viscosity Ratio (a.k.a. eddy viscosity ratio)

UDF User Defined Function

URANS Unsteady RANS (Reynolds-Averaged Navier-Stokes equations)

Chapter 1

Introduction

1.1 Introduction

To create a sustainable and stable energy economy, there need to be a range of renewable energy technologies for low-carbon electricity generation, even if they require long-term development. While the wind energy sector is burgeoning, there are a number of hindrances in the way of offshore renewables. Tidal stream, wave power and offshore wind meet additional problems: with planning, transmission and grid connection, and last but not least, structural stability. *Turbulence* and *dynamic stall* are two phenomena which affect turbine performance. Turbulence consists of chaotic property changes of fluids, such as air and water, which include fluctuations in pressure and velocity components over space and time.

Turbulence, or turbulent flow, occurs near the coast, near the seabed, and in tidal channels, where marine turbines are moored. It occurs when a jet stream (tidal stream) interacts with slower surrounding fluid, or when water swirls close to the seabed near the coast, causing mixing of the fluid. Turbulent mixing relates to the amount of diffusion and convection of flow properties such as momentum and energy. Transportation of these properties occurs by the action of eddies - transient vortices which appear on many scales and interact with each other. The *transition* from laminar to turbulent flow is thus defined at the point where this mixing first takes hold.

For a solid structure, such as a turbine blade, turbulence affects the lift and drag, both in magnitude and distribution and thus inflicts gust loads which impact adversely on turbine design.

For structural stress evaluation, load variations with respect to time are very important and fluctuating and alternating loads must be considered against the fatigue life of a bladed

structure. A load alleviation method is needed to minimise the fatigue life-extraction and to reduce excessive loads which affect the rotor and surrounding components.

1.2 Dynamic Stall & its Effect upon Fatigue

Dynamic stall (DS) is a phenomenon whereby an aerofoil pitching upwards relative to the freestream direction of flow experiences a delay in the onset of stall, along with a prolongation of *flow attachment* and higher lift than can be obtained quasi-statically. The lift coefficient rises until DS occurs.

A steep *adverse pressure gradient* forms on the upper side. When this gradient is large enough that the turbulent boundary layer (TBL) cannot penetrate it, *flow reversal* (which first occurs near the wall at 'incipient detachment') - or *separation*- and stall occurs.

The aerofoil also undergoes delayed *transition* from laminar to turbulent flow, which precedes BL *separation* and subsequent stall. Stall happens at a larger angle of attack (AoA) than the critical AoA and proceeds to a non-linear loss of lift until flow *reattaches* once the aerofoil returns to a lower α, a safe distance from the static stall limit.

Dynamic stall is different from *static stall* because of the many dynamic effects involved. One of the main ways dynamic stall differs is by the *shedding* of vortical structures. These pass over the upper surface of the aerofoil, or *suction side*, distorting the chord-wise loading i.e. *pressure distribution*. This can cause severe loading of the device, resulting in energy losses and degradation of the material over time.

The classic criterion for steady separation (which is associated with the static stall) is the vanishing of the skin friction coefficient at the wall. This is no longer valid in unsteady flow. Instead, the point of zero skin-friction oscillates along the aerofoil surface, generating a thin layer of reverse flow.

Due to increasing α the *stagnation point* moves aft of the leading-edge (LE) on the lower side and so the flow has a larger region of curvature to accelerate. An increase in velocity corresponds to a decrease in pressure about the LE and precipitates the growth of an adverse pressure gradient (APG) due to incidence, a bit further upstream of the LE.

At the point where the flow separates - the separation point (SP) - the shear stress is zero. Proceeding into the area of recirculating flow, the shear stress becomes negative. A shear *layer* is formed, and this shear layer rolls up into a vortex and convects downstream. This is called the 'dynamic stall vortex'.

DS can occur in turbulent conditions, in which a stationary aerofoil experiences a relative pitching motion due to an oscillating relative flow velocity vector. The configuration can be reproduced on a pitching aerofoil in a 2D flow, but, as it is one aim of this study to show, the

two are fundamentally different. Much unsteady wind turbine data currently depends on the relative pitching motion idea.

The forces on an aerofoil stem mainly from the pressure distribution. The force found from integrating the pressure has a lift and drag component. The drag coefficient is composed of two parts: one is the skin friction (shearing stress) component, which comes from the viscous surface stresses around the aerofoil; the other is the 'form drag', also known as the BL normal pressure drag, or simply 'pressure drag'. It comes from the fore and aft imbalance in the pressure distribution around the aerofoil. At low α, skin friction dominates the total drag, while the pressure drag component is minor. The form drag becomes very large when the aerofoil stalls as a result of BL separation, effectively altering the shape of the foil.

1.2.1 Literature Review

Carr [1] made a detailed review of the progress made on dynamic stall in the latter half of the 20^{th} century. While dynamic stall is primarily a three-dimensional phenomenon, as is turbulence, considerable insight can be gained by approximating the condition of two dimensions using a high aspect-ratio wing plan of constant cross section, spanning the width of a rectangular wind tunnel, and taking data measured in the mid-span plane, with suitable corrections made for the angle of attack. Local 2D data for the forces can be used in this way [2].

WT blades are long and slender structures where the spanwise velocity component is much lower than the streamwise component, and it is thus assumed in many aerodynamic models, that the flow at a given radial position is two dimensional and that 2D aerofoil data can thus be applied.

Variables which affect dynamic stall include aerofoil shape, freestream velocity (the velocity that would exist if the aerofoil were not there: the uninterrupted relative flow velocity vector), stream turbulence and Reynolds number.

Steady-state studies and quasi-steady aerodynamic hysteresis

Somers [3] conducted steady-state 2D experiments on an NREL thick wind turbine aerofoil, the S809, at Reynolds numbers ranging from 1.0×10^6 to 3.0×10^6. The angle of attack was increased from 0° until the entire upper surface was separated and then decreased to determine the extent of *hysteresis*. The same was done for negative angles of attack, whereby the author shows that there exist laminar-turbulent transition regions on both the upper (suction) and lower (pressure) surfaces.

For some aerofoils the performance data depend on whether the aerofoil is going in the direction of increasing or decreasing angle of attack, i.e. the data are dependent on the sense of change of the angle of attack.

Hysteresis is the dependence of the output of a system, not only on its current input, but also on its history of past inputs. It is a concept that appears in other areas of the physical sciences, such as magnetism [1]. Hysteresis is also seen in the flow of liquids through porous media: the hysteresis in this case is similar to porous media, as an obstruction causes a fluid particle to 'choose' a flow path, and be beset with viscous and inertial resistance (caused by local accelarations). This aerodynamic hysteresis is observed for AoAs close to the static stall angle.

An LSB (laminar separation bubble) was found by Somers to be the mechanism of laminar-turbulent transition on the upper surface and the same for the lower surface [2]. The separated laminar BL reattaches as the turbulent BL: the transition to turbulence has occurred inside the bubble, in the detached shear layer - this is "separation-induced" transition [4].

The study traced the LSB using pressure distributions (C_p). The LSB/transition location were captured using photographs of oil coating on the surface and a microphone as the choice of 'visualisation'. The oil coating photographs revealed the size and location of the LSB, as it revealed roughly the laminar separation and turbulent reattachment locations. Where the two locations were indistinguishable this was simply marked 'transition'. The microphone could detect turbulent 'bursts' of attached turbulent flow and thus detected the turbulent reattachment point after the LSB. Hence it was the turbulent reattachment point that defined the transition location as this was measurable using this technique.

Mittal and Saxena [5] conducted a numerical study, for a NACA 0012 at $Re = 1 \times 10^6$, to track the hysteresis loop in the aerodynamic data close to the static stall angle. They used the RANS equations in conjunction with the Baldwin-Lomax turbulence model for closure. Stabilizing terms based on element-level integrals of the residuals were added to stabilize computations against spurious numerical oscillations which manifest in advection-dominated flow. For angles ranging from 0° to 20°, they found hysteresis for the range $17^\circ < \alpha < 19^\circ$.

[1] In magnetism, when a ferromagnetic material is placed in a $\vec{B}$ (magnetic) field with one direction, it will not go back to zero magnetisation in the absence of the $\vec{B}$ field, as a large fraction of the saturation field is retained. The electric dipoles stay in position in cells called *magnetic domains*. Instead the magnetisation of the material must be driven back to zero by a field in the opposite direction. If this process were applied by way of an alternating $\vec{B}$ field a *hysteresis loop* would be traced.

[2] The 'laminar separation bubble' involves the laminar BL separating slightly (the thin vortex layer develops a shear layer) from the aerofoil upper surface. The flow reattaches to the body, resulting in the said 'bubble' between the separation and reattachment points. The formation of an LSB is more associated with low-Reynolds-number aerofoils, but this aerofoil has a relatively high design Reynolds number of 2×10^6. *Complete separation* takes place when the BL fails to reattach.

The authors note that the flow ceased to be steady beyond 17° (beyond this the aerofoil is in stall-state) and vortex-shedding was observed. The hysteresis was clockwise in the lift coefficient profiles and counter-clockwise in the drag coefficient profiles, indicating that this stall state persisted through decreasing α.

Figure 1.1, appropriated from the paper, shows pressure and vorticity contour plots at the same α: first from and second from top, vorticity and pressure at 18°, 'increasing'; first from and second from bottom, pressure and vorticity at 18°, 'decreasing'. These are fully-developed unsteady solutions of the flow field for a static aerofoil at 18°.

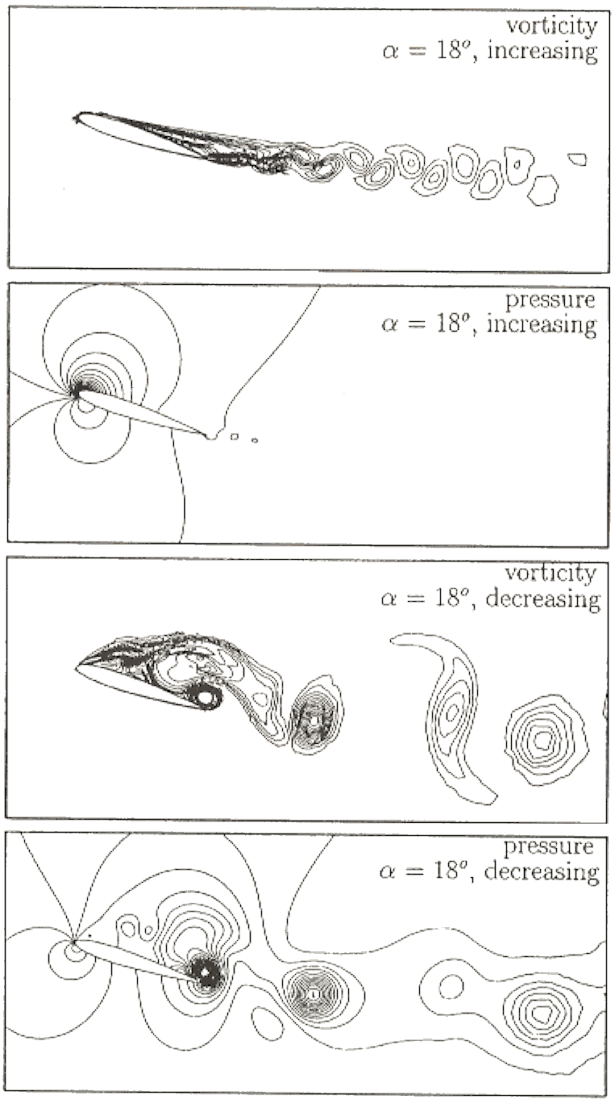

Fig. 1.1 Re=10^6 flow past a NACA 0012 aerofoil at AoA of 18°: vorticity and pressure fields for the computed solutions obtained with increasing and decreasing AoA. From Mittal and Saxena [5]

A comparison was made between resulting fully-developed unsteady solutions for one α (=20°) whereby the following two initial conditions were applied: computations were initiated using the steady-state solution at the respective AoA for $Re = 10^2$. Re was then ramped-up to 10^6 over 500 timesteps and the turbulence model then switched on. This was compared with the use of, for α, a fully developed flow-field solution for the preceding α, as the initial condition - approximating the situation where wind tunnel data for a static aerofoil are collected by increasing α incrementally. They found that the fully-developed unsteady solutions arising from the two different ICs were the same. They proceed by using the latter IC method, using the 20° solution data for 19° and soforth, when collecting data for the decreasing angle branch. Regarding the hysteresis, however, in seeming contradiction to their finding, they later conclude that 'it is the initial condition that is responsible for the multiplicity of solution'.

The results, the authors say, look qualitatively similar to those reported by Hoffman for experiments with the NACA 0015 at low free stream turbulence (FST). Hoffmann [6] shows that hysteresis in the 'steady' data for a NACA0015 is observed for low FST but disappears for high FST, which seems counterintuitive.

The higher the FST intensity, the more this penetrates into the LBL by means of the combined action of turbulent diffusion and pressure fluctuations, which trigger the process of transition to a turbulent state. This transition process is said to be of "bypass" type, in contrast to the "natural" type occurring at low FSTI, in which case transition is caused by growth of unstable waves called "Tollmien-Schlichting" waves.

There is more of a delay transitioning from turbulent-to-laminar than vice versa. In contrast, a separated boundary layer transitions rapidly back to turbulence. The separated flow is more sensitive to disturbances; it is unstable, while turbulent flow is a more stable flow regime.

Yang et al. [7] conducted a detailed steady-state study to determine the steady-state hysteresis of a low Reynolds number aerofoil - the NASA low-speed GA(W)-1 (also labelled NASA LS(1)-0417).

Pressure coefficient (C_p) distributions at several AoAs were measured using a pressure acquisition system. The team took PIV measurements to obtain details of the flow-field such as streamlines of the mean flow-field, TKE distribution and spanwise vorticity - derived from the instantaneous velocity vectors.

Following the theoretical work of Russell [8], the authors use a schematic for finding the locations of critical points (separation, transition, and reattachment points) from the measured surface pressure profiles (see figure 1.2). They, too, find the aerofoil is in stall state during the decreasing α branch of the hysteresis loop. Flow separation from the upper

surface also caused a recirculation region in the wake, resulting in an aerodynamic drag-force acting on the aerofoil.

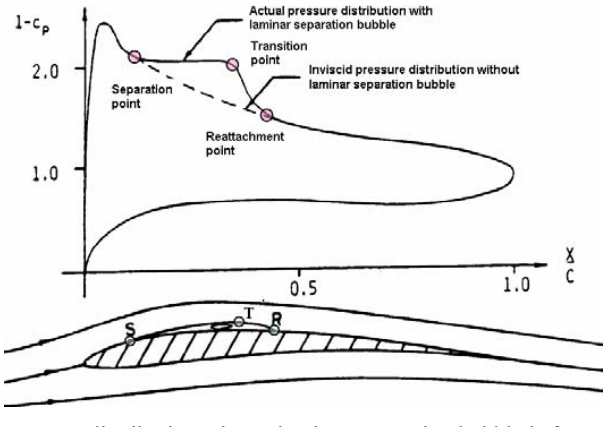

Fig. 1.2 Typical surface pressure distribution when a laminar separation bubble is formed. From Russell [8]

Unsteady oscillating aerofoil studies and highly-unsteady hysteresis

Ramsay et al [9] examined unsteady behaviour by oscillating the same aerofoil as Somers [3], an S809 model, about three mean angles, at three frequencies and with two amplitudes, $\pm 5^\circ$ and $\pm 10^\circ$ for four different Re. Stall was delayed while the AoA was increasing. For both amplitudes higher C_{Lmax} were reached than the steady state values; for the larger amplitude higher C_{Lmax} than the smaller amplitude were attained. Hysteresis loops were found to be larger for the higher reduced frequencies and for the larger amplitude oscillations. Here there is a periodicity imposed on the movement of the aerofoil; this therefore impacts on the flow passing over and around the aerofoil, and hysteresis is an inevitable consequence.

The parameter known as the reduced frequency, k, is:

$$k = \frac{c\omega}{2U_\infty} \tag{1.1}$$

It is defined as the ratio of the physical frequency of the flow oscillation, ω, multiplied by half-chord $c/2$, to the average flow velocity. Reduced aerofoil frequency is used to quantify the speed of the oscillations or vibrations. It represents the portion of the oscillation cycle elapsed during the time it takes the local flow to travel half a chord length. It is an important parameter when analysing performance during DS.

It is the dimensionless number used in general for the case of unsteady aerodynamics and defines the degree of unsteadiness (The other dimensionless number mentioned thus far,

Re, will be discussed in 2.6). In wind engineering it is commonly considered that a $k > 0.02$ results in unsteady effects and for wind turbines, reduced frequencies k in the range 0.035 to 0.12 are typical of normal operation.

It is also said by McCroskey et al. [10] to have significance for the phase of the dynamic stall - which relates to the portion of the cycle in which events take place. It is discussed by the authors, that both the strength and phase of the dynamic forces depend upon k ([3]). Increased k was seen to cause a delay in the phase of the dynamic stall. This is observed in the results for this study, visited in Chapter 3.

The study by Pereira et al. [11] validate a classical Beddoes-Leishman DS model against unsteady thick aerofoil data (2D), to assess load prediction for a HAWT environment. They then adapt the DS model to full-scale MEXICO (Model Rotor Experiments under Controlled Conditions) wind turbine data. They describe a condition of DS as being that a high enough k be met, and that a $k > 0.2$ means that the 'unsteady terms will begin to dominate the behaviour of the airloads' [11, p.208], and consequentially that the problem is highly unsteady. They use the OSU data from [9] for another NREL aerofoil, the S825 in their validation study and find close agreement.

A modified DS model for low-Mach numbers was developed by [12]. Two objectives were to justify the suitability of the low-speed DS model and to provide the relevant parameters for the NREL aerofoils. Airloads caused by separated flow are analysed using Kirchhoff's circulation theory.

McCullough and Gault [13] detail three general types of low speed stalling characteristics, originally classified by B. Melvill Jones [14] (who is also credited with first discovering the laminar separation bubble). These are:

1. Trailing-edge stall (preceded by movement of the turbulent separation point forward from the trailing edge with increasing angle of attack)

2. Leading-edge stall (abrupt flow separation near the leading edge generally without subsequent reattachment)

3. Thin-airfoil stall (preceded by flow separation at the leading edge with reattachment at a point which moves progressively rearward with increasing angle of attack)

(The turbulent separation point is where the streamlines of the mean flow separate from the aerofoil upper surface.) McCullough and Gault highlight the insight that can be gleaned from observing the processes of BL separation in 2D flow fields. The purpose of the study

[3] It was also observed by McCroskey et al. [10] that the maximum value of the lift also increased with an increase of k within the range $0.05 < k < 0.15$.

was to undertake an investigation of aerofoil characteristics - BL and stalling - to provide basic data for a BLC application. The study draws on the authors' previous studies of other aerofoil sections to illustrate the three *general* types of stall.

Most thick aerofoils, such as the S809, undergo TE stall. In TE stall, separation starts at the TE, the separated region propagates forward and at maximum lift the flow is separated over the rear half of the aerofoil. There is a gradual loss of lift as opposed to the sudden loss of lift experienced by an aerofoil undergoing LE stall (such as the S825). At the LE the highest and lowest pressures occur, and the most striking aerodynamic effects of the aerofoil take place. In LE stall, separation starts from the LE (hence the LSB is very close to the LE), and the entire BL may separate simultaneously due to the steep pressure gradients there (which is why LE stall is more sudden and serious when in flight). LE stall is triggered in some cases by what is referred to in the literature as a 'bursting' of the laminar separation bubble. Wang et al. [15] correct this terminology in that there is no sudden split, but rather that the leading edge bubble is induced to shed smaller vortices from time to time.

The peak of the lift curve for TE stall is rounded and the loss of lift, as well as the increase of pressure drag after the stall - form drag - is gradual - a soft stall is observed. The observations of TE stall made in this paper will be compared to the simulation results encountered in Chapter 3.

Wernert et al. [16] use laser-sheet visualisations and a PIV system to take recordings of a NACA 0012 (which experiences LE stall) during upstroke and downstroke pitching motions of the model, with a k of 0.15. As an example of the real-time effect of *unsteady* hysteresis, two of the plots of velocity vector-field streamlines - which are compared with numerical predictions - from their paper are shown. The aerofoil at 15 deg on the upward stroke, figure 1.3 , then at 15 deg on the downward stroke, figure 1.4.

Figure 1.4 shows the shedding of two counter-rotating vortices in this example, meaning that DS has taken place, and a video movie was obtained using a method to capture areas of reversed flow.

The paper is an important example of experimental and numerical work concerning DS. However the numerical results assume fully turbulent flow on the aerofoil. The authors mention the importance of vorticity for interpretation of unsteady, separated flowfields, and also the cycle-to-cycle irreproducibility of the flowfield during the phase of massive separation on which they base a subsequent paper. Although they also mention that the upwards stroke formation of the dynamic stall vortex is reasonably reproducible in space and time from cycle to cycle.

Greenblatt and Wygnanski [17] summarise data of experiments on steady incompressible separation control on the NACA 0012 and the 0015, which are two symmetric aerofoils

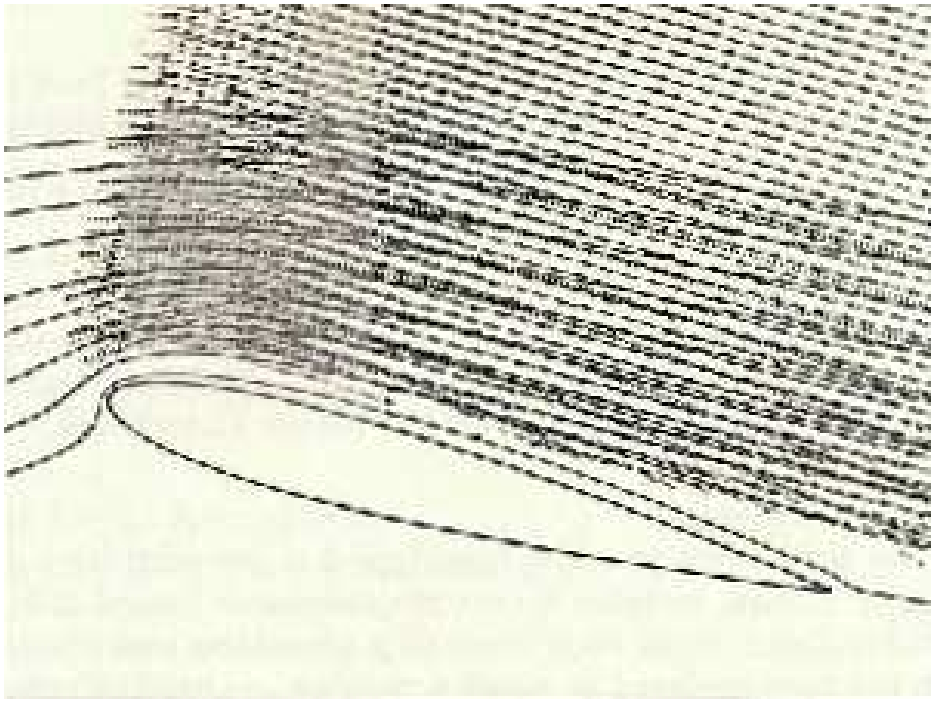

Fig. 1.3 NACA 0012 at 15° during upstroke - broken line corresponds to the PIV measurements (continuous line, calculations). From Wernert et al. [16]

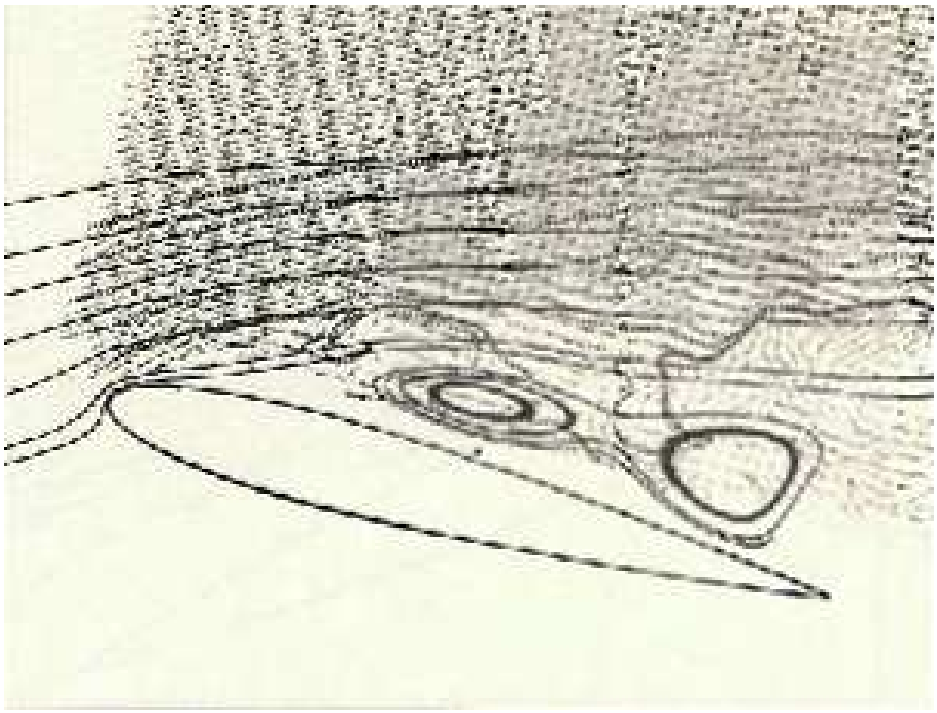

Fig. 1.4 NACA 0012 at 15° during downstroke - broken line corresponds to the PIV measurements (continuous line, calculations). From Wernert et al. [16]

characterised by LE stall and TE stall respectively. It would be ideal to complement this study with examination of the S825 aerofoil, which contrasts with the S809 in having a LE stall and a high $C_{\mathrm{L}\max}$ which leads into the following short introduction to flow control, in 1.3.

Wang et al. [15] conduct purely numerical investigations into oscillating aerofoil experiments by Wernert et al. [16] and Lee and Gerontakos [18]. It is a comprehensive study with detailed analysis and has plots of TVR and vorticity for the upstroke and downstroke. This study is for the low Reynolds number regime, but is a detailed comparison of two turbulence models.

Experiments in the medium of water are rarer but for examples, Tchon [19] investigates dynamic stall on an oscillating aerofoil in waterflow using chronophotography techniques and coloured dye injections while Patterson et al. [20] conduct an investigation to understand vorticity production and dynamic stall in three-dimensional steady water flows.

1.3 Active Flow Control

1.3.1 Introduction to turbine control

The oscillating loads on a turbine are caused by sudden changes in lift seen by the blade. These changes in lift can be caused by a number of events, one such event being turbulence. Turbine control can be split into two categories: active and passive control. Both can improve performance and/or reduce loads, with or without external energy expenditure.

For commercial wind energy in its early days, the stall of the flow about the blade was a passive control concept of its own. The turbines were equipped with fixed-pitch rotor blades designed to operate at the optimal tip-speed ratio (TSR). When wind speed increased, the AoA inherently increased as the blades sped up, flow would begin to stall, and drag increased, thus limiting the absorbed power. The growth in size of turbine blades made this passive control concept unsustainable as the structural and fatigue loads became more pronounced.

The wind turbine equation is:

$$L = \int_{r=0}^{b} \frac{1}{2}\rho \left[C_{L_\alpha}(\alpha + \theta_{\text{pitch}} - \alpha_0)V_{\text{wind}}^2 + (2\pi nr)^2 c\right] dr \tag{1.2}$$

Some of the terms of the equation embodying variables of the turbine are;

1. Blade incidence angle (variable pitch) - θ_{pitch}
2. Flow velocity (variable speed rotor) - n

3. Blade size (variable blade length) - b

4. Blade section aerodynamics -C_{L_α}, α_0

One active control technique is *pitch control* or *furling*. *Pitching* is the act of rotating each blade around its spanwise axis in order to change the effective AoA . This method controls θ_{pitch} in the lift equation for wind turbines. Modern large WTs are also variable speed machines. The variable-speed rotor adjusts the flow velocity in the equation by changing the flow velocity, n. Variable diameter rotors, which alter the turbine blade length, b, are being developed by Frontier Wind and GE Wind.

Variable-speed rotors and active collective blade pitch [4] are not capable of handling oscilllatory or fatigue loads. Therefore, new concepts for controlling fatigue loads on a turbine are needed and these include flow control devices.

1.3.2 Active Flow Control (AFC)

Active Flow Control is the control of the local airflow surrounding a blade or foil. AFC can cause flowfield alteration and methods range from TE flaps to suction or hydrodynamic excitation.

Alternate suction or excitation; including periodic blowing and suction using fluidic actuators in the form of zero-mass/synthetic jets, and in-tandem blowing and suction co-flow jets (CFJs), are the most common.

The idea of flow control through suction is to remove the decelerated fluid near the surface and to attract the high-momentum freestream fluid to the surface. Control through blowing parallel to the wall is to increase the shear-layer spanwise momentum; perpendicular to the wall to enhance the turbulent mixing rate in the BL.

Active flow control devices and actuators, their different locations and their associated flow phenomena are detailed in chapter three of Johnson et al. [24] in their detailed report of AFC methods.

The purposes of flow control devices are to delay/advance transition, to suppress/enhance turbulence, or to prevent/promote separation. According to the authors, flow control can be broken down into three separate categories: control/sensors, actuators/devices, and flow phenomena. Effects include drag reduction, lift enhancement, mixing augmentation and noise abatement.

[4] The traditional method of pitch control uses collective mode, in which all blades are adjusted simultaneously. There is an associated long response time of the turbine to changes in wind direction with this method. Studies of advanced active pitch control methods - cyclic pitch and individual pitch - have been conducted [21],[22],[23] and are evaluated in [24]

A labeling scheme by Wood [25] was introduced: F for fluidic devices, G for geometric devices. In addition to this, four *layers* are described in [24]. *Layer 1* identifies the technique as (F) or (G). (F) actively changes the flow about the blade section by either adding or subtracting air from the external flow, while (G) alters the external geometry. Layer 2 describes the location of the device, (LE), (TE) or mid-chord (MC). Layer 3 describes the effect of the device on the lift curve.

One such effect is translating the curve up or down, equivalent to changing the camber of the aerofoil. They further label this (I) or (D) for increasing or decreasing lift (referred to in this study as a 'decambering' effect). Another effect would be to extend the lift curve to stall at a higher AoA.

Layer 4 differentiates between a steady (S) and unsteady (U) device (i.e. a device whose position varies with time about a nominal setting). A steady operation gives flow 'time' to adapt to the change whereas an unsteady (U) device produces continual dynamic change.

Devices that operate unsteadily but which are also capable of steady operation are labeled (S/U), however research into these devices has shown that unsteady, or pulsed, operation is usually more effective.

'Stall regulation' is the term for the controlled intentional enforcement of the rotor blades to stall. Farthing [26] investigates this for a fixed pitch wind turbine. Yang et al. [27] investigate forced separation over a rotor blade in a hover facility; inflow is obstructed by a plate to induce separation. The aim when it comes to this project on a marine turbine blade is actually to trigger dynamic stall.

An idea presented by Corten [28], however, provides a method of using stall-delaying devices to reduce turbine loads. A common such device is a passive vortex generator to increase C_{Lmax} and delay stall. As C_{Lmax} is increased by the stall-delaying device, Corten reduces the chord, c, by an amount so that the generated lift again equals that of the original blade *without* the device; except that the slope $\frac{\Delta L}{\Delta \alpha}$ is reduced, and the angle of stall, α_{max} is increased (C_{Lmax} is the original). This would allow for smaller blades, requiring less material.

Investigation of unsteady load control by other means such as the use of microflaps and microtabs is found in [29] for a NACA 0012 aerofoil. A microtab study on the S809 aerofoil was made by Standish et al. [30]

AFC devices can supplement full-span pitch control as they would be able to react quickly to reduce the oscillatory, high-frequency loads caused by turbulent winds.

The local flow-field condition is important in the effectiveness of flow control, which can exploit an inherent development path and direct it along to a more desired state (or path).

Passive Flow Control Flow control can also be passive. Passive techniques include geometric shaping using pliable surfaces to manipulate the pressure gradient. These include the use of *fixed* mechanical vortex generators for separation control, the addition of a Gurney flap at the TE and the placement of longitudinal grooves or rivulets to reduce drag.

Because active control systems potentially require power inputs and feedback sensors, recent research has focussed on less complex passive methods requiring no sensing or actuation.

1.4 Examples of Ejection Idea in Literature

Some papers on the subject of ejections of fluid into a boundary layer exist in the literature. As an early example Perring and Douglas [31] conducted an experimental study to compare the effect of pressures or suctions on the upper surface of an aerofoil near stall. Their investigation was to explore a way to delay stall, rather than induce it, but the insights contained therein are nevertheless interesting.

To prevent stall, either the de-energised air is sucked away, or a layer is replenished and thusly re-energised by ejecting air tangential to the upper surface, and in one test both were used in tandem (known together as a CFJ). It was found that either the blowing or suction techniques had a similar effect. They show that there is more of a trend in the effect on lift by the quantity of air ejected, as opposed to the velocity, and that position and shape of the slots is key. It is shown that varying the slot width alters the shape of the lift curve drastically. It was also seen by flow observation that streamlines broke away from the surface some distance before the slot near the LE with suction, and that a region of 'marked' turbulence clung to a point ahead of the slot.

The paper by de Graffenried [32] explores injecting a 'sheet' of fast moving air at-or near- the LE stagnation streamline. It is explained by the author that for gas flowing over a solid surface, 'those molecules which are near to and impact the molecular lattice of the solid surface are thought to be momentarily adsorbed thereon'[32, p.2]. In boundary layer theory, velocity at the boundary is zero, and this is known as the no-slip condition. The injection 'canard' in this instance is not located on the aerofoil, but slightly upwind from the LE (the *canard configuration* is the positioning of the pitching control surface (commonly *tailplane*) at the front of an aircraft).

Experiments show that 'Increased pressure on the top surface of the aerofoil downstream of the aerofoil's $t_{\max}$ chordwise station causes much reduction in profile drag, and also causes some decrease in lift…' (p.4). The author posits that at higher angles of attack, the technique could be used to result in a 'more gentle decrease beyond $C_{\mathrm{L}\max}$, that is, a more

gentle on-set of stall'. Another interesting way of looking at the behaviour was by the author conceptualising an aerodynamic circuit consisting of upstream velocity profile 'input' and wake-velocity profile 'output'.

Hassan and Munts [33] examine the role of the injection angle - normal or near-tangent - in the effects of an array of oscillatory synthetic jets on the aerodynamics of two symmetric aerofoils - the NACA-0012 and -0015 and supplement this with predicted particle trajectories. Synthetic jets are classed as a combination of G/F devices as they use mechanical motion - not in contact with the external flow, to oscillate a membrane inside a cavity inside the aerofoil.

Fric and Roshko [34] investigate a transverse turbulent jet using flow visualisation and HWA. They find that downstream and to either side of the jet, it causes an adverse pressure gradient on the wall and provokes 'separation events' in the boundary layer on each side. The wake is orderly and the wake Strouhal freqiencies were found to correspond to the frequency of separation events.

1.5 Project Overview

Aim

The aim of this work is to use CFD to model a device to reduce the gust load on a marine turbine blade. It investigates triggered dynamic stall as a method of gust load alleviation. This device was decided to be in the form of an ejection jet.

The tidal turbine operating environment is one of a highly unsteady, time-varying nature with considerable shear and turbulence, complicated further by unsteady rotating effects. The occurrence of dynamic stall during normal operating conditions has the potential to dramatically reduce the turbine power output; a consequence that it is required to avoid.

In the process of CFD simulation it is hoped more will be found out about dynamic load behaviour. It should also improve understanding of the complex interplay between structural dynamics and hydrodynamics.

The work will approach this problem by using CFD to model an aerofoil undergoing pitching oscillations, then subjected to flow oscillation, then modified by a DS device – blowing actuators and/or trips – designed to trigger dynamic stall.
The final goal is to store the results in a database, so that by using a Blade Element Momentum (BEM) model, it is possible to perform a force analysis of the turbine blade geometry.

The majority of work to date on dynamic stall has focussed on the development of helicopter rotor blades, and more recently wind turbine applications. Drawing on this

experience and knowledge, but considering the thicker blade sections generally required for tidal turbines, the project aims to provide guidance for future tidal turbine design.

It is an aim of this investigation to simulate dynamic stall in 2D and to produce a validation case. There are experimental data available for validation, but it is recognised that two-dimensional experiments are extremely difficult to achieve, particularly at higher angles of attack approaching stall.

Atmospheric winds inflow fluctuations and anomalies introduce overriding uncertainty into turbine aerodynamics data. This problem led to the US NREL Unsteady Aerodynamics Experiment (UAE) horizontal axis wind turbine (HAWT) in the NASA-Ames 80 ft by 120 ft wind tunnel, completed in May 2000 [35].

Wind turbine data currently depend on the relative pitching motion idea, and it is also an aim of this project to compare and contrast numerical results from pitching the aerofoil in a freestream, with those from subjecting the static aerofoil to an oscillating inflow.

Previous studies exist of, for example, synthetic jets near the TE, but which have the exit normal to the surface. Jets commonly exit perpendicularly to the surface of the aerofoil or parallel to the surface. This study explores angled ejection as well as chordwise location.

This study examines the role of angled ejection in the effect of oscillatory blowing. It accomplishes this by conducting unsteady simulations with sinusoidal jet excitation and an oscillating-flow inlet boundary condition. The jet is always blowing, in contrast to oscillatory synthetic jets that use periodic blowing and suction. How to realise the blowing is not covered here - this CFD study looks principally at the effects on the surrounding flow field.

Objectives

The main objectives of this work are as follows;

1. Conduct a set of 2D steady state CFD simulations of two aerofoils and obtain C_{L} and C_{D} data and compare this with experimental data.

2. Run 2D transient simulations of a pitching aerofoil and compare with experiments.

3. Run 2D transient simulations of spatially stationary aerofoil exposed to oscillating inflow conditions, and compare with pitching case.

4. Run 2D transient simulations of spatially stationary aerofoil exposed to oscillating inflow conditions fitted with stall-promoting trip devices.

5. Supply actively stalled aerofoil data for use in BEM-code transient simulations

Chapter 2

Methodology

2.1 Introduction

The strategy of CFD is to replace the continuous problem domain with a discrete domain using a grid, also called a mesh. In the continuous domain, each flow variable is specified at every possible point in the domain, e.g. for a pressure distribution, $p = p(x)$, $x \in \mathbb{R}$. In the discrete domain, each variable is expressed only at the grid points , $p_i = p(x_i)$, $i = 1, 2 \ldots, N$.

In a CFD solution, one would directly solve for the relevant flow variables only at the grid points. The values at other locations are determined by interpolating the values at these grid points.

Grid sizes are chosen to selectively resolve the details of the flow while managing computational cost. Grid considerations are discussed in 2.7 and 2.7.1. The meshes used in ANSYS FLUENT have been generated using ANSYS ICEM CFD. The findings of a mesh dependency study are described in 2.7.2.

CFD codes allow for extra visualisation power than by experiment only, to obtain details of the flow field and to find features not generally detectable from experimental observation.

The governing equations of fluid dynamics are mathematical statements of the three basic principles of conservation of mass, momentum and energy. The continuity equation for mass (in Cartesian tensor notation):

$$\frac{\partial \rho}{\partial t} + \frac{\partial}{\partial x_j}(\rho u_j) = 0 \tag{2.1}$$

is the *material derivative* of density. In incompressible flow ρ = constant and so $\frac{\partial \rho}{\partial t} = 0$. Thus, to satisfy the continuity equation, $\frac{\partial u_j}{\partial x_j} = 0$.

A *viscous flow* is defined as a flow wherein viscous forces are important when compared to inertial forces. The momentum equations for viscous flow are called the Navier-Stokes (NS) equations, named after engineer and physicist Claude-Louis Navier and mathematician George Gabriel Stokes; the latter of whom derived the model law for a pendulum in viscous flow by means of the differential equations now bearing their names. The NS equations arise from Newton's second law, when applied to an infinitesimal fluid element.

The Reynold's number, *Re*, derived in 2.6, is sometimes described as the ratio of inertial to viscous forces. At low *Re*, the naturally occurring disturbances are dissipated away and the flow remains laminar. At high Re, the inertia forces are significant enough to amplify the disturbances. Transition from laminar to turbulent occurs.

The momentum conservation equations are a coupled system of non-linear PDEs that are a challenge to solve analytically. Therefore the equations are solved numerically. A broad class of numerical methods have been developed for solving the incompressible Navier-Stokes equations. They range from linear methods through to high-resolution (non-oscillatory) methods. By far the most usable is the RANS (Reynolds Averaged Navier-Stokes equations), the time-averaged equations of fluid flow.

The RANS solver FLUENT is used in this study. Section 2.5 introduces the solver as a sort-of guide using terms found in the FLUENT environment.

2.2 Reynolds-Averaged Navier-Stokes (RANS) equations

Turbulent flows are unsteady by definition. For turbulence then, variables such as velocity must be described as an instantaneous variable. In solving the equations a simplification is found by decomposing an instantaneous quantity into its time-averaged and fluctuating quantities. This process is named *Reynolds decomposition*.

Velocity is thus decomposed into a steady mean value, $\bar{u}$, with a fluctuating component, $u_i'(t)$, as $u_i(t) = \bar{u}_i + u_i'(t)$ and similarly for the other quantities, (pressure) $p = P + p'$ and (shear stress) $\tau_{ik} = \bar{\tau_{ik}} + \tau_{ik}'$. The fluctuations are distributed to some measure in all directions.

With the mean and fluctuating quantities substituted in 2.1 (if any terms have 2 means and a fluctuating part, these cancel, so too if there is 1 mean and 1 fluctuating part) the continuity equation becomes:

$$\frac{\partial}{\partial t}\bar{\rho} + \frac{\partial}{\partial x_i}\left(\bar{\rho}\bar{u}_i + \overline{\rho' u_i'}\right) = 0$$

Since ρ = constant, $\frac{d\bar{\rho}}{dt} = 0$ and $\rho' = 0$, the continuity equation for an incompressible fluid is $\frac{\partial \bar{u}_i}{\partial x_i} = 0$.

The momentum equation is (in Cartesian tensor form):

$$\frac{\partial}{\partial t}(\rho u_i) + \frac{\partial}{\partial x_j}\left(\rho u_i u_j\right) = -\frac{\partial p}{\partial x_i} + \frac{\partial \tau_{ij}}{\partial x_j} \tag{2.2}$$

Obviously in steady cases $\frac{\partial \bar{u}_i}{\partial t} = 0$. Substituting the mean and fluctuating quantities in the momentum equation it becomes:

$$\frac{\partial}{\partial t}\left(\bar{\rho}\bar{u}_i + \overline{\rho' u_i'}\right) + \frac{\partial}{\partial x_j}\left(\bar{\rho}\bar{u}_i\bar{u}_j + \bar{u}_i\overline{\rho' u_j'}\right) = -\frac{\partial \bar{p}}{\partial x_i} + \frac{\partial}{\partial x_j}\left(\overline{\tau_{ij}} - \bar{u}_j\overline{\rho' u_i'} - \overline{\rho' u_i' u_j'}\right)$$

The last 2 terms on the RHS represent turbulent transport. For incompressible flows the density-generated terms disappear and the equation simplifies to:

$$\rho\left(\underbrace{\frac{\partial \bar{u}_i}{\partial t}}_{*} + \frac{\partial}{\partial x_j}\bar{u}_i\bar{u}_j\right) = -\frac{\partial \bar{p}}{\partial x_i} + \frac{\partial}{\partial x_j}\left(\overline{\tau_{ij}} - \rho\,\overline{u_i' u_j'}\right) \tag{2.3}$$

remembering ρ is constant, and where

$$\bar{\tau}_{ij} = \mu\left(\frac{\partial \bar{u}_i}{\partial x_j} + \frac{\partial \bar{u}_j}{\partial x_i}\right) \tag{2.4}$$

for a Newtonian fluid. The time derivative of a *time averaged quantity* * is zero but is retained in the RANS momentum equation. The basis of this is the assumption that the averaging time is larger than the time scale of small turbulent fluctuations, but much smaller than the time scales of the bulk flow activities, such as vortex shedding. On this basis the RANS method may be applied to unsteady flow, where it is referred to as URANS.

The horizontal component of velocity is gradually slowed down due to viscous effects and the vertical component should be acting to remove fluid from the BL.

In the case of an APG, large scale turbulent structures in the outer layer provide most of the total turbulent energy. There is increased shearing stress accompanying turbulence, which is due to the momentum interchange caused by lateral fluctuations of velocity. Tongues of large-eddy fluid erupt into the free stream.

The mean rate of strain tensor is:

$$\bar{S_{ij}} = \frac{1}{2}\left(\frac{\partial \bar{u}_i}{\partial x_j} + \frac{\partial \bar{u}_j}{\partial x_i}\right) \tag{2.5}$$

This means $\bar{\tau_{ij}}$ in 2.3 can be replaced with $2\mu\overline{S_{ij}}$.

The last term on the RHS of 2.3 is a term representing the mean effects of turbulence, the Reynold's stress tensor. It is known as the Reynold's stress since it shares units with stresses. The approximate scale of the largest eddies, what is known as the 'integral scale', is related to this important quantity. There are now more unknowns than equations. A further equation is necessary to provide the Reynold's stress tensor. The absence of this additional equation is often referred to as the 'turbulence closure problem'.

2.3 Turbulence Closure using the $k-\omega$ eddy-viscosity model

Numerical models are used to parameterise turbulence due to the constraint on computers and partly due to the classical problem that the equations for turbulent moments are not closed. Turbulent closure schemes are commonly based upon scaling arguments and contain constants that must be determined from measurements.

The RANS equations have a closure problem due to the term $-\rho\ \overline{u_i' u_j'}$ - the Reynold's stress tensor. As mentioned previously, this term represents the mean effects of turbulence, the turbulent stresses. It needs to be expressed using time-averaged quantities to close the system of equations.

There is no one universal turbulence model that may be applied for all CFD problems and this has resulted in different turbulence models which are based on different physical modelling assumptions. They can generally be classed into two groups, eddy-viscosity models (linear and nonlinear) and Reynolds stress models (RSM) (see Tu [36] for an overview of RSM). Various eddy viscosity models are implemented in commercial flow solvers such as ANSYS FLUENT and are usually the first choice for modelling turbulence for engineering applications.

The underlying assumption used in all eddy viscosity models is the Boussinesq hypothesis [37]. Joseph Boussinesq proposed relating the turbulent stresses to the mean of the velocity gradients in order to close the system of equations. The Boussinesq hypothesis states that the Renolds stress tensor $\tau_{ij} =; -\rho\ \overline{u_i' u_j'}$ is proportional to the traceless mean strain rate tensor, S_{ij} by:

$$-\rho\,\overline{u_i'u_j'} = 2\left(\mu_T\overline{S_{ij}} - \frac{1}{3}\rho k\delta_{ij}\right) \tag{2.6}$$

where $k = \frac{1}{2}\overline{u_i'u_i'}$ is the turbulent kinetic energy. A new proportionality constant μ_T has been introduced; the 'eddy viscosity' (also termed turbulent viscosity).

This is now the commonest method of RANS-based CFD: everything depends on modelling the eddy viscosity μ_T. The Boussinesq hypothesis assumes the eddy viscosity to be isotropic.

One such eddy-viscosity model is the $k-\omega$ model. The first variable k - the turbulent kinetic energy (TKE) - determines the level of energy in the turbulence. The second, ω, is the *specific dissipation rate* of TKE and this determines the scale of the turbulence. The model is a set of transport equations that include terms for production, effective diffusivity and dissipation of k and ω. The equations are:

$$\frac{\partial}{\partial t}(\rho k) + \bar{u}_j\frac{\partial}{\partial x_j}(\rho k) = \underbrace{\tau_{ij}\frac{\partial \bar{u}}{\partial x_j}}_{P_k} + \frac{\partial}{\partial x_j}\underbrace{(\mu + \sigma_k\mu_{\mathrm{T}})}_{\Gamma_k}\frac{\partial k}{\partial x_j} - \underbrace{\beta^*\rho\omega k}_{C_k} + S_k \tag{2.7}$$

$$\begin{aligned}\frac{\partial}{\partial t}(\rho\omega) + \bar{u}_j\frac{\partial}{\partial x_j}(\rho\omega) = \underbrace{\frac{\mu}{\mu_{\mathrm{T}}}\tau_{ij}\frac{\partial \bar{u}}{\partial x_j}}_{P_\omega} + \frac{\partial}{\partial x_j}\underbrace{(\mu + \sigma_\omega\mu_{\mathrm{T}})}_{\Gamma_\omega}\frac{\partial \omega}{\partial x_j} - \underbrace{\beta\rho\omega^2}_{C_\omega} + \ldots \\ \underbrace{2(1-F_1)\rho\sigma_{\omega 2}\frac{1}{\omega}\frac{\partial k}{\partial x_i}\frac{\partial \omega}{\partial x_i}}_{D_\omega} + S_\omega\end{aligned} \tag{2.8}$$

where P_k and P_ω represent production of k and ω respectively ; Γ_k and Γ_ω the effective diffusivity; C_k and C_ω the dissipation; D_ω is the cross-diffusion term. It is possible to add user-defined source terms S_k and S_ω. The terms of production, diffusivity and dissipation are closed by a system of equations that rely on multiple empirically-evaluated parameters. Experiments can test the turbulence parameterisation of a model and lead to improvements by researchers learning more about how these parameters behave, for instance Wiles et al. [38] for a marine environment.

The damped cross-diffusion derivative term is introduced as part of the formulation of the SST $k-\omega$ model, to blend the $k-\omega$ and $k-\varepsilon$ models together. Blending functions then control the behaviour of the models in the SST: for example, the SST formulation switches

to $k-\varepsilon$ behaviour in the free-stream, avoiding the common $k-\omega$ problem that the model is too sensitive to the inlet freestream turbulent (FST) properties.

To achieve this blending, the k- ε model is transformed into equations based on k and ω. Then the standard k- ω model and the transformed k- ε model are both multiplied by the blending function and both models are added together. The blending function turns the $k-\omega$ model on in the near-wall region, retaining its robustness and accuracy in the near-wall region.

The SST $k-\omega$ model includes prediction of the laminar-to-turbulent transitional process, and hence the 'transition point', whereas the standard k-ω model theory assumes fully turbulent flow. The modelling of transition is realised by damping the turbulent viscosity μ_T, which is:

$$\mu_t = \frac{\rho k}{\omega} \frac{1}{max\left[\frac{1}{\alpha^*}, \frac{SF_2}{a_1 \omega}\right]} \tag{2.9}$$

where S is the strain rate magnitude, F_2 a blending function, α^* a damping coefficient, and α_1 a model constant. See the following section, *Intermittency Transition Model*. Both the standard k-ω and the k-ω SST model have been reported to perform well in flows with large separation regions and severe adverse pressure gradients. Wang et al. [15] assess the ability of the standard k-ω model and the SST k-ω model to correctly simulate dynamic stall in the low Reynolds number regime. The authors find that the k-ω SST model presents a more complex and realistic flow structure compared to the standard k-ω model.

They find that the k-ω SST model performs well at the range of AoAs $-5^\circ < \alpha < 20^\circ$ but not so well at high AoAs in the region $20^\circ < \alpha < 25^\circ$, where deep stall is to be expected.

In terms of accuracy, 'almost all of the models fail to generate results which can consistently agree well with the experimental data, in particular for those pitching patterns associated with higher angles of attack and high reduced frequency.' [15, p.1531]. However, it is found from PIV data that the SST k-ω model performs the best overall.

They conclude that, from their comparison of the dimensions of vortices found by the SST k-ω model to those found by the k-ω, and from their finding that the k-ω model fails to predict the severe adverse pressure gradient, that the k-ω may be more dissipative in terms of the eddy energy, and that this may also be due to the assumption of fully turbulent flow.

Intermittency Transition Model

The traditional means of modelling transition was to demarcate the transition location based on experimental observation, or to trigger transition for the experiment; by placing a tripwire or turbulator tape before the point of decelaration. And for computations, to “switch" on the turbulence model at this point. But this neglected the complexity of transition. One such complexity being ‘intermittency’, so-called because for free-stream two-dimensional flows, ‘separation begins intermittently at a given location; that is, the flow reversal at that location occurs only a fraction of the total time.’ [39, p.206]. Transitional flows are well-characterised in the literature, for example Simpson (ibid.), which reviews knowledge of two-dimensional turbulent separated flows.

Figure 2.1, taken from Simpson, shows the separation region: the ‘traditional’ view of the TBL, above, and below, experimentally-determined points; among them, the point of ‘Intermittent Transitory Detachment’ (which corresponds to the ‘location of turbulent separation’, or ‘intermittent separation’).

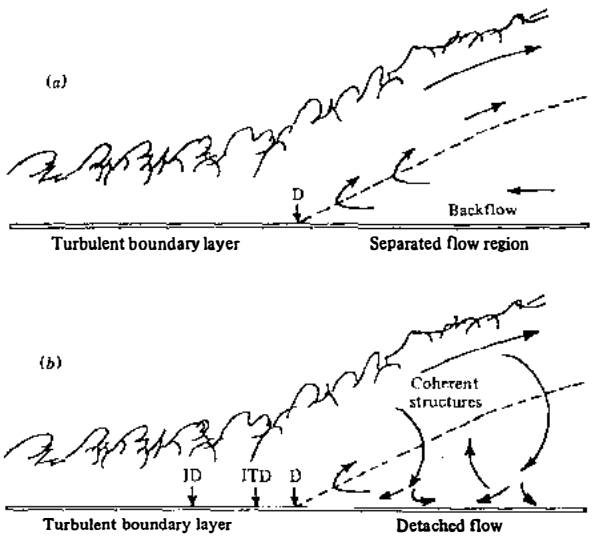

Fig. 2.1 (a) Traditional view of TBL separation with the mean backflow coming from far downstream. The dashed line indicates $U = 0$ locations. (b) A flow model with the turbulent structures supplying the small mean backflow. ID, incipient detachment; ITD, intermittent transitory detachment; D, detachment. The dashed line denotes $U = 0$. From Simpson [39].

The challenge was then to work that into a computational model. Conventional RANS codes do not lend themselves easily to transitional flows where both linear and non-linear effects are relevant. RANS-averaging ‘eliminates the effects of linear disturbance growth and is therefore difficult to apply to the transition process’ [40, p.278].

This is done using an intermittency factor, γ, which modifies the eddy-, or turbulent-viscosity in the EVM. The classical approach consists of multiplying the eddy-viscosity by γ to define the effective eddy-viscosity in the transitional flow. Thereby a transport equation for γ is found. Other turbulent quantities are predicted in the usual way.

$$\frac{\partial}{\partial t}(\rho\gamma) + \frac{\partial}{\partial x_j}(\rho U_j \gamma) = P_\gamma - E_\gamma + \frac{\partial}{\partial x_j}\left[\left(\mu + \frac{\mu_t}{\sigma_\gamma}\right)\frac{\partial \gamma}{\partial x_j}\right] \tag{2.10}$$

The Intermittency Model in FLUENT is available for use with the k-ω SST model. It is based on the γ-Re_θ model, but solves for only one transport equation 2.10 for γ and has a correlation proprietary to FLUENT, to trigger the transition model. This avoids the need of a second equation for Re_θ, and the dependency of Re_θ on the velocity U. This renders the computational model *Galilean Invariant*.

A TKE Production limiting option is selected by default for all two-equation models based on the ω equation in FLUENT, as the SST k-ω model does, however, produce too large a turbulence level in regions with large normal strain; such as stagnation regions and regions with strong acceleration. This tendency is actually less pronounced than with a standard $k-\varepsilon$ model. The first formulation prevents stagnation point buildup and is enabled by default. The second formulation is based on the work by Kato and Launder [41], who noticed that the excessive level of TKE production is caused by the very high level of shear strain rate 2.5 in the stagnation regions. This is switched on. The Kato-Launder formulation and production limiter can be applied simultaneously, as is done for the Transition SST model by default.

2.4 Discretisation

In the computational space it is mandatory to operate by discrete rather than by differential operators. Generally, the discretised equations are applied to the cells in the interior of the domain and for cells at, or near, the boundary, a mixture of the discretised equations and boundary conditions are applied.

The steady and unsteady RANS are solved using the FLUENT solver which is based on the cell-centred finite volume method. The momentum equation can be interpreted as an advection/diffusion equation for the velocity. The conservation law says that;

Rate of change	+ Advection	+ Diffusion	= Source		
$\frac{d}{dt}\int_\Omega \rho d\Omega$	$+\int_S \rho(\vec{V}\cdot\vec{n}_S)dS$		$=0$	$(Continuity)$	(2.11)
$\frac{d}{dt}\int_\Omega (\rho\vec{V})d\Omega$	$+\int_S (\rho\vec{V})(\vec{V}\cdot\vec{n}_S)dS$	$+\int_S (\vec{\tau}\cdot\vec{n})dS$	$=\int_S(-p\vec{n})$	$(Momentum)$	(2.12)

where V is the cell volume and $\hat{n}()$ is the unit outward normal vector to the boundary (to the surface) which multiplied by the scalar gives the correct projected area $\hat{n}|dA| = d\vec{A}$. The advection term is non-linear giving the equations their characteristic non-linearity.

Spatial discretisation

Discretisation of the governing equations may be shown by considering the unsteady conservation equation for transport of a scalar quantity ϕ. This is written in integral form for an arbitrary control volume V:

$$\int_V \frac{\partial \rho\phi}{\partial t}dV + \oint \rho\phi\vec{u}\cdot d\vec{A} = \oint \Gamma_\phi \nabla\phi \cdot d\vec{A} + \int_V S_\phi dV \tag{2.13}$$

where $\vec{u}$ is the velocity vector, $\vec{A}$ is the surface area vector around the control volume V, Γ_ϕ is the diffusion coefficient for ϕ, and S_ϕ is the source of ϕ per unit volume. Applying 2.13 to each control volume yields a discretised version of the form:

$$\frac{\partial \rho\phi}{\partial t}V + \sum_f^{N_{\text{faces}}} \rho_f\phi_f\vec{u}_f\cdot\vec{A}_f = \sum_f^{N_{\text{faces}}} \Gamma_\phi\nabla\phi_f\cdot\vec{A}_f + S_\phi V \tag{2.14}$$

where V is the cell volume, N_{faces} is the number of faces enclosing the cell, and ϕ_f the value of ϕ convected through face f. The last term on the RHS includes the mass flux through a face, $\rho\vec{u}\cdot\hat{n}A$ which has units of kg/s.

Discrete values of ϕ are stored at the cell centres, however face values ϕ_f are required for the convective terms and are thus interpolated from the cell centre values ϕ_p. This is accomplished using an upwind scheme. Upwinding means that the face value ϕ_f is derived from quantities in the cell upstream, or "upwind" relative to the freestream velocity $\vec{u}$.

For example, first order accuracy is achieved when the face value of ϕ_f is set equal to the cell centre value in the upstream cell, referred to as the first-order upwind scheme. Higher-order accuracy is achieved at cell faces by way of a Taylor series expansion of the cell-centred solution about the cell centroid. Transport equations for both the SST k-ω model

and the transitional model implemented a second-order upwind scheme. This advection scheme is also used for the momentum equation.

Temporal discretisation

A steady solution may be achieved if the flow problem does not exhibit time-varying flow features, while, for unsteady flow, the evolution of the flow field must be solved by time-marching. Both methods are used in this study.

When conducting unsteady simulations, the governing equations are discretised in time as well as space. The temporal discretisation involves the integration of each term in the differential equations over a given time-step Δt.

The time evolution of a variable ϕ is given by

$$\frac{\partial \phi}{\partial t} = F(\phi) \tag{2.15}$$

where the function F incorporates any spatial discretisation. Using backward differences, the first and second-order accurate forms are given respectively as:

$$\frac{\phi^{n+1} - \phi}{\Delta t} = F(\phi^{n+1}) \tag{2.16}$$

and

$$\frac{3\phi^{n+1} - 4\phi^{n} + \phi^{n-1}}{2\Delta t} = F(\phi^{n+1}) \tag{2.17}$$

where n is the value at the current time level (t), $n+1$ is the value at the next time level $(t+\Delta t)$, and $n-1$ the value at the previous time level $(t-\Delta t)$.

Whichever level of accuracy is selected, equation 2.16 or 2.17 is solved iteratively at each time level for ϕ^{n+1} - this is implicit time integration. The time step itself is covered in section 2.8.1.

2.5 The Solver setup

The solver is the commercial software ANSYS FLUENT 15.0 which solves the RANS using the cell-centred finite volume method. The solver operates an iterative procedure. This allows for efficient matrix inversion with greatly reduced memory requirements, and is necessary to solve non-linear equations.

The choice of primitive variables (pressure-based or density-based) is essential to the type of problem encountered. Under *Solution Setup* of FLUENT, on the *General* task page, the *Solver 'Type'* can be *pressure-based* or *density-based*. The pressure-based method is used, as is common practice for problems involving incompressible flow.

It employs an algorithm that belongs to the projection method, which solves for a pressure correction equation to find the constraint on the mass continuity of the velocity field. *Absolute* velocity formulation is selected.

The turbulence model (in the *Models* task page) used is the viscous shear-stress transport (SST) k-ω Model. *Low-Re Corrections* was enabled under *'k-omega Options'*, as were the four general *'Options'*: *Curvature Correction*, *Production Kato-Launder*, *Production Limiter* and *Intermittency Transition Model*. *Crossflow Transition* was switched off. All the model constants were their default values, except where built-in corrections were enabled. On the *Materials* task page, *air* was chosen. Density was 1 kg/m^3, held constant, and viscosity was scaled as 1×10^{-07} by considering preservation of the Reynold's number, *Re*, which will be discussed in section 2.6.

Boundary Conditions were mostly kept constant and are described in 3.1 and tabulated in 3.1.1.

Two pressure-based solver algorithms are available in FLUENT. Under *Solution*, on the *Solution Methods* task page, the velocity-pressure algorithm can use either a segregated or a coupled solution *'Scheme'*.

The segregated approach solves the equation of each variable separately, using previously computed best-estimate values of the other dependent variables. It is memory-efficient, since it need only store one solution variable at a time.

A segregated, or 'decoupled' pressure-based solver in FLUENT is the *SIMPLE* algorithm. However, its convergence is highly affected by the explicit treatment of the pressure gradient in the momentum equation, and the velocity field in the continuity equation.

There is one coupled algorithm in FLUENT. A coupled algorithm treats both pressure and velocity terms in an implicit manner. This is achieved by coupling the momentum equation and the pressure equation form of the continuity equation through a set of coefficients that represent the mutual influence of the continuity and momentum equations on the pressure and velocity fields. The coupled scheme is selected for this study.

All the governing equations for the solution variables which are decoupled from each other, are solved sequentially, except for velocity and pressure which are coupled using the *Coupled* choice of coupling algorithm. During the coupled approach, the conservation equations are discretised and solved as a system of equations. This improves the convergence compared to the segregated algorithm, but takes up to twice as much memory.

With respect to the discretisation of the convection terms in the transport equations for the velocity and turbulence quantities, *second-order upwind* schemes were preferred. The interpolation scheme (again in Solution Methods) for pressure was *Standard*, while *Momentum*, *Intermittency*, *Turbulent Kinetic Energy* and *Specific Dissipation Rate* were all *Second Order Upwind*. *Transient Formulation* when it was needed was also second order upwind. No other options were selected - higher-order-term relaxation (abb. HOTR) was not needed as strict convergence criteria were met. The methods used to monitor convergence are discussed in 2.8.

On the *Solution Controls* task page, *'Under-Relaxation Factors'* were the default values to enhance the stability of the numerical procedure and to ensure the convergence of the iterative process.

2.6 Model scaling

A physical model tends to be a smaller-scale, simplified reproduction: of an object, of states and of flow processes.

To yield qualitatively and quantitively useful results, physical models must fulfil three scaling laws;

1. Geometrical similitude
2. Kinematic similitude
3. Dynamic similitude (Forces similitude)

Geometric similarity In dimensional analysis, consideration of shape effects is often eliminated by making the model the same shape: i.e. geometrically similar. If the shape of the model is considered to be fixed from the outset, then the size of the model is specified completely by designating a single characteristic length, say, the aerofoil chord: c.

Transient scaling The concept of similarity extends to many other characteristics besides geometry. If transient behaviour occurs in a model, it is necessary to introduce the concept of 'homologous times' between model and prototype (experiment). Langhaar [42, p.63] states that:

'In all cyclical phenomena, homologous times for a model and its prototype are instants that occur in the same fraction of a cycle'

Equation 1.1 for the reduced frequency is a dimensionless parameter. U'_∞ in the OSU wind tunnel is 33 m/s, c' in the unsteady experiments of Ramsay et al. [9] is 0.457 m. The

model chord c is 0.1m and U_∞ is 1 m/s. Using 1.1 the ratio of the experimental frequency to the model frequency is $f'/f = \frac{c/c'}{U'/U}$. The ratio of the cyclic periods is $f/f' = K_t$, where K_t is known as the 'time scale factor'. In a cyclic phenomenon, the time scale factor is the ratio of the cyclic periods of the two systems.

Kinematic similarity For kinematic similarity to exist, material particles of two systems must be homologous. The definition from Langhaar [42, p.68] states that:

> *The motions of two systems are similar, if homologous particles lie at homologous points at homologous times.*

If kinematic similarity exists, corresponding components of velocity or accelaration are similar. The vectors have homologous directions and this also means the streamlines of the similar fluid motions are homologous curves.

Dynamic Similarity Full dynamic similarity between two geometrically and kinematically similar systems results from Newton's second law and requires that the ratios of all corresponding force vectors in both systems be equal.

The following principle from Langhaar [42, p.152] states:

> *In geometrically similar systems with kinematically similar steady flows and similar pressure distributions, the ratios of inertia force to friction force are identical if the Reynolds numbers are equal, the ratios of inertia force to pressure force are identical if the pressure coefficients are equal.*

Complete dynamic similitude is only possible at scale 1:1. Therefore, the most appropriate governing force must be chosen, which, together with the inertial force, should be scaled while all other forces are neglected. Dynamic similarity cannot be fulfilled simulataneously in the same model for the other forces, leading to so-called *scale effects*. The largest amount of testing for scale effect was done at the NPL (National Physical Laboratory) by Diehl [43].

In an incompressible fluid flow, dynamic similarity follows from kinematic similarity, since the mass distributions are necessarily similar.

Reynolds Number Since viscous friction forces dominate it is the Reynolds similitude that will be used. For true dynamic similitude, the *Re* numbers must be the same in model and prototype. It is implied by the chord *Re* that geometrically similar aerofoils will give identical characteristic curves when tested at speeds inversely proportional to their chords.

In general, if D denotes a characteristic length of the system - in this case the chord, the dimensionless product $\rho VD/\mu$ is called Reynold's number.

The chord Reynolds number $Re = cV_\infty/\nu$, where ν is the kinematic viscosity, is derived below.

The ratio of the kinematic viscosity for model and prototype are fixed by the geometric scales. If x', y' represent the true x and y of the scenario in planar x y coordinates, and v' the true velocity, then

$$x = x'c\, y = y'c\, v = v'V \tag{2.18}$$

Time is now

$$t = t'\frac{D}{V} \tag{2.19}$$

This can be shown by taking the curl of the continuity equation in order to derive the Reynolds number. The vorticity $\Omega = \nabla \times v$. Using the identity that $\nabla^2(\nabla \times v) = \nabla \times \nabla v^2$,
then

$$\begin{aligned} \nabla \times \left(\frac{\partial \rho}{\partial t} + \rho \nabla \cdot \bar{v} \right) = \nabla \times \rho \frac{\partial v}{\partial t} + \Omega \times v + \frac{1}{2}\nabla v^2 = \dots \\ -\nabla p - \rho \nabla \phi + \mu \nabla^2 v + (\mu + \mu')\nabla(\nabla \cdot v) = \dots \\ \underbrace{\frac{\partial}{\partial t}\nabla \times v}_{*} + \nabla \times (\Omega \times v) = \mu \nabla^2(\nabla \times v) = \mu \nabla^2 \Omega \end{aligned} \tag{2.20}$$

Dividing all sides by ρ and knowing that $\frac{\mu}{\rho} = \nu$ (the kinematic viscosity) then the last term becomes $\nu\nabla^2\Omega$.

Since $\Omega = \nabla \times v$, which is a spatial derivative of v, and since we are scaling v' (Vv'=v), then, scaling in terms of units V and D, $\frac{V}{D}(\nabla \times v') = \frac{V}{D}\Omega'$

Along with the units of vorticity $\frac{1}{t} = \frac{V}{D}\frac{1}{t'}$ or $t = t'\frac{D}{V}$. Therefore, if t is the characteristic time of the aerofoil, then $t = t'\frac{c}{U}$. The characteristic time is an estimate of the reaction time scale of a system. It can loosely be defined as the inverse of the reaction rate.

Indicated by * $\frac{\partial}{\partial t}\Omega$, is the unsteady material derivative of the vorticity. It describes the rate of change of vorticity (the *angular accelaration* of the fluid particle) and is an indicator of unsteadiness in the flow.

Similarly:

$$\underbrace{\frac{\partial}{\partial t'}}\Omega' + \nabla \times (\Omega' \times v') = \frac{\mu}{\rho}\nabla^2\Omega' \tag{2.21}$$

Again analysing units we see;
$\frac{1}{\rho}\frac{\mu}{V^2}\frac{D^2}{D^3}V$ or $\frac{\mu}{\rho VD}$ which, inverted, is of course the Reynolds number.

Buckingham's Theorem says that:

> *If an equation is dimensionally homogeneous, it can be reduced to a relationship among a complete set of dimensionless products.*

All the fundamental equations of physics are dimensionally homogeneous. Therefore relationships deducible from these equations are consequently dimensionally homogeneous. Reynolds number can also be derived from the non-dimensional form of the incompressible Navier–Stokes equations, or by a combination of solving the dimensional matrix of the variables and simple inspection thereof. Another dimensionless product found this way takes the form of a pressure coefficient:

$$\frac{F}{\rho V^2 D^2} \tag{2.22}$$

This expression is integrated in order to find the force on the aerofoil, which is then resolved into components of lift and drag. Together, *Re* and the pressure coefficient C_p form a complete set of dimensionless products of the variables concerned. Then the function is not actually a function of each of the separate variables, but rather a function of a complete set of dimensionless products of the variables.

It is because of these tools of Dimensional Analysis that it is possible to test at much smaller scales. Provided that, in this case, the Reynolds number is the same for the model as for the prototype (the experiment) - and although complete similarity is infeasible - similar results may be achieved. This is expected to remain valid for turbulent flow.

2.7 Mesh generation

A grid or mesh can be described either as ‘structured’ or ‘unstructured’. Structured grids are made up of rectangular elements with 4 nodal points in 2D (hexahedral with 8 nodal points in 3D) and have regular connectivity. Unstructured mesh has irregular connectivity. This allows for any possible element shape that a solver might be able to use. Typically an unstructured mesh is made up of triangle-shaped elements in 2D (tetrahedral in 3D).

An unstructured mesh was made for this case, entirely made up of quadrilateral cells. Quadrilateral cells were used for this simple geometry because they can be stretched to account for different flow gradients in different directions. In the present case, the gradients normal to the aerofoil’s wall are much greater than those tangent to the aerofoil. Consequently, the cells near the surface have high aspect ratios.

Patch-based shell meshing offers the best in quad-dominant quality and capturing of surface detail. In ICEM this is why a domain is given a ‘blocking’ structure ahead of calculating the initial mesh, which the user can fine-adjust using, for example, algorithms that expand or contract distances between nodes towards or away from locations of interest.

You define a block model through using ‘split’, ‘merge’, O-grid definition, edge/face modifications and vertex movements. A single ‘C’ grid was very popular before multiblock solvers as this would consist of one block wrapped around. The mesh in this case had an internal and external O-grid and a C-grid around the aerofoil.

Boundaries are placed tens of c upstream and particularly downstream to minimise issues associated with the effect of the farfield boundary (which can particularly influence drag and lift levels at high lift conditions).

For the calculations, whether using a desktop PC or a grid cluster, a mesh is partitioned and the partitioned mesh distributed between two or more compute nodes.

2.7.1 Grid Considerations for a Mesh Dependency Study

Two aspects which constitute a successful CFD computational solution are convergence, of the iterative process, and grid-independency, also called mesh or grid convergence.

When the numerical solutions obtained on different grids agree to within a degree of tolerance set by the user, they are referred to as *grid converged* solutions. By the process of *mesh refinement*, reduction of the cell size causes the solution to be independent of the grid. The numerical error decreases as the number of grid points is increased.

In order to resolve the flow on the mesh near to the boundary layer, an important number for wall spacing for viscous CFD is known as the y^+ (Y plus). It is calculated based on the speed, the medium and predicted dynamic viscosity by the equation $y^+ = \frac{y}{\mu}\sqrt{\rho\tau_w}$ where $\tau_w = \mu\left(\frac{\partial u}{\partial y}\right)_{y=0}$ is the skin friction.

y^+ is the nondimensional distance from the first grid point (the wall-adjacent cell centre) to the wall. The values of y^+ relate to the resolution of the mesh and the Reynolds number of the flow, and are defined only in wall-adjacent cells. The value of y^+ in the wall-adjacent cells dictates how wall shear stress is calculated.

A very small y^+ on the order of 1 is normally advised for steep velocity gradients (we want this distance, where the first grid point is placed, to be within the viscous sublayer - the near-wall region where $y^+ \leq 5$) in order to accurately resolve the boundary-layer behaviour and thus the aerodynamic loads on the aerofoil. And since there was no wall function applied, the height of the first row of cells was set to be at a distance of the order of $10^{-5}c$ corresponding to a y^+ of about 1. The mathematical expressions involved in the designation of the y^+ value can be found in White [44] page 467.

If the mesh is too fine near the wall, there will be too low a value of y^+. This will result in overprediction of the near wall velocity. On the other extreme, if y^+ is too high, it will cause the code to apply the law of the wall to the outer wake where it is not valid.

It is important to investigate the effect of grid resolution in all its respects – wall y^+, number of cells, mesh gradients – and to do this for all CFD simulations.

2.7.2 Mesh Dependency Study

A mesh independent solution is entirely dependent on the mesh employed to capture the fluid flow, and also the physical model that is capable of describing the physics related to the problem. Following the directions above preparations were made for producing accurate simulations by performing a mesh dependency study.

An unstructured quadrilateral mesh was made for an isolated aerofoil profile, which comprised an inner rotating domain and an outer stationary one. The boundary where the rectangular stationary region is connected to the circular rotating region is set as an interface BC in order to employ the sliding mesh technique. The interface is non-conformal; nodes do not match across the interface. These need to be paired up in the solver so that interpolation across the interface can occur. The mesh distance from the top and bottom of the aerofoil to the side boundaries is $55 \times t_{\max}$, the aerofoil thickness. The top/bottom side boundaries in the steady and pitching cases use a slip condition (zero shear), as shown in figure 2.2 for the pitching aerofoil method.

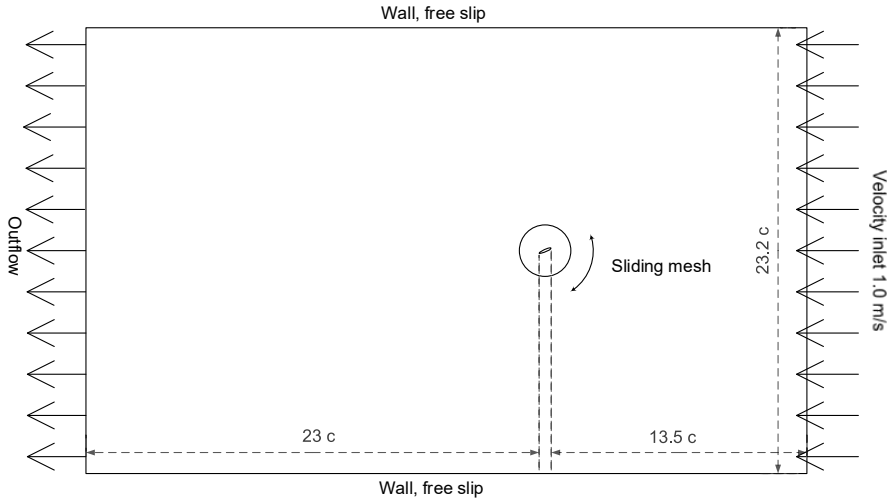

Fig. 2.2 Diagram of domain with sliding mesh and boundary conditions for pitching case

For the oscillating flow case a periodicity was set up between the upper and lower walls for the changing flow direction. This means specifying a periodic relationship between the inflow and outflow boundaries, so that flow characteristics entering a boundary must be identical to the flow characteristics leaving a boundary.

At the liquid-solid interface, a real fluid with non-zero shear viscosity must satisfy a no-slip BC: essentially meaning that fluid molecules are 'adsorbed' to the surface and attain zero velocity relative to the surface. The no-slip condition is specified for the velocity on the aerofoil surface and the freestream values are assigned for the velocity at the upstream boundary (boundary conditions are tabulated in table 3.1.1).

Firstly, a steady test case was made to ascertain what differences might arise from using a mesh interface, later to be used for a 'sliding mesh'. The inner circular domain was rotated in steps of 3 degrees to compare with a simulation whereby the inflow velocity vector was rotated and a mesh with no interface used.

A detail of the mesh is shown in figure 3.5. The near leading edge of the mesh needs to resolve small structures and steep pressure gradients typically observed in this region. Grid clustering in the wake and at the leading edge deformation point is used for accurate flow resolution.

For the ejections simulations to follow a validation study, grid density was added on the suction side for the same reasons as already mentioned.

A dynamic mesh option was tested out. There are three dynamic mesh schemes: smoothing, layering and remeshing. A combination of these would be used to tackle the most

challenging dynamic mesh problems, but for simple dynamic mesh problems involving linear boundary motion, the layering scheme is often sufficient.

2.8 Convergence

No material is truly incompressible, although it is a good approximation. The measure of incompressibility is the divergence of the velocity, $\nabla \cdot v$, which equals the time rate of change of fluid volume per unit volume.

The physical mechanism which leads to incompressible behaviour is the rapid propagation of pressure waves, which must move through a fluid faster than the material speed of the fluid.

Most often the numerical propagation of pressure waves is accomplished by an iteration sheme which couples the pressures to the velocities. The goal of iteration is to reduce the magnitude of $\nabla \cdot v$ below some absolute numerical value, called the convergence criteria.

Convergence is seen by tracking the imbalances that are shown from the advancing of the numerical calculations. These imbalances measure the overall conservation of the flow properties and are known as the residuals. During CFD calculation the residuals can be progressively tracked as the solver iterates, by viewing through the GUI.

These residuals represent the average error in the solution - the smaller the residual, the more converged the solution. There are 3 differential equations to be solved in a 2D incompressible flow problem, and therefore there are three residuals to be monitored for convergence in the laminar problem: continuity, x-velocity, and y-velocity.

Two more residuals are monitored for turbulence depending on the model used. A decrease of the residual by three orders of magnitude during the iterative process is an indication of at least ‘qualitative convergence’.

There are 3 indicators of convergence:

- Residuals less than some agreed order of magnitude: the solution no longer changes.
- Mass momentum balances are obtained (net imbalance should be less than 0.2% of the net flux through the domain).
- In addition to consistency, another property that also strongly governs the numerical solution is stability. This property concerns the growth of decay of errors introduced at any stage during the computation.

How to choose this value depends on the numerical method used.

In this study, convergence criteria for all the different computed quantities were set to below 10^{-6} which was sufficient to produce converged solutions within one time step.

2.8.1 Timestep

The time-step, Δt, applied for the time-marching, is the determining parameter of stability and convergence of the solution. The Courant-Friedrichs-Levy (CFL) condition states the following stability condition:

$$C = \Delta t \sum_{i=1}^{n} \frac{u_{xi}}{\Delta x_i} \leq 1 \tag{2.23}$$

where C is the Courant number, Δx_i is the length interval (i.e. of the cell), and u_{xi} the velocity in the x_i-direction.

The continuity equation (in vector form) is:

$$\frac{d\rho}{dt} + \rho \nabla \cdot \bar{v} = 0 \tag{2.24}$$

and is the mathematical statement of mass conservation. If the fluid is incompressible then ρ = constant, therefore $\frac{d\rho}{dt} = 0$. This means that to fulfil the continuity equation, $\nabla \cdot v = 0$. The discretised form is:

$$\frac{\delta\rho}{\rho} = \delta t \nabla \cdot \bar{v} \tag{2.25}$$

The R.H.S. has the general order of magnitude of:

$$\delta t \nabla \cdot \vec{v} \approx \frac{\delta t \cdot v}{\delta x} \tag{2.26}$$

where δx is the length or size of the discrete elements used in the numerical solution. It is also defined in other sources as the average distance between adjacent grid points or as the 'grid point separation'. This quantity is referred to as the flow Courant number.

$\frac{\delta\rho}{\rho} = \delta t \nabla \cdot \bar{v} = 1$ so $\frac{\delta t v}{\delta x} \approx 1$. If one is exceeded it is seen that the change in density could be greater than the density itself, hence the reason for this constraint on the timestep. This is the reason why the Courant limit is so closely tied to issues of accuracy and stability. It also explains why it becomes more restrictive as the number of dimensions is increased (from one to two, for example). For stability, the accumulated change resulting from fluxes in all directions must not be allowed to change the density (or other quantity) by more than its current value. Thus, with more dimensions there are more fluxes and a smaller timestep size is needed to ensure that elements are not over-emptied.

If the velocity has a component in the y-direction, and the continuity equation is expanded, then the condition becomes:

$$C = \frac{v_x \Delta t}{\Delta x} + \frac{v_y \Delta t}{\Delta y} \leqslant C_{\max} \tag{2.27}$$

where $C_{\max}$ is the maximum Courant number.

The CFL condition being met is a pre-requisite for explicit schemes, but this is not true of implicit schemes. However, it does provide a suitable first estimate for the timestep.

A Courant number of 1 led to a guidance non-dimensional timestep value of close to 0.005. The premise of this number was that the arc distance a single node on the interface of the circular inner mesh moves in one timestep must not be more than the maximum arc distance between nodes. Two timesteps were considered, and a comparison of convergence and calculation results made. The decreased timestep had an effect on convergence per timestep in that convergence occurred in fewer iterations.

Calculations start from an initial flow field obtained from a well-converged steady-state computation where the aerofoil is positioned at the mean angle of attack α_1 and, in order to remove the influence of the initial flow field, a sufficient number of cycles of the aerofoil pitching, or oscillating flow, motion have been calculated until a periodic solution is achieved, which is further proof of a time-independent solution. Other variables monitored for convergence are the lift and drag forces, by checking the time histories of C_l and C_d.

2.9 User Defined Functions

A UDF is, as the name suggests, a function written by the user. It is written in C to perform some additional function on top of the FLUENT-supplied solver-functions.

The DEFINE ZONE MOTION macro used in this case uses a moving mesh or frame motion, rather than a dynamic mesh or mesh motion. DEFINE ZONE MOTION defines node motion. It computes the rotation rate of a cell zone and thus describes the motion of each computational zone.

The UDF for the sliding mesh is:

```
# include "udf.h"

 # define PI 3.14159

 DEFINE_ZONE_MOTION(motion,omega,axis,origin,velocity,time,dtime)
  {
```

```
    velocity[0] = 0.0;
    velocity[1] = 0.0;
    origin[0] = 0.0;
    origin[1] = 0.0;


    *omega =  1.6*0.1806415776*sin(1.6*(time)+(PI/2));
    }
```

For oscillating the velocity, the most convenient way of doing this was to keep v_x a constant value of -1 m/s and set $v_y = \tan(\alpha)$ where $\alpha = \alpha_0 + \alpha_1 \sin(2\pi f t)$ where α_1 is the amplitude respective to the mean angle of attack α_0, and frequency f is found from scaling arguments, this time using the dimensionless parameter k.

$$f = \frac{U_\infty \cdot k}{\pi c} \tag{2.28}$$

The UDF for the oscillating velocity is:

```
# include "udf.h"

# define PI 3.14159

DEFINE_PROFILE(unsteady_yvelocity, thread, position)
{
  face_t f;
    real t = CURRENT_TIME;
  begin_f_loop(f, thread)
    {
      real alpha = (13.3+10.4*sin(2*PI*0.0859*t+(PI/2)))*PI/180;
      F_ PROFILE(f, thread, position) = tan(alpha);
    }
  end_f_loop(f, thread)
}
```

Because of the distance travelled by a packet of the flow during one period, the time it takes for α of the inlet BC to effectively meet the aerofoil LE, Δt, was found by an integration to correct for the delay in onset of α.

For ejections, or 'blowing', an oscillating pressure UDF was written for a pressure-inlet specified at the ejection locations. It is possible to create a UDF that will respond to an excitation condition. This could be:

- excitated amplitude (degrees), or

- excitated frequencies

The equation of the pressure-outlet boundary condition is:

```
DEFINE_PROFILE(blowing, thread, position)
 {
 face_t f;
 real t = CURRENT_TIME;

  begin_f_loop(f, thread)
  {
    if(t < 1.3482)
      {
        F_PROFILE(f, thread, position) = 0;
      }
    else
      {
        F_PROFILE(f, thread, position) = 0.5*(1.0+sin(0.52*(t-1.3482)

        -(2*PI/3)))/2.0;
      }
  }
  end_f_loop(f, thread)
 }
```

They could adapt in such ways as:

- amplitude of pressure fluctuation increases with increasing excitation amplitude.
- Period of pressure fluctuation varies with excitated frequency.

For example, Yan Gu and Yonglin Ju [45] conduct CFD simulations with a UDF in order to understand the periodically oscillating pressure characteristics of inviscid flow in the rolling pipe (to do with floating plants for oil production).

Postprocessing of data was carried out in MATLAB and FLUENT. Complete graphics such as contour plots and animation sequences can be exported from FLUENT.

Chapter 3

Validation Study

The purpose of a validation study is to compare predictions from CFD with real-life experiments. Unlike verification, which seeks to establish that a model has been implemented correctly, validation tests the ability of the model to reproduce the physics. Thus a validation case for the turbulence model is provided.

An aerofoil is chosen for further study for which complete performance data is available in both steady and unsteady form; the NREL (National Renewable Energy Laboratory) S809 [46] 'Airfoil Shapes'.

Ohio State University (OSU) was commissioned to produce experimental data for a range of aerofoil shapes by the NREL. The steady and unsteady experimental data are publicly available on the NREL National Wind Technology Centre (NWTC) Information Portal ([46] 'Airfoil Data').

The validation study to follow compares simulations and experimental data obtained from those databases and the related documents [3, 9]. In the paper by Ramsay [9], unsteady tests used sine waveforms having 2 pitch oscillation amplitudes of ±5.5° and ±10°, with three different mean incidence angles: 20°, 14° and 8°. The wave form is:

$$\alpha = \alpha_0 + \alpha_1 sin(2\pi f t) \tag{3.1}$$

where α_1 is the amplitude respective to the mean angle of attack α_0. The same wave form is used for the sliding mesh to replicate a pitching aerofoil.

Two CFD tests were done in support of this validation study;

1. simulation of pitching aerofoil (P.A.)

2. simulation of oscillating flow (O.F.)

The results of both kinds of motion are shown on the same plot; for example, the graphs of lift and drag coefficients for a reduced frequency k of 0.027, $\alpha_1 = \pm 10$, and $\alpha_0 = 14^\circ$ are shown in 3.7 and 3.6.

Simulations of a pitching aerofoil case are used in the first place because experimental data for validation are available for this type of motion. The reason that a pitching aerofoil is still used in studies of WT aerofoils, like in flight studies for aircraft, is that moving the model is much more manageable than changing the flow.

Although it is the relative flow velocity vector that is changing, rather than the aerofoil moving relative to the freestream velocity, it has been accepted that in principle it is possible to use the relative movement of the oscillating model. However, Carpenter [47] warns that 'there is one very important way in which the shape of the airflow around the object can change substantially even though object shape and size and airflow properties all remain unaltered. This occurs if the relative direction of the airflow changes with respect to the object.' This study will compare the two types of motion; pitching aerofoil and oscillating flow.

3.1 Solution Set-up

The grid is shown in figure 3.5. As shown in figure 2.2, the mesh extends $13.5c$ from the LE to the inlet, and $23c$ from the TE to the outlet. The mesh distance from either the top or bottom of the aerofoil to the side boundaries is 55 x the aerofoil thickness. The top/bottom side boundaries in the steady and pitching cases use a slip condition (zero shear). For the oscillating flow case the side-boundary conditions are similar to the open/non-reflecting condition as used for wave propagation in an unbounded domain. A no-slip BC was specified for the aerofoil surface as described in 2.7.2.

The Reynolds number is 1.0×10^6 based on the chord length of the aerofoil, U_∞ and the viscosity of the fluid. To describe the forces completely, it is required to know M (the pitching moment) about a point. This point is located, as it is often, at $c/4$. Therefore, $c/4$ of the aerofoil is centred on (0,0,0) in the mesh. This is important for the pitching scenario encountered in section 3.3.

Details of the case are provided in table 3.1.1.

3.1.1 Boundary Conditions and Settings

Zone Name			Type/Value
Inlet	*Velocity Specification Method*	Magnitude and Direction	velocity-inlet
	Reference Frame	Absolute	
	Magnitude(m/s)		1
		X-Component of Flow Direction	-1
		Y-Component of Flow Direction	0
	Turbulence Specification Method	Intensity and H.D.	
		Turbulent Intensity (%)	0.05
		Hydraulic Diameter (m)	0.2
	Pressure Initial Gauge Pressure (Pa)		0
Outlet			Outflow
	Gauge Pressure (Pa)		0
	Backflow Direction Specification Method	Normal to Boundary	1
	Loss Coefficient Specification Method	Polynomial	
		Intensity and H.D.	
		Backflow Turbulent Intensity (%)	0.05
		Backflow Hydraulic Diameter (m)	0.2

3.2 Steady Simulation

The lift and drag are the resolved components of the reacting force; lift is a component resolved perpendicular to U_∞ (U_{rel} in figure 3.1) and drag is resolved parallel. The velocity vector was changed to result in a specific AoA, α. This is the angle between the chord line and U_∞ (or U_{rel} in figure 3.1). The local AoA is given by; the pitch of the aerofoil, θ; axial velocity and rotational velocity at the rotor plane - denoted respectively by U_a and U_{rot}. The flow angle is found as $\tan\phi = U_{\text{a}}/U_{\text{rot}}$.

Since Fluent calculates force vectors based on the geometry, and therefore does not account for influences on the flow at the inlet and in the fluid interior, a transformation matrix;

$$\begin{bmatrix} x' \\ y' \end{bmatrix} = \begin{bmatrix} \cos\theta & -\sin\theta \\ \sin\theta & \cos\theta \end{bmatrix} \begin{bmatrix} x \\ y \end{bmatrix}$$

corrected the lift and drag vectors on the aerofoil.

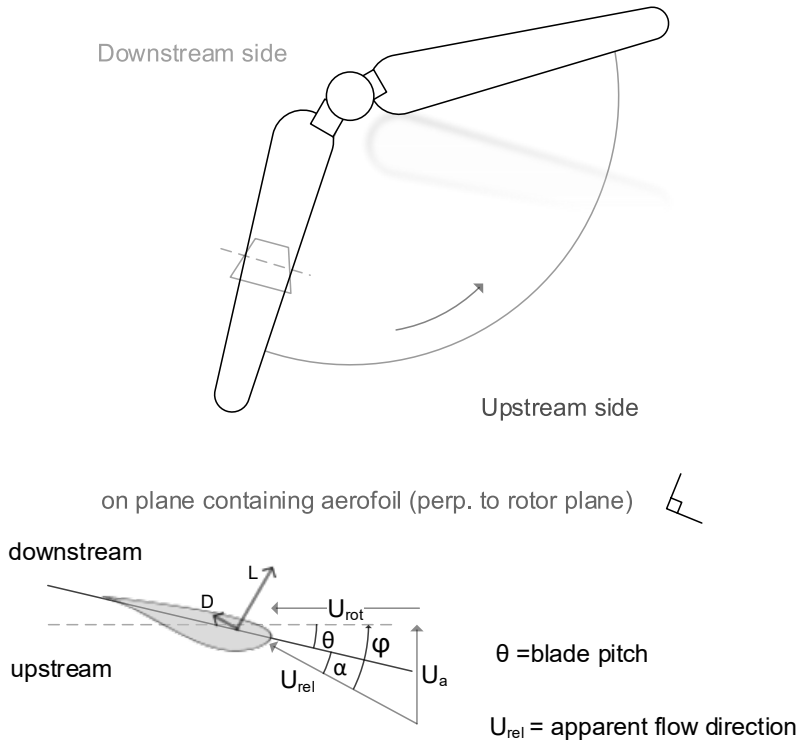

Fig. 3.1 Blade cross-sectional view: – U_{rot} is in rotor plane and aerofoil plane. – U_{a} is in aerofoil plane and points into rotor plane. – U_{rel} is the incoming velocity 'seen' by the aerofoil.

3.2.1 Static aerofoil results

Figures 3.2a and 3.2b show the lift and drag curves obtained by simulation using the Fluent code, compared to the steady-state experiments for the S809 at a *Re* of 1.0×10^6 by Somers [3] in the Delft WT, and Ramsay [9] in the OSU WT, for a Reynolds number of 1.0×10^6. The simulation presented was run as steady state below the static stall angle and unsteady above for reasons explained below.

The residuals, that are monitored for convergence, for $\alpha = 0^\circ$ are shown in figure 3.3. The higher angles of attack should be run unsteady to achieve convergence because at the static stall angle, the laminar BL separates, and there is significant temporal variation as the separated, yet still laminar, flow is highly sensitive to disturbances. The values obtained are no longer a snapshot in time that would be similar for any instant and the results cease to resemble a steady situation. As Somers points out, higher C_L than $C_{\mathrm{L}_\mathrm{max}}$ at higher AoA may be reached but these values are not to be entirely trusted; '(...Such massive separation suggests that the validity of the data is suspect.)' [3, p.10].

The two sets of experimental data from different sources - Ramsay et al. [9] and Somers [3] - are plotted to give an indication of how data can vary from one experiment to the next even under tightly controlled conditions. Part of the explanation is the subtle differences in background TI from one wind tunnel to the next.

The lift curve in figure 3.2a shows reasonably close agreement between simulation and experiment at low α. The double 'hump' seen for the experimental lift curve of this aerofoil is reproduced to an extent in the simulation, but its occurrence is diminished and delayed somewhat. The stall is therefore not predicted well, and the curve appears to resemble the lift curve that might be expected of a higher TI.

There was no provision of measurements of the FST level in the wind tunnel in unsteady experiments by Ramsay et al. [9]. Those experiments were conducted in the OSU/AARL 3'x5' subsonic wind tunnel. A look at the OSU facilities webpage has that the TI level is 'less than 0.1%'.

It is referred to the experimental conditions for the steady experiments by Somers [3], under similar test conditions, but this time with the wind tunnel as the TU Delft low-turbulence wind tunnel, as being 'generally below' 0.05%. Under the section titled 'Wind Tunnel', it states that 'the turbulence level in the test section varies from 0.02 percent at 10 m/s (33 ft/s) to 0.04 percent at 60 m/s (200 ft/s). This would suggest a TI of about 0.033%. But it was important to try to match the TI for the unsteady experiments as best possible in the absence of measurements, therefore the turbulence intensity at the inlet BC was set at 0.05%.

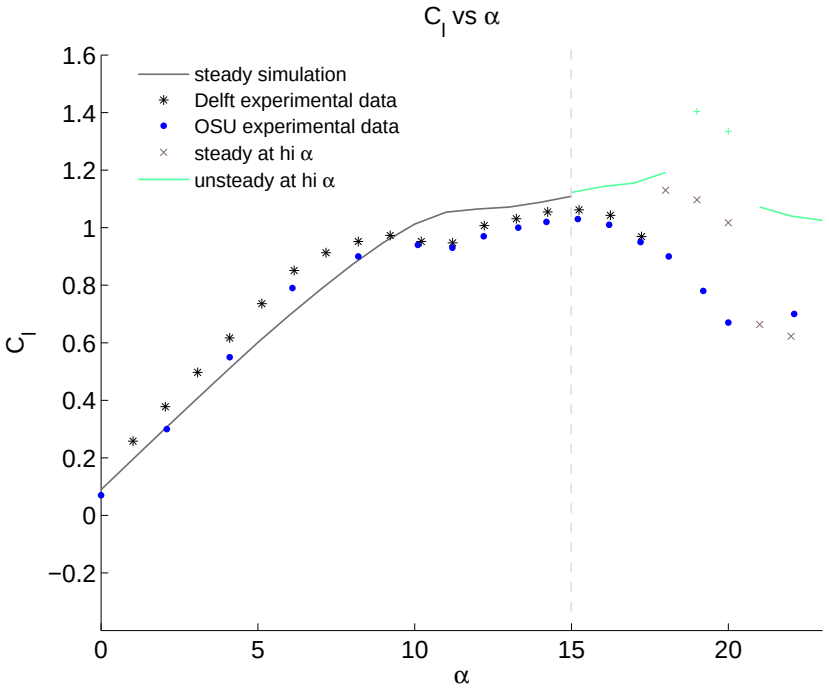

(a) Steady lift curves comparison - for α before dotted line, simulation was run steady and beyond run transient

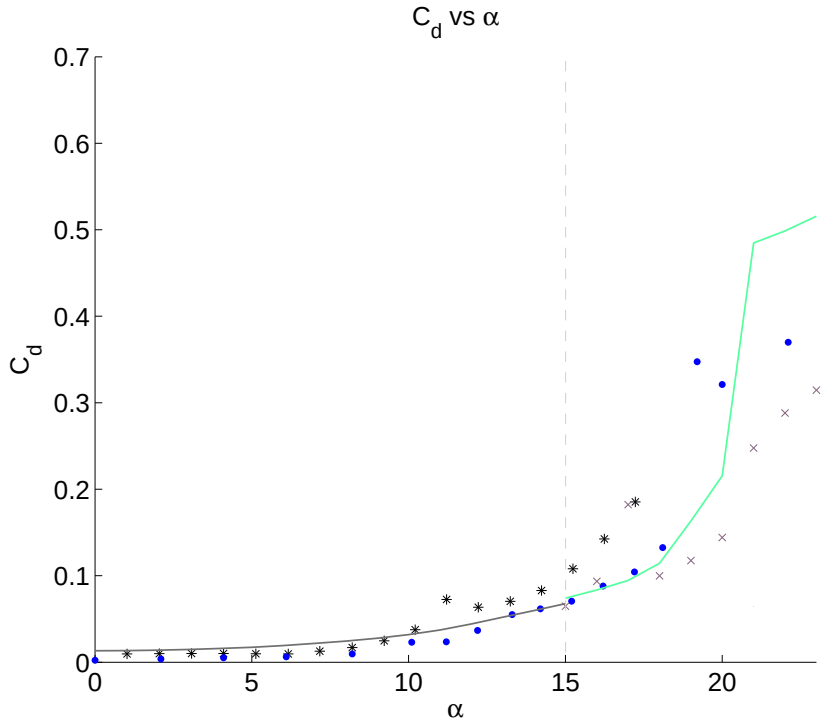

(b) Steady drag curves comparison - for α before dotted line, simulation was run steady and beyond run transient

The slope $\frac{\Delta L}{\Delta \alpha}$ is predicted quite well. The CAD-model S809 for this study had the TE thickened to 1.25mm by adding to the upper surface over the last 10% of the chord. This was done as described in the section 'Model Details' of Ramsay et al. [9]. Therefore it was expected that the slope should closely resemble that of the experimental curve.

Cross markers in green show outliers in the transient-simulated values of C_l. Running the simulation unsteady is not enough to guarantee a realistic solution, as it is probable that 3D effects are more prevalent at separated α.

The drag curve in figure 3.2b shows very good agreement with experiment at low α but also overpredicts at the higher α of 21° and beyond.

The crosses in grey represent the steady results for the same region of α where the unsteady results were questionable. The steady simulation C_l here follow the shape of the stall.

The steady simulation did not converge at 16° or 17°. There is an increase in lift predicted by the transient results at high AoA probably due to turbulence effects. Turbulence enhances the tendency of attachment which would lead to enhanced lift. It is apparent that the model has predicted transition and switched to the SST Transition model (with the Intermittency Transition Model) and both the steady and unsteady results overpredict $\alpha_{\max}$ for static stall. Both steady and unsteady simulations also overpredict lift at high α.

This might have been cause for concern about the agreement, but the unsteady pitching results in 3.3 showed very good agreement with the exact same model.

A better understanding of how good the model is might be gleaned from convergence. Looking at the time-histories for 15°,16° and 17° in figures 3.4a and 3.4b it is seen that there is adequate convergence.

The top right plot of lift time-history for 18°, shows that there is some simple oscillatory time-variation of the solution - this is more pronounced for C_l than the corresponding plot for C_d at 18°, 3.4b.

The third plot (left to right) shows that the amplitude of the oscillations increase with increasing AoA. Some quasi-periodic wave patterns begin to emerge after 20°. This periodicity is more easily seen in the bottom right plot for 21°-23° in 3.4b. It is not known why the C_d time-history oscillations are smaller than C_l.

Obtaining a value is possible if a periodicity appears. A periodicity means that it is possible to reproduce the flowfield. The values of lift and drag can be extracted by averaging the values over a number of periods. This can be done by treating the time-history data as a discrete periodic 'signal', then, using a Fourier Transform (FT), converting the signal from the time domain to the frequency domain (spectrum). The spectrum shows what proportion of

the signal lies within each given frequency band over a range of frequencies. The proportion with the highest frequency gives the best value.

As mentioned in Chapter 2, the physical mechanism which leads to incompressible behaviour is the rapid propagation of pressure waves, which must move through a fluid faster than the material speed of the fluid and pressure-velocity coupling accomplishes the numerical propagation of pressure waves. Here the convergence reflects the fact that there are unsteady processes in the flow and very steep pressure gradients.

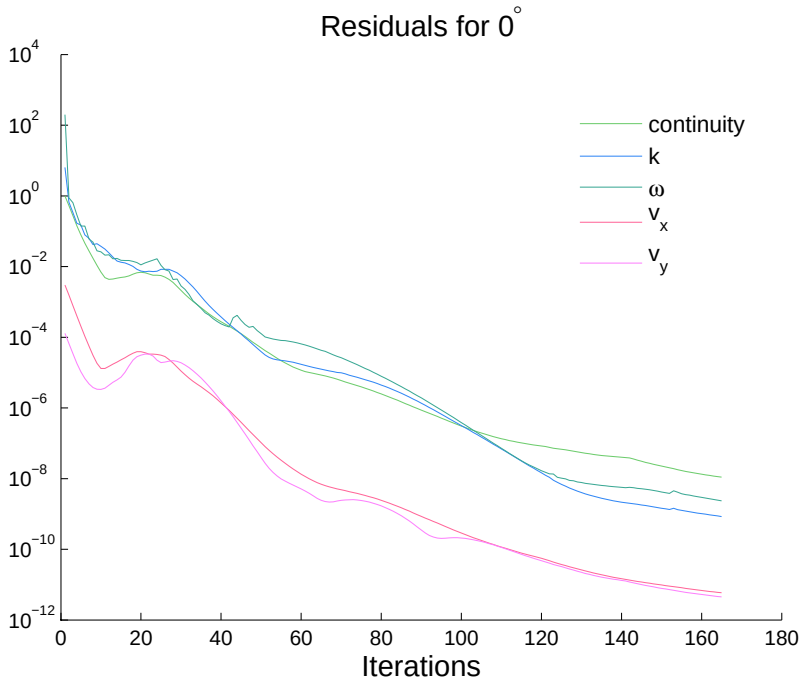

Fig. 3.3 Residuals for 0°

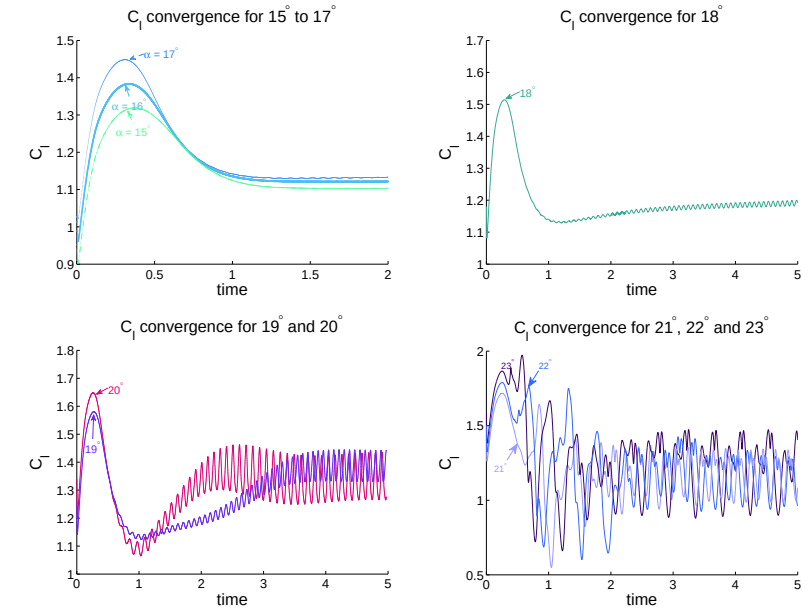

(a) Lift Convergence

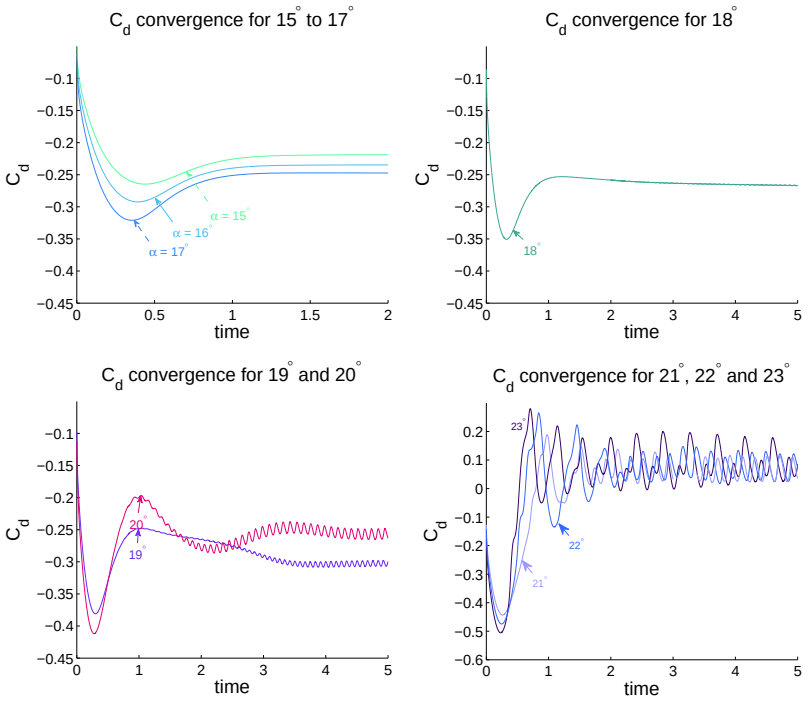

(b) Drag Convergence

Fig. 3.4 Convergence for steady validation simulations

3.3 Pitching Aerofoil and Oscillating Flow Simulations

The sliding mesh was composed of an inner circular domain containing the aerofoil, and an outer domain which always remains stationary. Figure 3.5 shows the domain in a close-up of the interface region.

Sinusoidal oscillatory motion is considered in the absence of a computational analogue for turbulence; it is modelled in a cyclic manner largely for convenience. Sinusoidal motion is often considered in the body of research pertaining to turbines as it is also close to the incidence variations experienced by a real blade in marine/wind turbine aerodynamics.

In a rotational frame of reference fixed on the turbine blade, the blade will see a cyclic variation in the effective flow velocity and the AoA, as shown in figure 3.1. Wang et al. [15] write that 'this is very similar to what would be seen by a sinusoidally pitching blade in a stationary frame of reference.' However, this study will show that there are also substantial differences between the relative types of motion, pitching aerofoil and oscillating flow, shortened to PA and OF (this notation will be used throughout).

The mechanics strongly depends on a number of parameters, such as aerofoil shape, mean angle α_0, amplitude of oscillation α_1, and reduced frequency k. Therefore the experimental data were examined and for example, where the measured α indicated a slightly different α_0, an adjustment was made to the UDF to attempt to match the experimental data as well as possible.

The details of each simulation run are given in table 3.1 below:

Table 3.1 Details of simulation runs

		Mean AoA		Amplitude		
	Figures	$\alpha_0(^\circ)$	actual $\alpha_0(^\circ)$	$\alpha_1(^\circ)$	actual $\alpha_1(^\circ)$	k
large amplitude oscillations	figs 3.7 and 3.6	14	13.3	$\pm$10	$\pm$10.4	0.027
	figs 3.8 and 3.9	14	12.65	$\pm$10	$\pm$10.35	0.08
moderate amplitude oscillations	figs 3.10a and 3.10b	8	8.45	$\pm$5	$\pm$5.05	0.026
	figs 3.11a and 3.11b	8	8.35	$\pm$5	$\pm$4.95	0.077

All pitching aerofoil and oscillating flow simulations are in figures 3.6 - 3.13 (figs. 3.6, 3.7, 3.8, 3.9, 3.10b, 3.10a, 3.11a and 3.11b). What follows is a mainly qualitative commentary on the results.

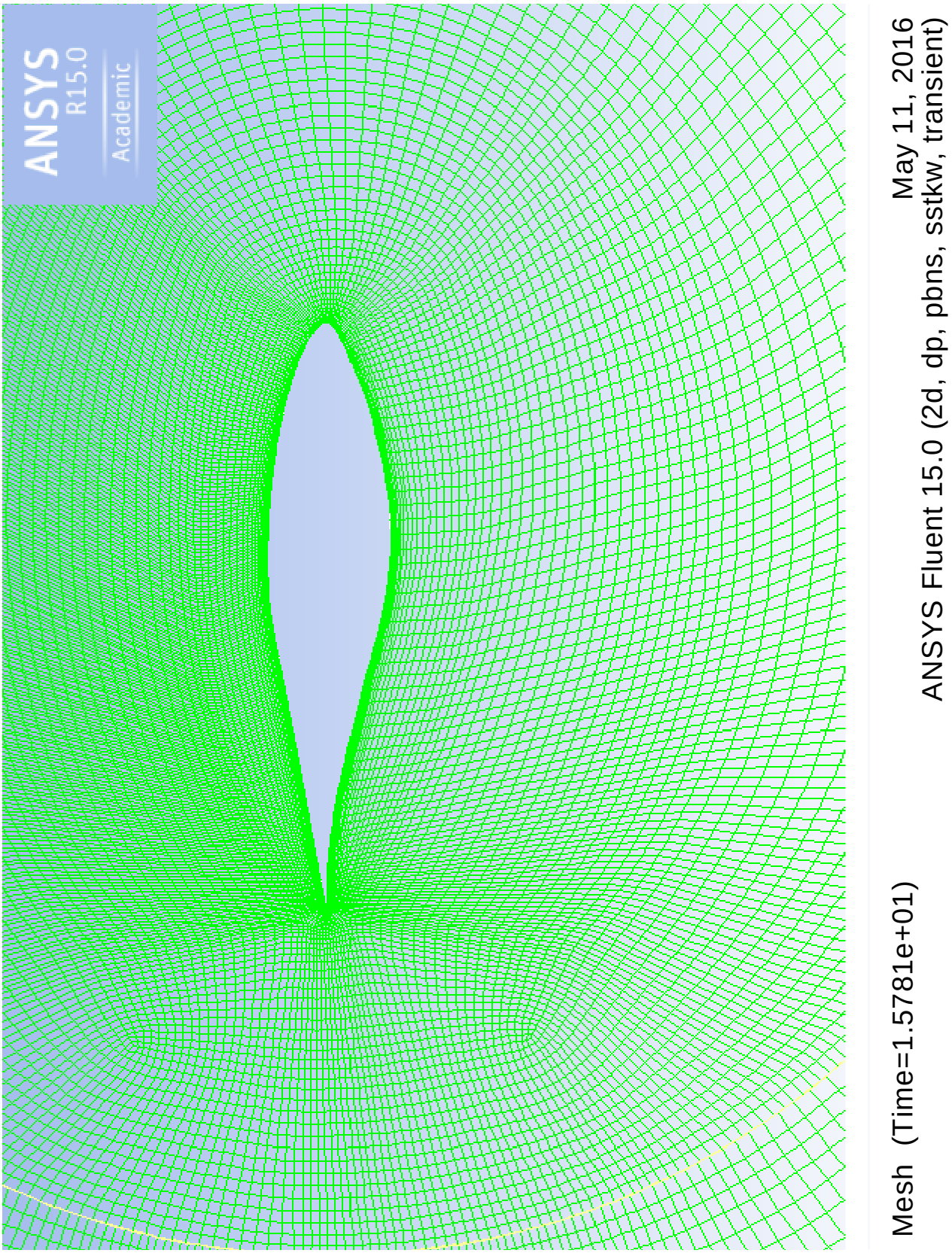

Fig. 3.5 Image of domain

3.3.1 High AoA oscillation simulations

Simulations for the S809 were pitted against OSU experimental data. First of all, for a reduced frequency of 0.027, with a $\pm 10^\circ$ pitch oscillation and a mean angle of 14°, then for a reduced frequency of 0.08.

Low Reduced Frequency

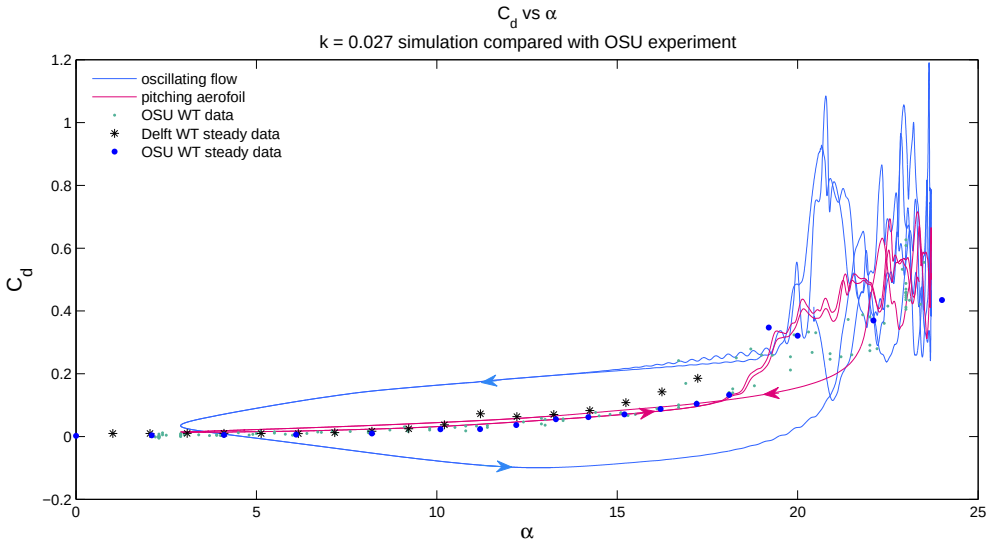

Fig. 3.6 C_D vs. α comparison with experiment, oscillation amplitude $\pm 10^\circ$, $\alpha_{mean} = 14^\circ$, $k = 0.027$.

Figure 3.7 and figure 3.6 show hysteresis curves for the lift and drag coefficients respectively, for $k = 0.027$, $\alpha_0 = 14^\circ$, $\alpha_1 = \pm 10^\circ$.
The equation of the oscillation is $\alpha \equiv \alpha_0 + \alpha_1 \sin(2\pi f t)$.

The starting point for the simulations along the increasing AoA branch of the graph is an attached flow, whereas it is a massively separated flow at very high α. This indicates that 'deep stall' has taken effect. The hysteresis was found to be clockwise in the lift coefficient profiles and counter-clockwise in the drag coefficient profiles.

The unsteady component of the aerodynamic coefficients seen in figure 3.7 for the oscillating flow (OF) case (blue) at the high angles is significantly larger than that for the pitching aerofoil (red) case for both increasing and decreasing α.

The drag for the pitching case is very close to experiment. The oscillating flow exhibits a lot of hysteresis and deviates from the experiment a lot on the whole, but if one were to imagine a median line for the flow drag, the line would also reside very close to the experimental results.

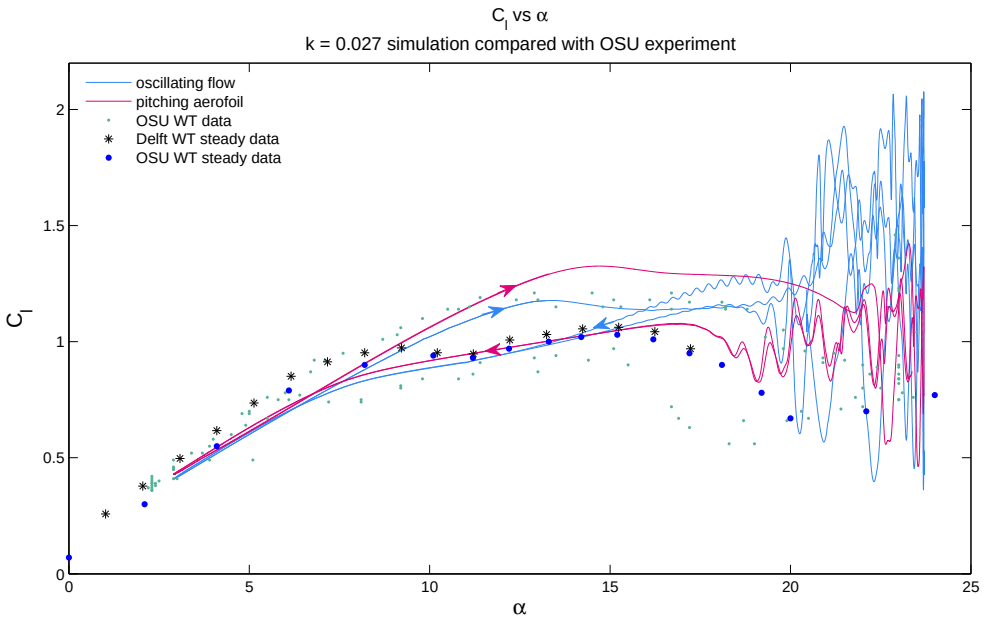

Fig. 3.7 C_{L} vs. α comparison with experiment, oscillation amplitude $\pm 10^{\circ}$, $\alpha_{\mathrm{mean}} = 14^{\circ}$, $k = 0.027$.

It is known that a narrow hysteresis loop implies a *small* amount of dissipated energy in reversing a variation, caused by adjusting to new inputs, to the initial state. With this in mind it would appear from all pitching aerofoil/ oscillating flow simulations that, in general, there is more energy dissipated in the oscillating flow case.

Pre-Stall: Increasing AoA branch As can be seen from figure 3.7 on the **increasing AoA branch**, the lift is in some areas better represented by the oscillating flow (OF) simulation than by the pitching aerofoil (PA) - namely 10° and beyond. C_{Lmax} for OF, the angle of static stall, α_{max}, and the prediction of stall afterwards, is close to the experimental results from Ramsay et al. [9].

On the other hand, the *amount* of hysteresis for the PA simulation is more representative of the experiment, but the lift is excessive. The loop appears as if translated upwards, and stall delayed more: α_{max} is beyond that of the experiment.

It looks as though the PA is subjected to higher turbulent conditions - although both simulations have identical conditions except for the type of motion-UDF imposed. The simulations may have a slightly higher background TI than the experiment for the reason of the FSTI at the boundary being set as described in subsection 3.2.1. However, results for the

higher k simulation to follow do not support this hypothesis. Also, a short but by no means exhaustive study of different inlet FSTI values did not show substantial differences for TI values less than 1%.

Wang et al. [15] (and Hoffmann [6]) observe that fluctuations of the numerically-predicted coefficient progressively smooth-out with increasing free-stream turbulence-intensity (FSTI).

They cite a reason for this as being the improved energy transfer across the boundary layers, delaying the laminar-to-turbulent BL transition as well as the flow separation.

Increasing FST is also known to prolong TBL attachment, delay dynamic stall, increase $\alpha_{\max}$, and enhance $C_{\mathrm{L}\max}$.

However, the plot for oscillating flow does not suggest a higher FST. It could be that the aerofoil in the OF case is not subjected to as high turbulence as the PA case.

Indeed, the authors find that increasing the FST level improves the stability of the predicted forces. The PA simulation certainly *appears* more stable in figures 3.6 and 3.7. It is well known that the k-ω models, and others, are less stable at low Re. The model is very sensitive for unsteady, low TI applications. There are models that have been formulated to improve stablity at low TI.

Post-stall: decreasing AoA branch The location of $\alpha_{\max}$ is roundabout 17°-18°. On the downstroke this location corresponds to the 'hysteresis lift' as detailed by Ramsay [9, p.13]; 'To obtain some measure of this hysteresis behavior, the lift coefficient on the "return" portion of the curve, at the angle of attack where maximum lift coefficient occurs, can be used...Note the angle of attack where the maximum lift coefficient occurs does not necessarily show the greatest hysteresis behavior but does give a relative indication of the effect.'

The hysteresis lift $C_{\mathrm{L}\mathrm{hys}}$ for oscillating flow is higher than for the pitching aerofoil: it also rivals $C_{\mathrm{L}\max}$ for flow on the upstroke.

There is a sudden increase in lift coefficient near 19°, before $C_{\mathrm{L\,hys}}$ during the **downstroke**. This seems to occur slightly in advance for the OF results as compared to the PA results. This lift increase on the downstroke, for both simulations, happens prior to the corresponding increase in experimental lift.

Wang et al. [15] attribute this to the generation of a secondary vortex. The point of occurrence of this sudden lift in the OF simulation, and the fact it exceeds $C_{\mathrm{L\,max}}$, may indicate the phase of the normal force is shifted to the right. However, this is not conclusive,

as the fact remains that the point of stall and $C_{\mathrm{L\,max}}$ compare well to the experiment.

The reattachment is predicted well by both numerical simulations, however C_d for the OF indicates something else happening: with C_d crossing the axis into negative figures, this must mean there are forces propelling the aerofoil to the right. This might be explained in terms of wave-resistance, which is frequently distinguished from the 'form drag'. The researchers also mention the point of intersection between the upstroke and downstroke paths in their simulation results, which was found also in the experimental results they compare them with, from Lee and Gerontakos [18]. This happens about a degree earlier for the PA case here.

Summary In both cases, pitching aerofoil (PA) and oscillating flow (OF), and for both lift and drag, the numerical results have a much larger difference from the experimental data at high α ($20^\circ < \alpha < 25^\circ$).

The unsteady component of the aerodynamic coefficients for the OF simulation (blue) is also significantly larger than that for the PA simulation, which appears more stable.

This unsteadiness is greater during the *decreasing* AoA branch, a feature in common with the hysteresis for a static aerofoil, as described in the Literature Review, 1.2.1, and in agreement with other unsteady experiments.

The OF simulation better predicts $\alpha_{\max}$ and its corresponding lift coefficient value $C_{\mathrm{L}\max}$ before DS. The pitching aerofoil better replicates the hysteresis. Both PA and OF curves exhibit significant hysteresis and both predict the stall angle rather well, as well as other attributes of the experimental curve, like the jump in lift in the early portion of the downstroke.

Using the moment data, the pitch-damping parameter (see 3.3.3 Discussion) for the OF is about 50% higher than for PA; work done *by* the fluid *on* the aerofoil is greater for OF.

Integrating the lift and drag over a complete cycle gives the same result for PA and OF for the lift, but the OF drag is several times greater. These results might not be meaningful given the spurious numerical oscillations at high α.

The appearance of the PA simulation being more stable, and having a higher $C_{\mathrm{L}\max}$, $\alpha_{\max}$ and, all in all, a later dynamic stall event, suggests FST at the inlet boundary was in excess of the experimental conditions, but this is not reinforced by the good agreement of the OF simulation.

High Reduced Frequency

For the plot of C_l in figure 3.9, the $k = 0.08$ case (α_0 = 14° , $\alpha_1 = \pm 10°$), it can be seen that $C_{\mathrm{L\ max}}$ and higher experimental lift coefficients are better represented by the results for the pitching aerofoil (PA). This in contrast to the $k = 0.027$ simulation (figure 3.7) whereby better prediction was attained by the results for oscillating flow (OF).

The experiment stall angle $\alpha_{\max}$ is predicted best by the OF results again, while it is overpredicted by the PA results. There is less unsteadiness at high α. There is more hysteresis (i.e. a larger hysteresis loop) with the higher k as is expected [9].

Figure 3.8 shows that the spike in the drag coefficient at the maximum AoA is captured by the PA simulation. The degree of reattachment at low α is predicted well in the PA case but for the OF case, reattachment only occurs when the aerofoil terminates/changes direction at the lowest α. Hence, the C_l hysteresis loop is rounded at the lowest part of the cycle. This is because the flow is constantly being pushed along and molecules of fluid are feeling pulled and pushed by the effects of other molecules, leading to a diluted sense of 'pitching'.

The flow would have to be oscillating at a lesser frequency to allow time for the fluid to settle, or adjust to its inputs, and this is seen by observing the closer agreement between pitching aerofoil and oscillating flow for the $k = 0.027$ case in figure 3.7.

Net work is done *on* the fluid *by* the PA over one cycle in this case as indicated by the pitch-damping parameter, τ_0. More work is done by the fluid on the aerofoil in the OF case. Again integrating the lift over a complete cycle yields about the same for PA and OF; the drag is about $3\frac{1}{2}$ times greater for OF.

The phase of the OF curve again looks as though it has been shifted to the right (and this time further so) as for an increase in k. At least it appears like this partially, because the upstroke portion is in-keeping with the dynamics.

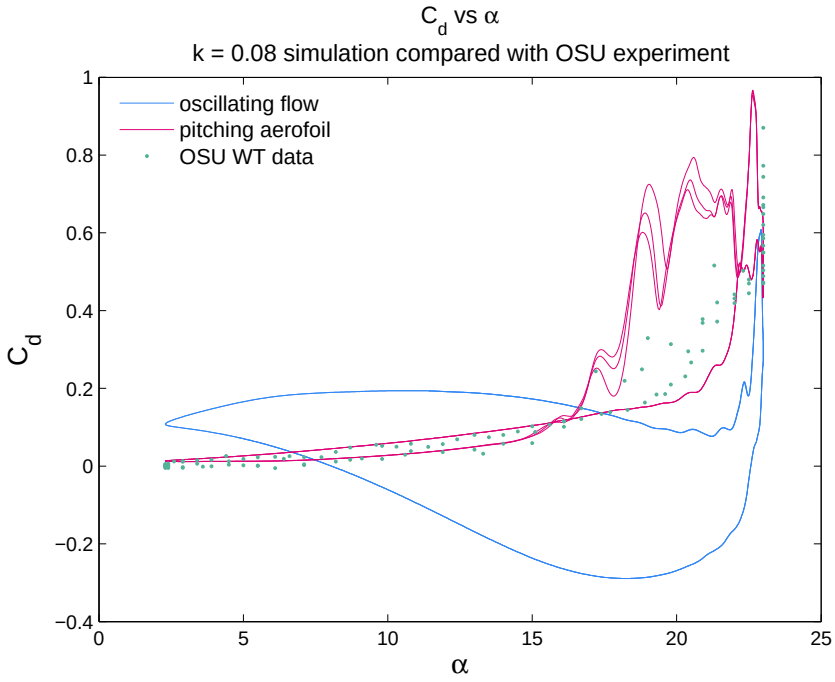

Fig. 3.8 C_{D} vs. α comparison with experiment, oscillation amplitude $\pm 10^{\circ}$, $\alpha_{\mathrm{mean}} = 14^{\circ}$, $k = 0.08$.

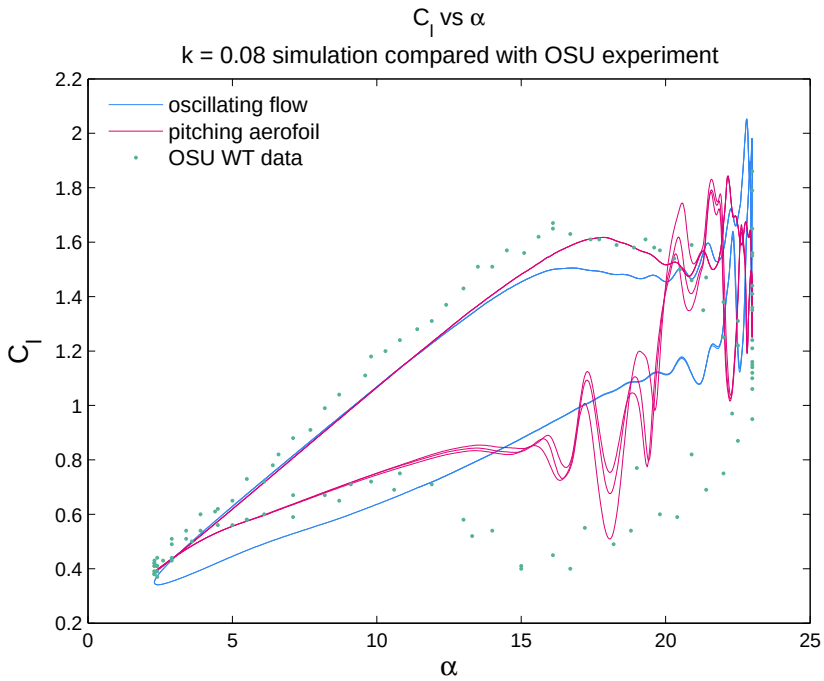

Fig. 3.9 C_{L} vs. α comparison with experiment, oscillation amplitude $\pm 10^{\circ}$, $\alpha_{\mathrm{mean}} = 14^{\circ}$, $k = 0.08$.

3.3.2 Moderate AoA oscillation simulations

There is much less unsteadiness evident in these plots due to the fact that, with respect to the range of angles of attack of this motion, this hysteresis loop terminates, or changes direction, before the angle of static stall. Hysteresis is observed for aerofoils at around the angle of static stall, and the less the maximum AoA is than the angle of static stall, the smaller the hysteresis loop.

Low Reduced Frequency

Figures 3.10a and 3.10b show the lift and drag hysteresis curves for $\alpha_0 = 8^\circ$, $\alpha_1 = \pm 5^\circ$ and $k = 0.026$.

In figure 3.10b, the shape of the simulation lift curve is concave on the downwards branch while the experimental curve is more convex. However, the degree of reattachment at low α is predicted well by both and the stall is also predicted well.

There is no dynamic stall present in this case, but from the oscillating flow (OF) simulation, there could be a slight phase shift before the maximum AoA resembling the low k simulation in 3.3.1.

For the pitching aerofoil (PA) simulation, there is a tongue of the low α where the branches intersect, as in 3.3.1, but which does not occur for the OF simulation. Although this intersection bears no resemblance to the experimental curve.

High Reduced Frequency

Figures 3.11a and 3.11b show the lift and drag hysteresis curves for $\alpha_0 = 8$, $\alpha_1 = \pm 5$ and $k = 0.077$.

Again there is a intersection between the upstroke and downstroke branches at low α in the PA curve which is not replicated in the OF curve. A phase shift looks more apparent for the OF curve than for the high k simulation of 3.3.1.

In terms of τ_0, the reverse is true of the moderate AoA cases. For PA fluid is indicated to be doing work on the aerofoil and more so than for OF. Integrating the lift and drag shows that OF generally produces more lift and more drag.

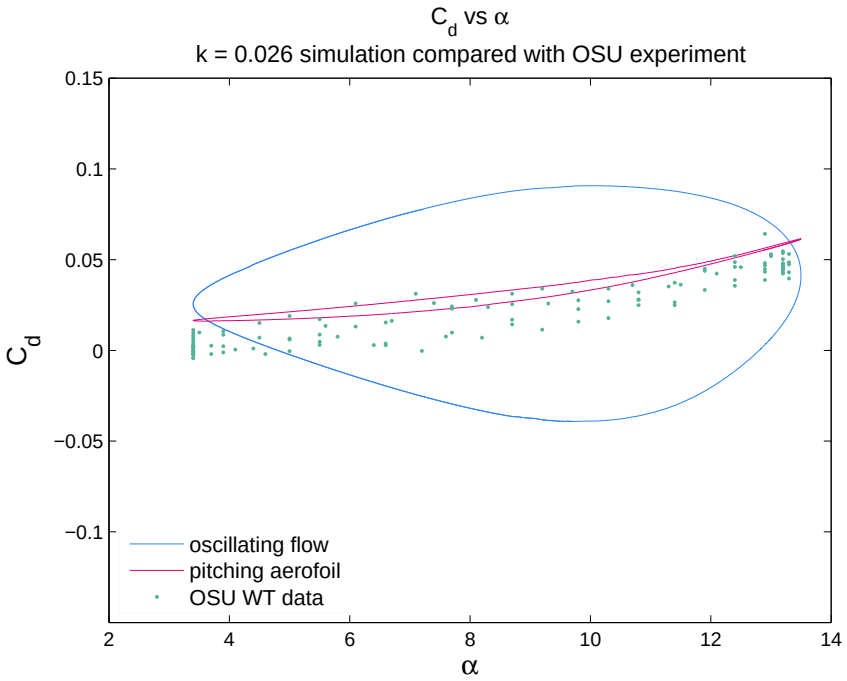

(a) C_{D} vs. α comparison with experiment, oscillation amplitude $\pm 5^{\circ}$, $\alpha_{\mathrm{mean}} = 8^{\circ}$, $k = 0.026$

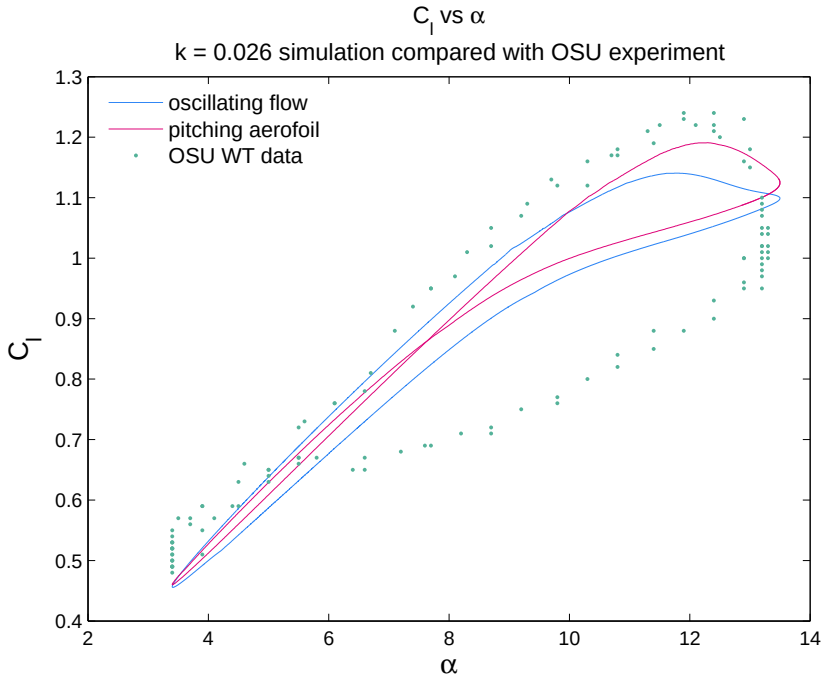

(b) C_{L} vs. α comparison with experiment, oscillation amplitude $\pm 5^{\circ}$, $\alpha_{\mathrm{mean}} = 8^{\circ}$, $k = 0.026$.

Fig. 3.10 C_{D} and C_{L} vs. α comparison with experiment, oscillation amplitude $\pm 5^{\circ}$, $\alpha_{\mathrm{mean}} = 8^{\circ}$, $k = 0.026$

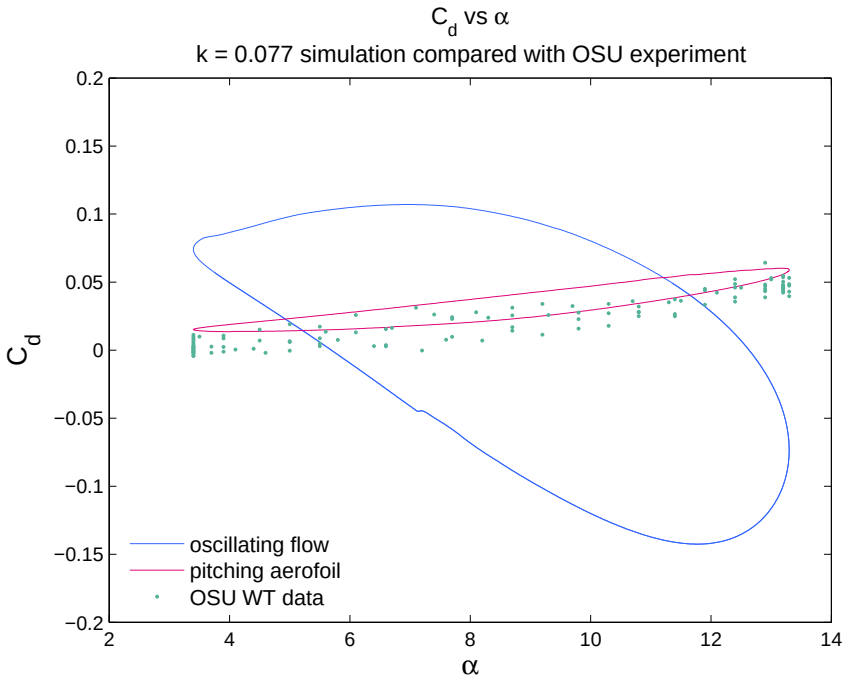

(a) C_{D} vs. α comparison with experiment, oscillation amplitude $\pm 5^{\circ}$,$\alpha_{\mathrm{mean}} = 8^{\circ}$ $k = 0.077$.

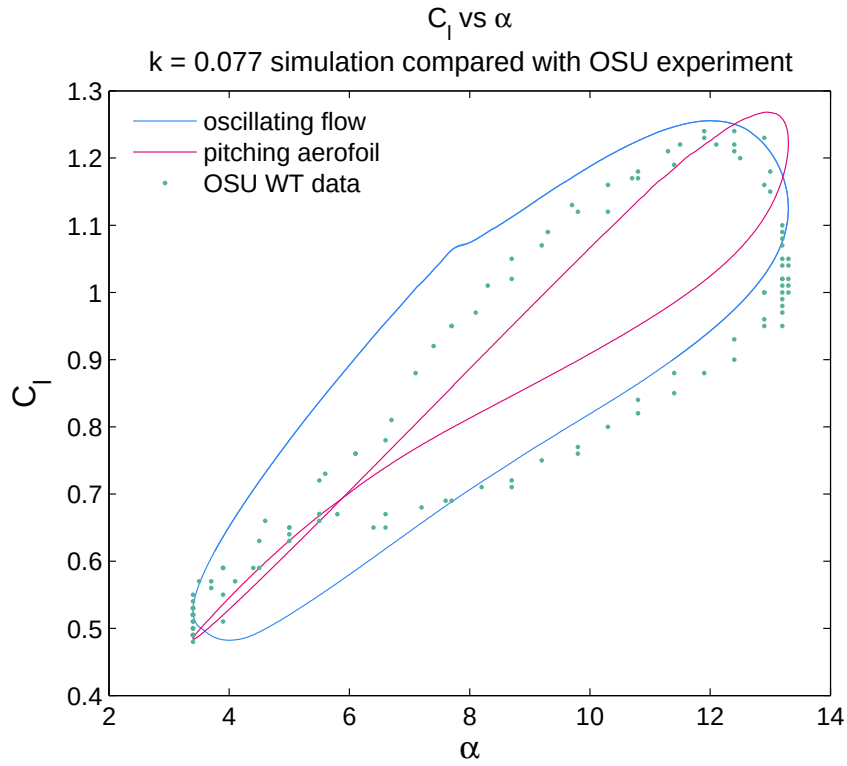

(b) C_{L} vs. α comparison with experiment, oscillation amplitude $\pm 5^{\circ}$, $\alpha_{\mathrm{mean}} = 8^{\circ}$, $k = 0.077$.

Fig. 3.11 C_{D} and C_{L} vs. α comparison with experiment, oscillation amplitude $\pm 5^{\circ}$, $\alpha_{\mathrm{mean}} = 8^{\circ}$, $k = 0.077$

3.3.3 Discussion

For the pitching aerofoil case, a second cycle is needed to develop the hysteresis when the aerofoil is first put in motion. For both pitching aerofoil (PA) and oscillating flow (OF) cases, three model oscillation cycles are preferential to develop the form of hysteresis. The plots are of the hysteresis after three model cycles had elapsed. Closeness of predictions by the simulations to the experimental results varies from case to case but overall some very good agreements are seen.

The OF case was initialised so that the flow field corresponded to the starting point of the OF UDF 2.9.

Going along the curve branch corresponding to increasing AoA, an increase in the maximum C_{Lmax} is seen, compared to the static-aerofoil lift curve. During the unsteady simulations, an increase in the maximum lift coefficient of up to 60% was observed.

For the first two cases where the static stall angle is exceeded, stall is slightly delayed. Best agreement is seen by PA, overall, as is to be expected, since this is the motion performed in the experiment.

Deep stall was observed for 3.3.1, High AoA oscillation simulations: $\alpha_0 = 13.3^\circ$, $\alpha_1 = \pm 10^\circ$, going along the branch corresponding to a decreasing AoA. See figures 3.7 and 3.6.

The unsteady component of the aerodynamic coefficients seen in figure 3.7 for the oscillating flow case (blue) at the high angles is significantly larger than that for the pitching aerofoil (red) case. In general, sizes of the hysteresis loops are larger for the OF curves, especially as regards the drag coefficient...

The curve for the drag coefficient for oscillating flow takes a very wide path and strays across the x-axis (y=0) at varying points during the cycle, into negative figures. This can be seen in all cases for C_d for oscillating flow. This would seem to suggest that there is a force accelarating the aerofoil forwards, instead of pushing back on the aerofoil as elsewhere. This could be due to wave resistance, since the oscillating flow exhibits wave-like motion.

The net aerodynamic work per cycle of oscillation for a pitching aerofoil is:

$$dW = -Md\alpha \tag{3.2}$$

It represents the instantaneous work done on fluid by the body due to its motion, where W stands for work, M the pitching moment about the axis of rotation which is positive for 'nose-down' airloads. McCroskey [48] states that: 'Although the product of $C_m d\alpha$ is normally negative, during some phases of dynamic stall it can become positive, so that the

fluid is doing work on the body instead of vice versa.' The pitch-damping parameter is defined in [48] as:

$$\tau_0 = -\oint C_m d\alpha / 4{\alpha_1}^2 \tag{3.3}$$

and is a measure of the work done.

For the high AoA cases τ indicates that there is more work is done by the fluid on the aerofoil in the OF case; there seems to be a tendency for the oscillating flow to amplify the oscillations in AoA experienced by the aerofoil, especially for higher k. This is not seen in the results.

However, for the moderate AoA cases the situation reverses; more work is done by the fluid than the pitching aerofoil in deflecting the fluid. The aerofoil extracts less energy from the fluid for OF in these cases.

The phase of the OF curve looks as though it has been shifted to the right. The point of occurrence of the secondary vortex-induced lift in the OF simulation in 3.7: the fact its occurrence is delayed with respect to both the PA simulation and the experiment, and the fact it exceeds $C_{\mathrm{L\,max}}$, may indicate the phase of the normal force is shifted to the right.

There is clearly a difference in the two types of motion. Grace [49, p.3] says, when discussing an aerofoil encountering a vortical disturbance; 'For the case of an airfoil interacting with a vortical disturbance, arriving at the boundary condition along the airfoil is a bit different than for the case of the oscillating airfoil' and mentions that the unsteady velocity field is split into two parts: rotational and irrotational.

3.3.4 Snapshot pressure coefficient plots

Figure 3.12 shows markers at corresponding locations on the plot of figure 3.9 from 3.3.1, for the upstroke ↑ and downstroke ↓ of both oscillating flow (OF) and pitching aerofoil (PA) cases, at which surface pressure coefficient - C_p - distribution plots are compared.

The 3.4° location on the plot corresponds to roundabout the angle of reattached flow.

The 13.5°-15.1° locations are on the lead-up to the angle of the maximum pre-stall lift coefficient - $C_{L\mathrm{max}}$ - for the steady case, and are also approaching the angles of maximum lift coefficient - $C_{L\mathrm{max}}$ - of the unsteady cases (there is a different angle at which the unsteady $C_{L\mathrm{max}}$ occurs for the pitching aerofoil/oscillating flow case).

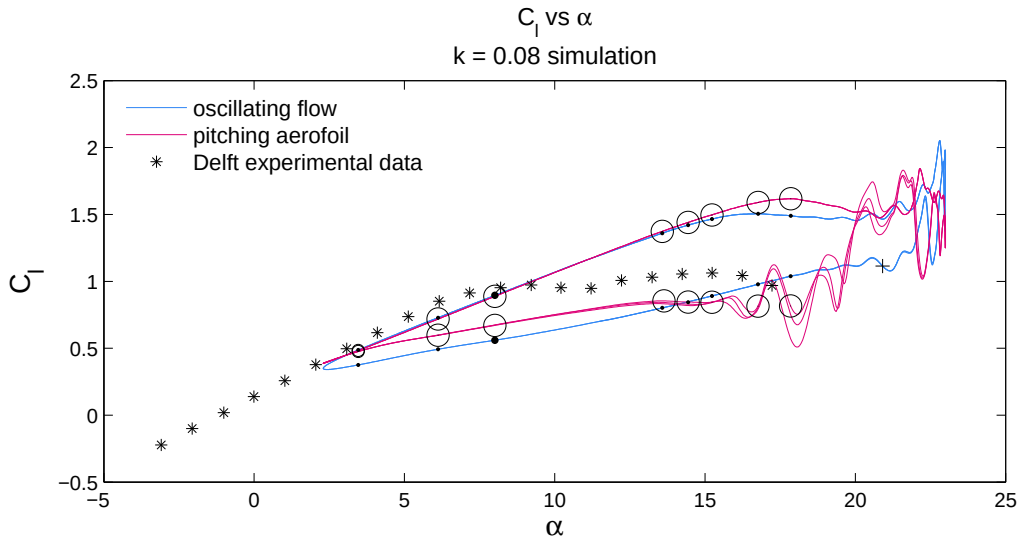

Fig. 3.12 Graphical positions of C_p measurements for $\pm 10°$, $\alpha_{\text{mean}} = 14°$, $k = 0.08$. ◯ for pitch oscillations and • flow oscillations

The $\alpha_{\text{max}} = 16.7°$ and $\alpha_{\text{max}} = 17.9°$ locations correspond to the angle of $C_{L\text{max}}$ for the OF curve then the PA curve respectively: on the downstroke these 2 locations correspond to the 'hysteresis lift' $C_{L\text{hys}}$ - as described in 3.3.1 and Ramsay et al. [9, p.13].

By an integration, the time delay taken for the aerofoil to 'see' the velocity input at the inlet, Δt, was found, and for post-processing, data were corrected for this phase-shift. For example, while figure 3.13 shows the velocity vector at 6.11°, at this time the velocity vector at the inlet is now at 22.95°. To measure the orientation of the vectors by looking at velocity

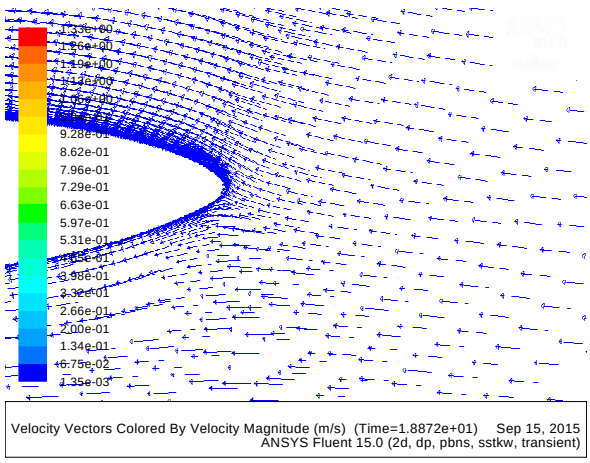

Fig. 3.13 Velocity vectors for 6.11° for $\pm 10°$, $\alpha_{\text{mean}} = 14°$, $k = 0.08$.

vector plots alone is misleading, as the flow gets pushed, pulled and directed around the LE of the aerofoil. Plots of pathlines were also studied. Also, to check the phase correction,

contour and vector plots were studied to find the maximum and minimum alpha - like turning points - and check that timesteps at the maximum and minimum α were as calculated.

Surface pressure coefficient - C_p - distributions around the aerofoil, as the AoA changes from 2.3° to 23° and back again, are shown in figure 3.15, for up the way, and figure 3.16, for down the way. The sketch in figure 3.14 shows the shape and a few features of the C_p plot.

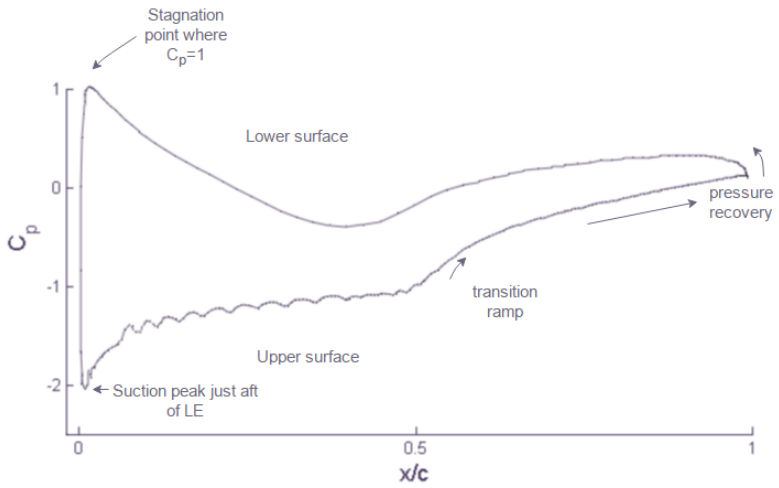

Fig. 3.14 Sketch of features of C_p plot.

The C_p plot for the straightforward PA case at some α (pitch angle), and the corresponding C_p plot for OF at the same α (flow angle), are plotted together for corresponding marked values α in 3.12 along both the increasing and decreasing α branches of the hysteresis loop.

Oscillating flow and Pitching aerofoil comparison

The plots for 'oscillating flow' appear translated upwards in the higher α plots compared to 'pitching aerofoil' (on the upstroke). This suggests there is an overall higher pressure distribution around the aerofoil for the oscillating flow (OF) case.

The higher C_p overall for the OF simulation, at the higher α, corresponds to a lower C_{Lmax} than for the PA simulation. There is likely to be increased re-entrainment of the fluid around the aerofoil for the OF case. This can be investigated by observing the near-wall velocity profile. Pressure changes are determined by the shearing stress at the wall and this, in turn, is determined by the velocity profile at the wall.

The reverse occurs on the downstroke, with 'pitching aerofoil' appearing translated upwards in the higher α plots. This is reinforced by looking at the lift and drag curves for 3.3.1 in 3.3.1 where values of the lift and drag coefficients tend to be significantly lower for OF than corresponding values for PA during the downstroke. It was referred to in 3.3.3,

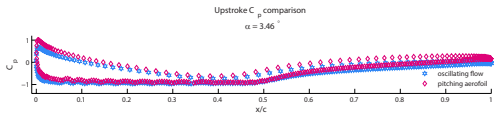

(a) C_p vs x/c at 3.4°

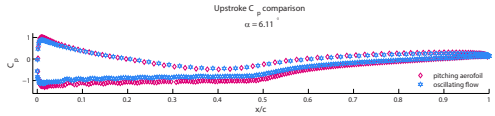

(b) C_p vs x/c at 6.0°

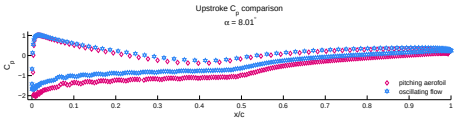

(c) C_p vs x/c at 8.0°

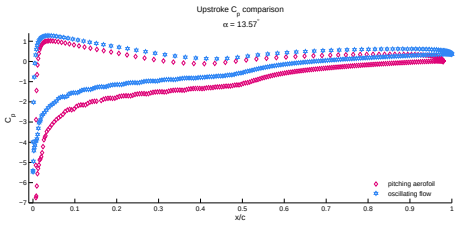

(d) C_p vs x/c at 13.5°

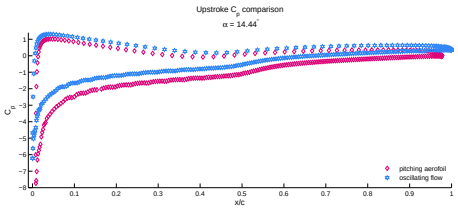

(e) C_p vs x/c at 14.3°

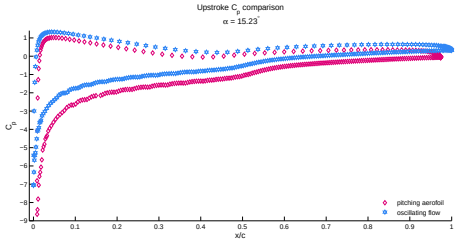

(f) C_p vs x/c at 15.1°

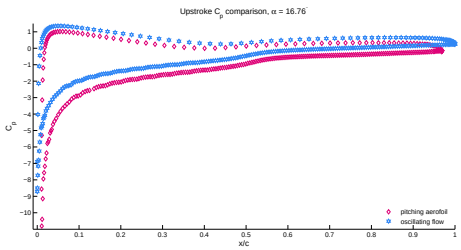

(g) C_p vs x/c at 16.7°

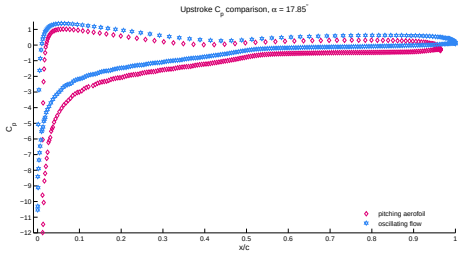

(h) C_p vs x/c at 17.9°

Fig. 3.15 C_p plots for both oscillating flow and pitching aerofoil at equivalent points on the upstroke

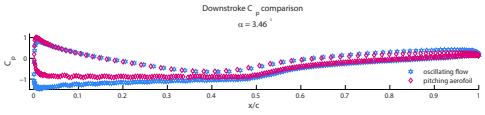

(a) C_p vs x/c at 3.4°

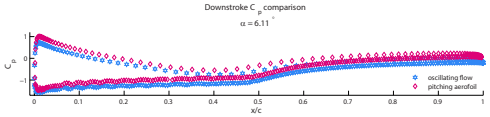

(b) C_p vs x/c at 6.0°

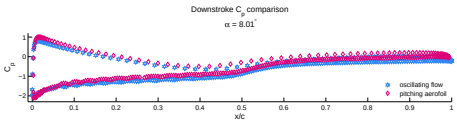

(c) C_p vs x/c at 8.0°

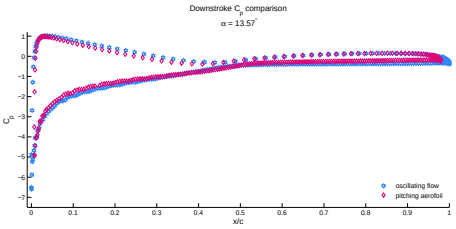

(d) C_p vs x/c at 13.5°

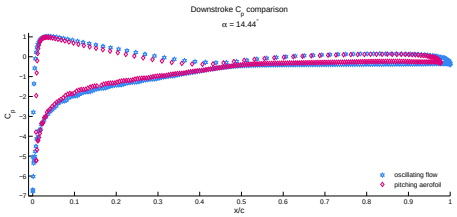

(e) C_p vs x/c at 14.3°

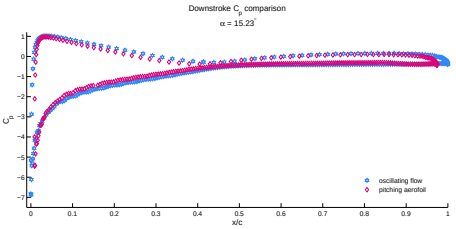

(f) C_p vs x/c at 15.1°

Fig. 3.16 C_p plots for both oscillating flow and pitching aerofoil at equivalent points on the downstroke

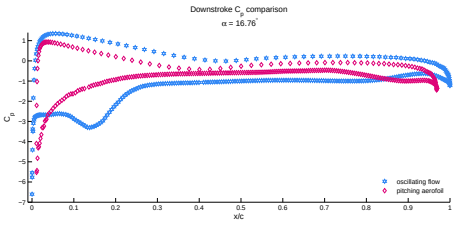

(a) C_p vs x/c at 16.7°

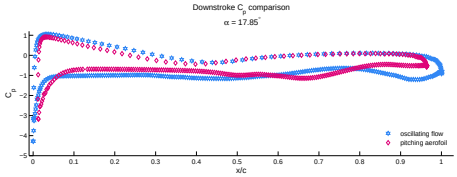

(b) C_p vs x/c at 17.9°

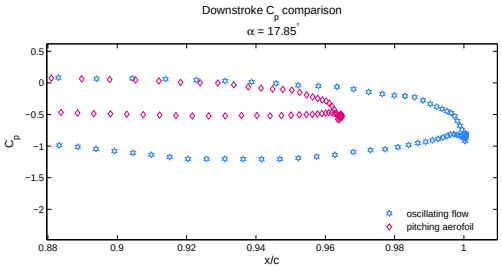

(c) close-up of TE. C_p vs x/c at 17.9°

Fig. 3.17 C_p plots for both oscillating flow and pitching aerofoil at equivalent points on the downstroke, high α

the fact that the curve for the drag coefficient for oscillating flow, in all cases, crosses the x-axis at y=0 during the downstroke.

A shortish region of adverse pressure gradient or pressure recovery - a “transition ramp” - is seen most clearly for the range $3.4° < \alpha < 8.0°$, which is said by Somers to be desirable for transition from laminar to turbulent flow. This begins from a region of nearly constant pressure (of $C_p = -1$) on the upper surface (lower side of plot [1]) near 0.5c (called the “pressure plateau" region in the literature) which is likely to predicate an LSB. This same feature is also present on the lower side just forward of 0.5c, also indicating an LSB. Russell [8], based on the original ideas by Horton [50], developed the theoretical model behind the schematic (1.2) shown in Chapter 1.

This LSB is some way aft of the LE, compared to being very near the LE for a LE-stalling aerofoil. It is also very minimal, probably because an LSB is associated more with low *Re* aerofoils, and the S809 has a relatively high design *Re* of 2×10^6. The pressure recovers over the rest of the upper surface.

[1] It is actually more usual to see the C_p plot reflected in the x-axis so that $-C_p$ is what is on the y-axis, but this is not done here.

A negative pressure (suction) peak is reached rapidly on the upper surface at a location near to the LE, for angles in the range $13^\circ < \alpha^\circ < 18^\circ$, represented by both OF and PA plots. The initial pressure recovery area is seen as a fluctuating curve in both pitch and flow C_p (likely also to indicate an increase in drag and tendency to separate).

A favourable pressure gradient on the lower surface (upper side of plot) to about 0.4c is desirable to achieve low drag, as can also be seen. Near the LE, where C_p value attains 1, is where the stagnation point is located.

Separation takes place at about 0.5c, as was confirmed by studying velocity vector plots.

Aft of this region, the pressure recovers smoothly, and this region is similar throughout all the plots except during the downstroke.

In figure 3.16 it can be seen that there is significant variation for the upper surface during the downstroke going from $17.9^\circ \rightarrow 16.7^\circ$, signifying large-scale flow separation over almost the entire upper surface going back towards the TE. Both oscillating flow and pitching aerofoil show a spike in negative pressure on the upper side, right at the TE, indicating a vortex has been immediately shed.

Any indication of an LSB has vanished until α decreases again to about 8°.

In summary, surface pressure C_p distributions on the aerofoil lower surface do not change very much during the upstroke and downstroke, for neither OF nor PA simulations. C_p distributions on the aerofoil upper surface on the other hand, vary significantly - constrasting PA at $16.7^\circ \uparrow\downarrow$, for example. This is consistent with the findings of other researchers [7].

Comparison with experiment

Figures 3.18 and 3.19 show C_p distributions around the aerofoil, for PA, OF and closely corresponding pitching experimental C_p results from Ramsay et al. [9]. These data were publicly available in the same location as the unsteady lift and drag data, publicly available from the NREL NWTC Information Portal.

Figures 3.18a and 3.18c for 3.4°, and 3.18b and 3.18d for 6.1°, show that the simulation C_p distributions agree well with experiment except just aft of midchord where spikes in the experimental distributions are seen. These are regions of the laminar separation bubbles.

For $6.1^\circ \uparrow$ these spikes better resemble an LSB, as pictured in 1.2.1, figure 1.2, on both the upper and lower surfaces (and on the lower surface for $6.1^\circ \downarrow$). Turbulent reattachment occurs at about 0.6c.

This feature of the unsteady C_p comparisons, where a negative pressure spike is seen, is consistent with the steady-state CFD pressure distribution-compared-with-experiment for low α as shown in the S809 study by Wolfe and Ochs [51, pp. 16–17].

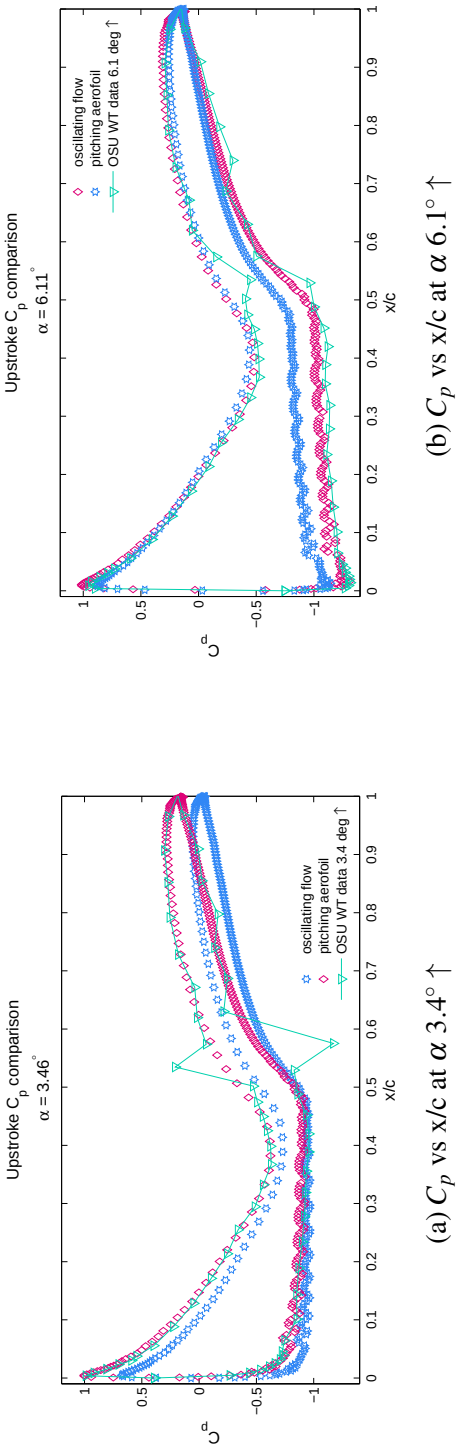

(a) C_p vs x/c at α 3.4° ↑

(b) C_p vs x/c at α 6.1° ↑

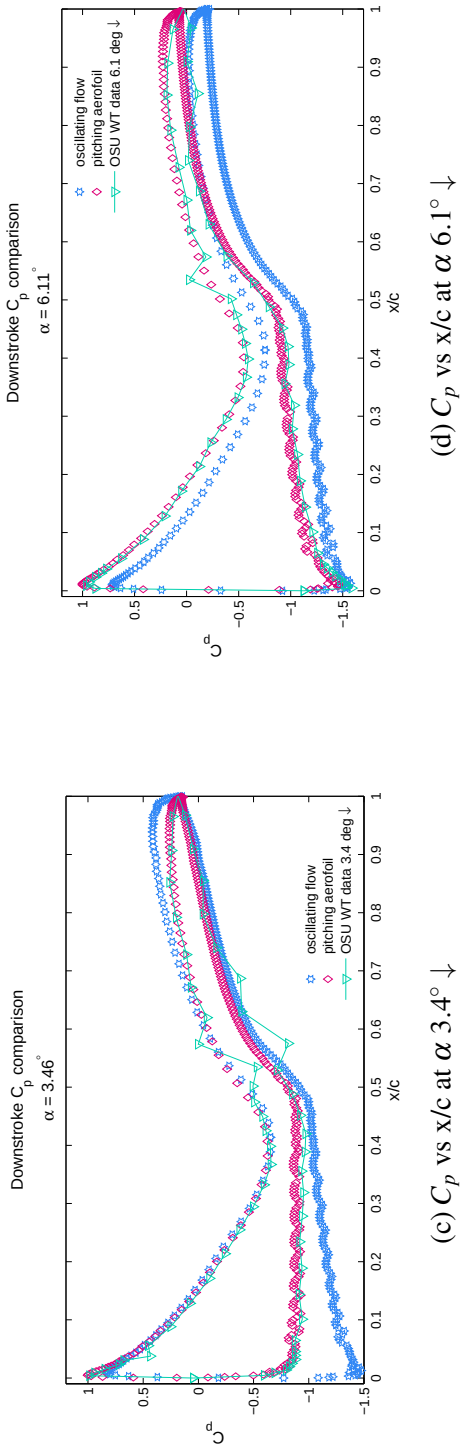

(c) C_p vs x/c at α 3.4° ↓

(d) C_p vs x/c at α 6.1° ↓

Fig. 3.18 C_p vs x/c for $\alpha = 3.46°$ and $\alpha = 6.11°$, comparison with experiment (α_0=14°, α_1=±10°, $k = 0.08$).

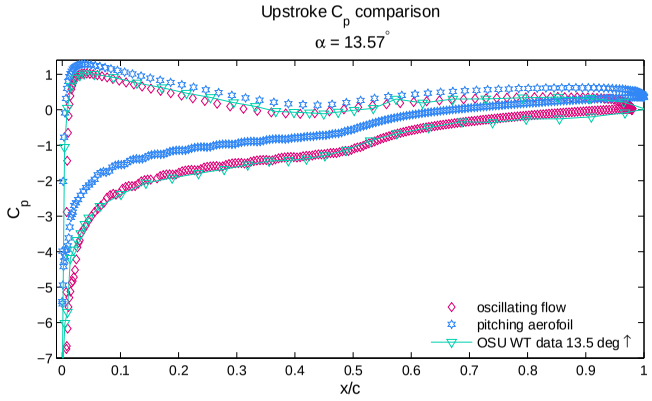

(a) C_p vs x/c at α 13° ↑

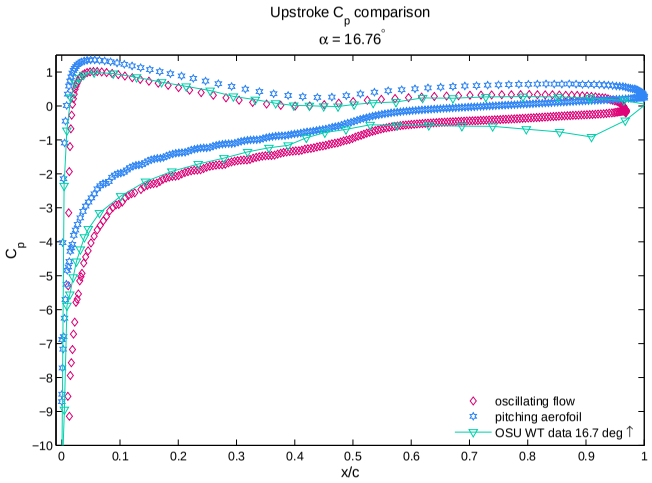

(b) C_p vs x/c at α 16.7° ↑

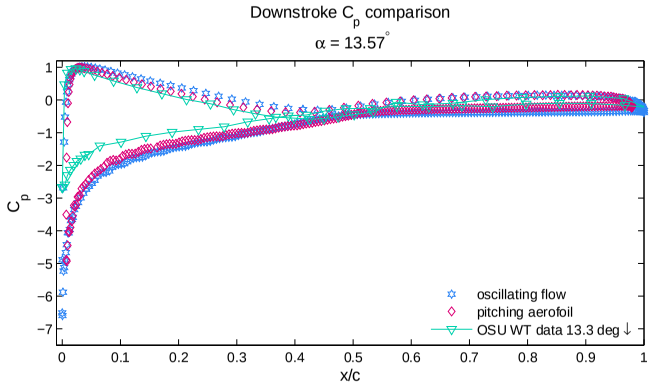

(c) C_p vs x/c at α 13° ↓

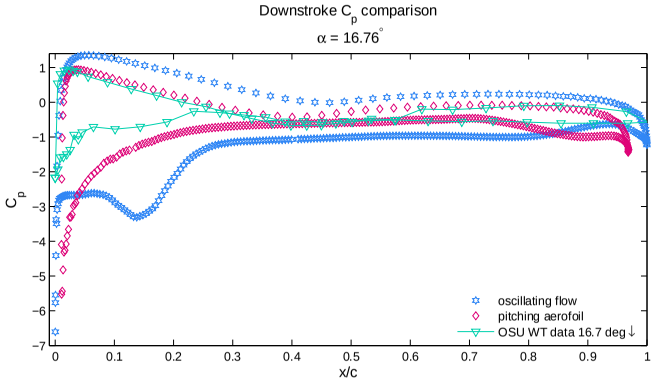

(d) C_p vs x/c at α 16.7° ↓

Fig. 3.19 C_p vs x/c for $\alpha = 13.57°$ and $\alpha = 16.76°$, comparison with experiment (α_0=14°, α_1=±10°, $k = 0.08$).

Figures 3.19a and 3.19c for 13.5° show good agreement. The LSB has gone meaning the flow is fully turbulent. Figure 3.19b for 16.7° ↑ shows good agreement all the way around except on the upper side at the TE and figure 3.19d for 16.7° ↓ again shows good agreement all the way around except towards the LE on the upper side. The shallower dip in pressure on the suction side, after 0.1c and the much more sudden suction spike close to the LE, is closer to 'oscillating flow' at this stage. These features are consistent with the differences seen between the CFD prediction and experiment for larger α in Wolfe and Ochs [51, pp. 22–23].

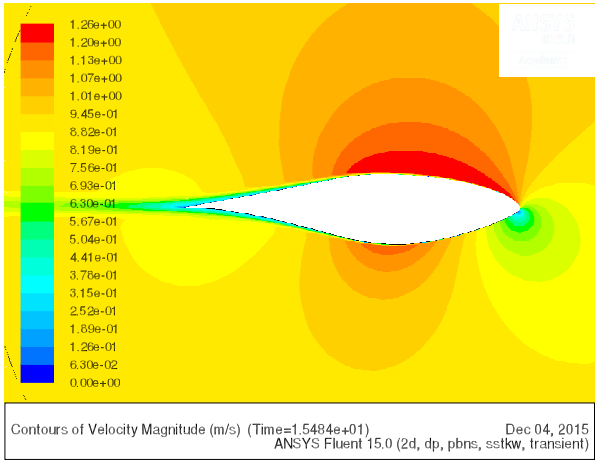

(a) Oscillating flow: α 3.4° ↑

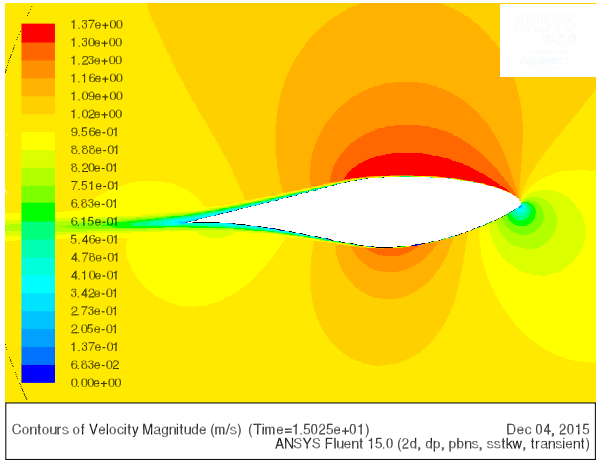

(b) Pitching aerofoil: α 3.4° ↑

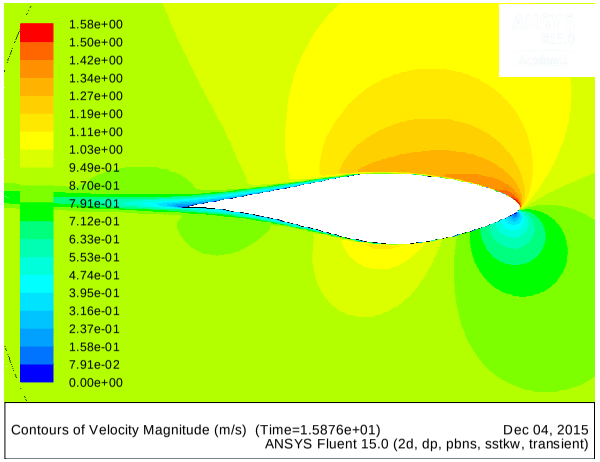

(c) Oscillating flow: α 8.0° ↑

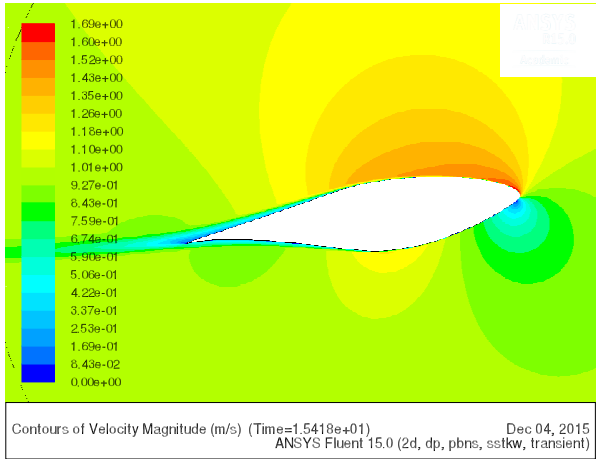

(d) Pitching aerofoil: α 8.0° ↑

Fig. 3.20 Velocity Magnitude contours for $\alpha = 3.4°$ and $\alpha = 8.0°$, comparison between oscillating flow (left) and pitching aerofoil (right) (α_0=14°, α_1=±10°, $k = 0.08$).

3.3.5 Pressure and Velocity Magnitude contour plots

Velocity magnitude contour plots at equivalent positions and times, on the 'upstroke' and 'downstroke', for the pitching aerofoil and oscillating flow simulations, are shown in figures 3.20 and 3.21 (upstroke) and 3.22 (downstroke).

The oscillating flow simulation was found to be very different from the pitching aerofoil during the downstroke, at the *higher* angles of attack, though similarities in the flow field can be seen between figures 3.23a and 3.23b for points on the downstroke that do not seemingly correspond exactly in timing. This can be seen from 3.12, where the velocity contour plot in figure 3.23a corresponds to the '+' at about 21° for the OF simulation (blue), where there is a sudden increase in lift, and where 3.23b corresponds to the $C_{L\text{hys}} = 17.9°$ location. Furthermore, this implies a phase shift, in the shedding of a secondary vortex (indicated by the aforesaid increase in C_l), between the PA and OF simulations. The pitching normal force curve is shifted to the right, or rather, is delayed in the phase of the dynamic stall.

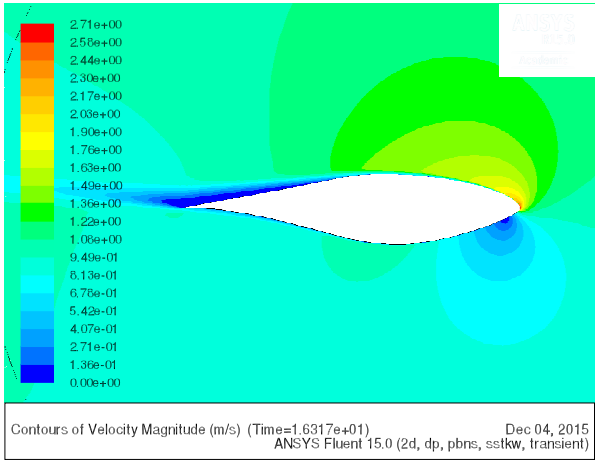

(a) Oscillating flow: α 15.1° ↑

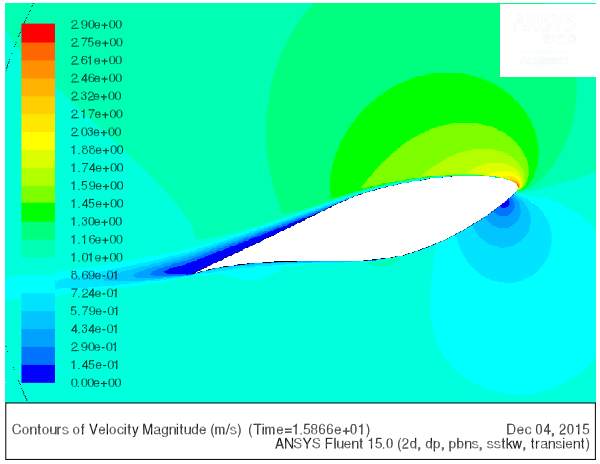

(b) Pitching aerofoil: α 15.1° ↑

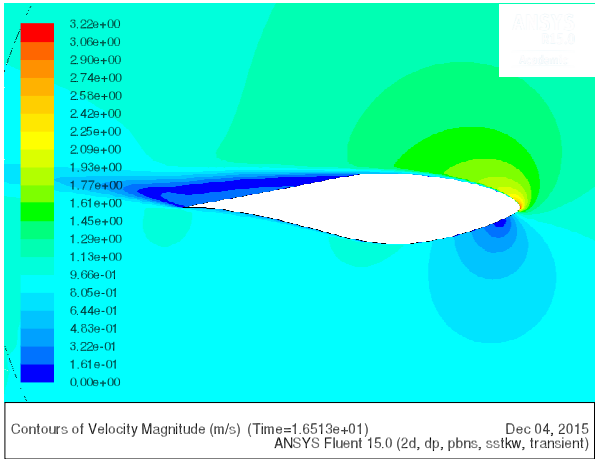

(c) Oscillating flow: α 18.0° ↑

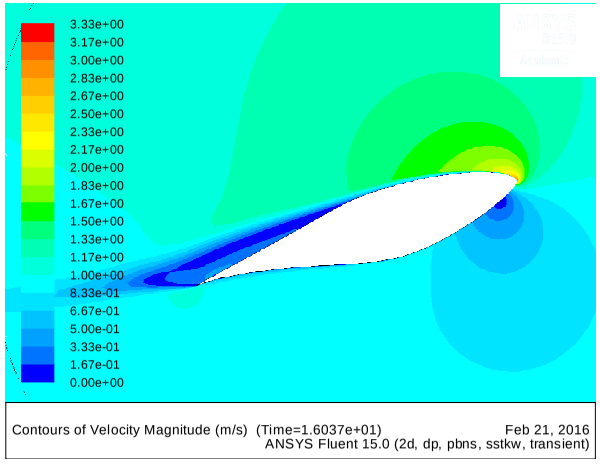

(d) Pitching aerofoil: α 18.0° ↑

Fig. 3.21 Velocity Magnitude contours for α 15.1° and α 18.0, comparison between oscillating flow (left) and pitching aerofoil (right) (α_0=14°, α_1=±10°, $k = 0.08$).

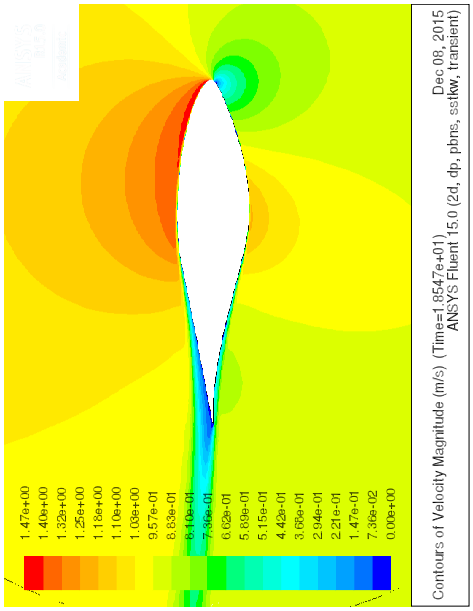

(a) Oscillating flow: α 6.11° ↓

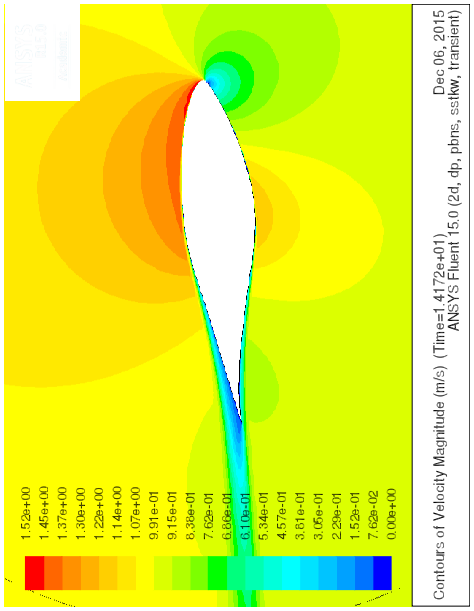

(b) Pitching aerofoil: α 6.11° ↓

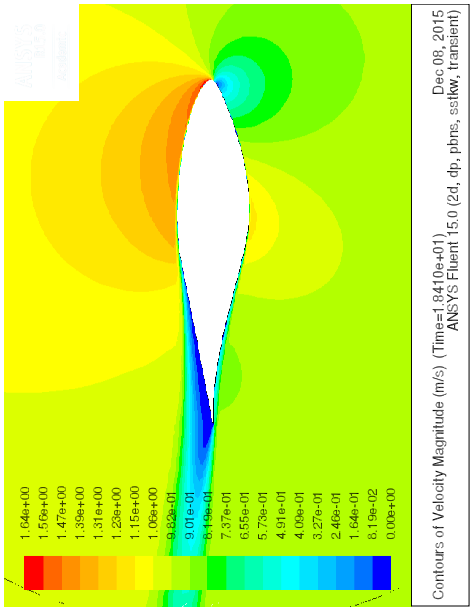

(c) Oscillating flow: α 8.01° ↓

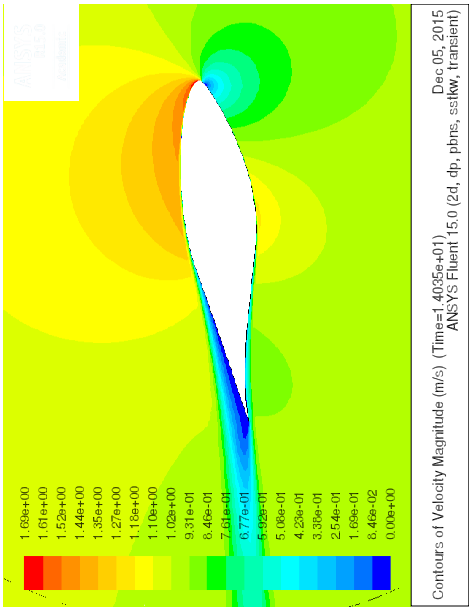

(d) Pitching aerofoil: α 8.01° ↓

Fig. 3.22 Velocity contour plots for oscillating flow (left), compared with pitching aerofoil (right)(α_0=14°, α_1=±10°, $k = 0.08$)

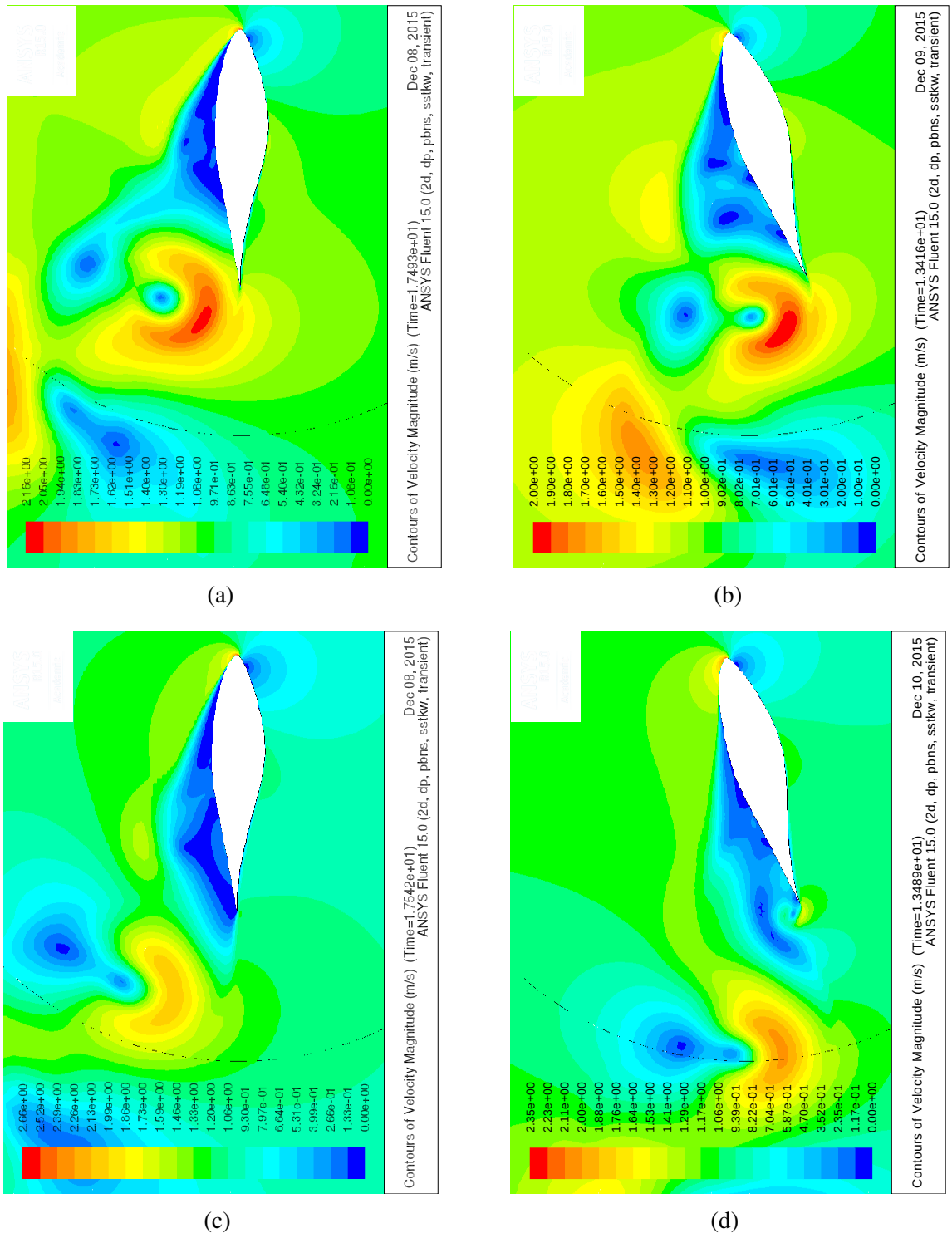

Fig. 3.23 Velocity contour plots for oscillating flow (left), compared with pitching aerofoil (right), corresponding to locations (a) '+' at about 21° in figure 3.12, (b) $C_{L\text{hys}} = 17.9°$: (c) and (d) correspond similarly.

3.3.6 Time evolution of pressure coefficient plots for 3.3.1

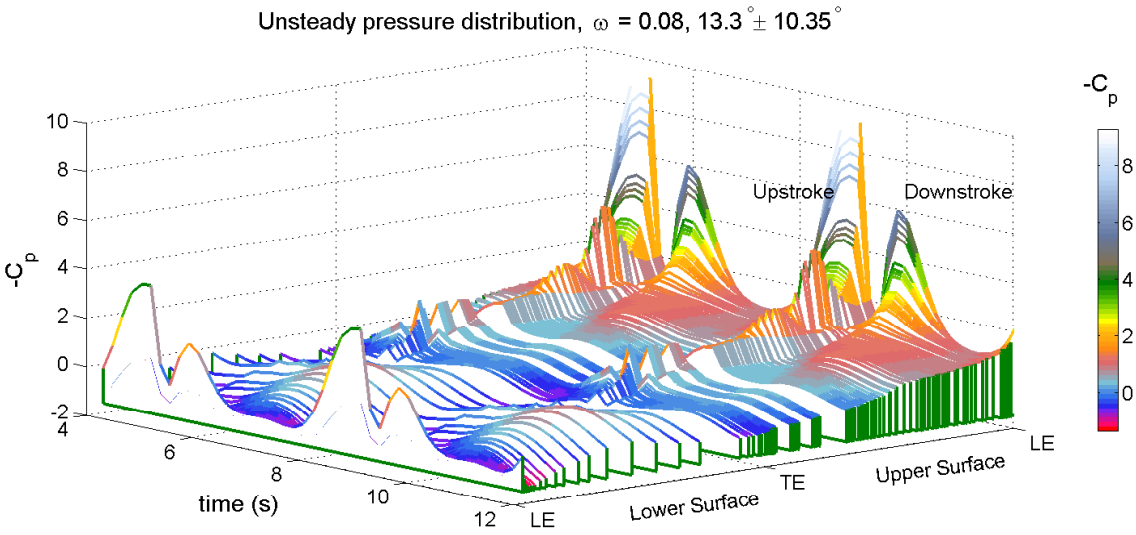

Fig. 3.24 Time evolution of C_p for oscillating flow ($\alpha_{\text{mean}} = 12.65$, $\alpha_1 = \pm 10°$, $k = 0.08$). Az:-87 El:90.

The C_p time evolution for oscillating flow, figure 3.24, shows the negative pressure peak on the suction upper surface, near the LE, towards the highest point of the upstroke.

For oscillating flow - figure 3.24 - vortex shedding takes place after 5s and 9s, which precedes a period of turbulence.

For the pitching aerofoil, there appears to be more turbulence after this event than for oscillating flow. This could be due to the fact that the pitching aerofoil is in the act of 'blocking' the flow. The decrease in fluid velocity is accompanied by an increase in turbulent flow.

There is one distinct low pressure spike at the TE in figure 3.24 between, e.g., 9.5s and 10s, which may indicate a TE vortex. A section of the data for the OF simulation is shown in figure 3.25. The C_p data are colour-coded and projected onto the shape of the upper 'surface planform' of the aerofoil, with time as the 'z' coordinate. It was seen that there is a consistent periodicity to the data. This was observed for all simulations and so it was decided that these were fully time-converged solutions.

The higher pressure regions signal the formation, growth and convection of vortices on the upper surface of the aerofoil.

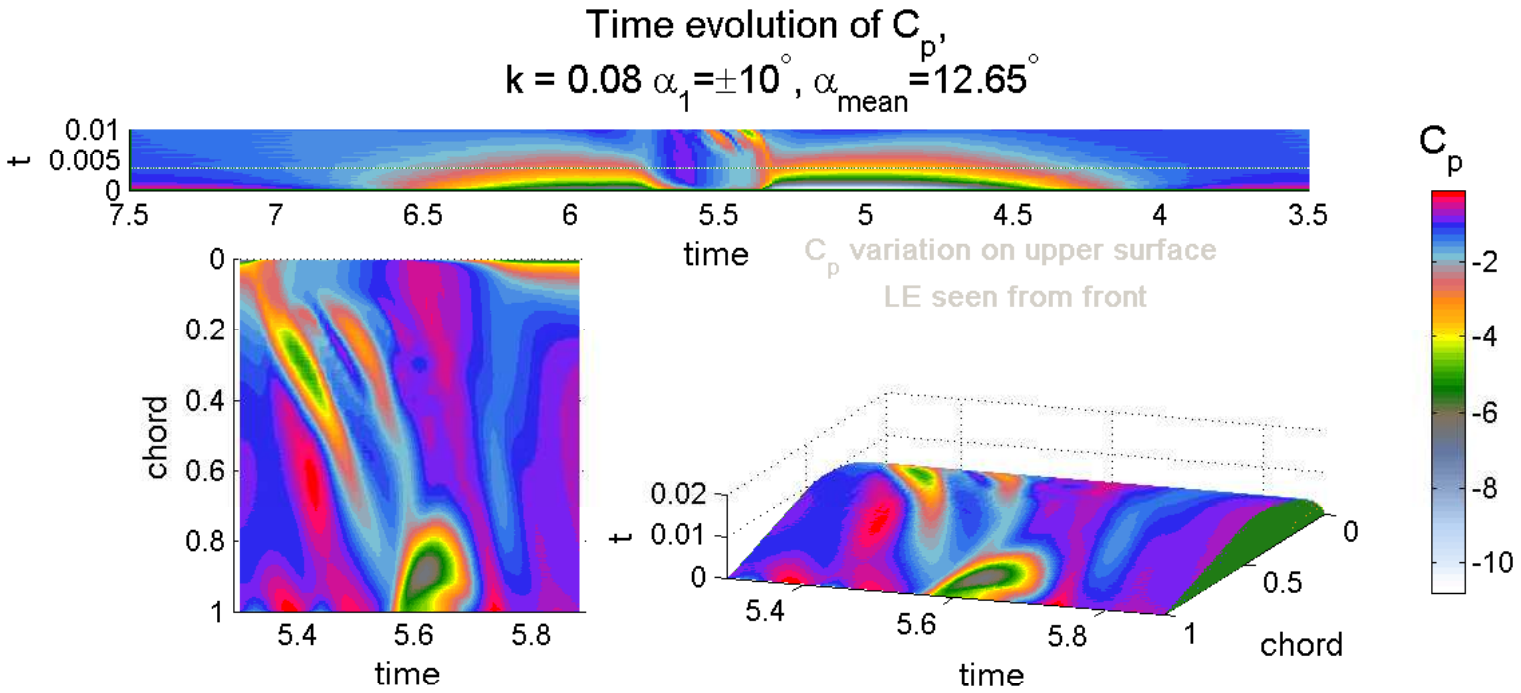

Fig. 3.25 Time evolution of C_p for oscillating flow carpet plot ($\alpha_{\text{mean}} = 12.65$, $\alpha_1 = \pm 10°$, $k = 0.08$)

Chapter 4

Simulations with ejection

4.1 Steady Simulations Results with Ejection

A separate zone was created in ICEM CFD from line elements of the existing mesh. This was labelled the injection and a pressure-inlet BC specified for this zone.

The initial/total guage pressure was varied in increments of 0.05 (Pa).

A Scheme batch script was written to cycle through the simulations. For every angle of attack the cycle started from a developed flow-field loaded from a Fluent solution-data file corresponding to that α. The simulation cycle was run in order of increasing pressure: each ejection run had a loaded flow-field from the previous (lower) ejection value to assist in convergence. Ejection locations are shown in figure 4.1.

The ejection plots are, for the MC (mid-chord) location; figures 4.2a, 4.2b, 4.3a, 4.3b, 4.5a and 4.5b. For the TE location, these are figures 4.6a, 4.6b, 4.7a, 4.7b, 4.9a and 4.9b.

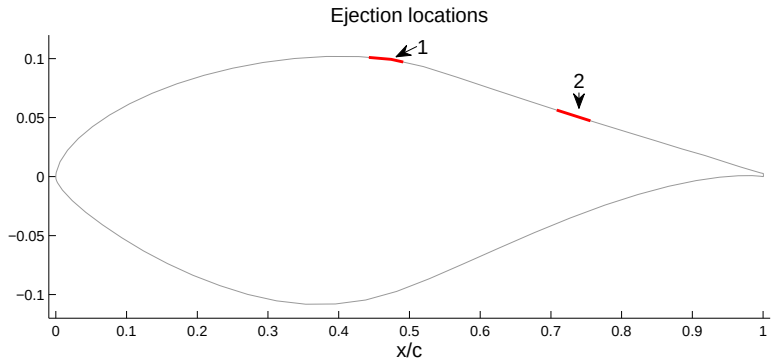

Fig. 4.1 Ejection locations

Johnson et al. [24] describe three ways that a reduced $\frac{\Delta L}{\Delta \alpha}$ help to reduce the load:

1. The lift variation ΔL for a given $\Delta \alpha$ is reduced

2. The maximum lift for a given α is lowered

3. Magnitude of the maximum negative lift is reduced (important for emergency shut down for certain machines)

To reduce an oscillating load, sudden changes in lift have to be mitigated and this can be done by reducing the lift curve slope, $\frac{\Delta L}{\Delta \alpha}$. This is also referred to as a *decambering* effect. At first glance it looks as though the following ejection tests achieve this as well as reducing the $C_{\mathrm{L}\max}$.

The drag increases with increasing pressure of the ejection, as would be expected. Correspondingly, the higher the pressure of the ejection, the less the lift.

The $\frac{\Delta L}{\Delta \alpha}$ slope is significantly lessened for location 1 mid-chord. This effect dies away with increasing angle away from the normal. It is not so evident for location 2.

Ejection location 1 - mid-chord

For ejection normal to the wall at the midchord location the lift (figure 4.2b) is reduced substantially by about half of the $C_{\mathrm{L}\max}$, meanwhile, the stall is quite significantly delayed. There is also creation of negative lift - which is obvious since the ejection here is constant at all α. The reactive force due to the ejection exceeds the lift.

The reduction of maximum lift is less for the ejection oriented at 60° (to the x-axis of the coordinate system) (figure 4.3b) compared to the normal ejection, and the overall impression of the curve is that it is translated upwards compared to the normal ejection. The ratio $\frac{\Delta L}{\Delta \alpha}$ is similar.

The ejection has a decambering effect upon the aerofoil lift characteristic and there may be a functional dependence to this decambering effect depending upon AoA. There is also some variation of the slope for individual pressures. The drag is similar throughout.

Figure 4.4 shows the TKE for (going down) $\alpha = 10°$ and 12°, for (left to right) no ejection, the highest, then the lowest pressure ejection. All the ejection cases exhibit a counter-rotating pair of vortices behind the ejection. This increases the drag more for location 1 than location 2.

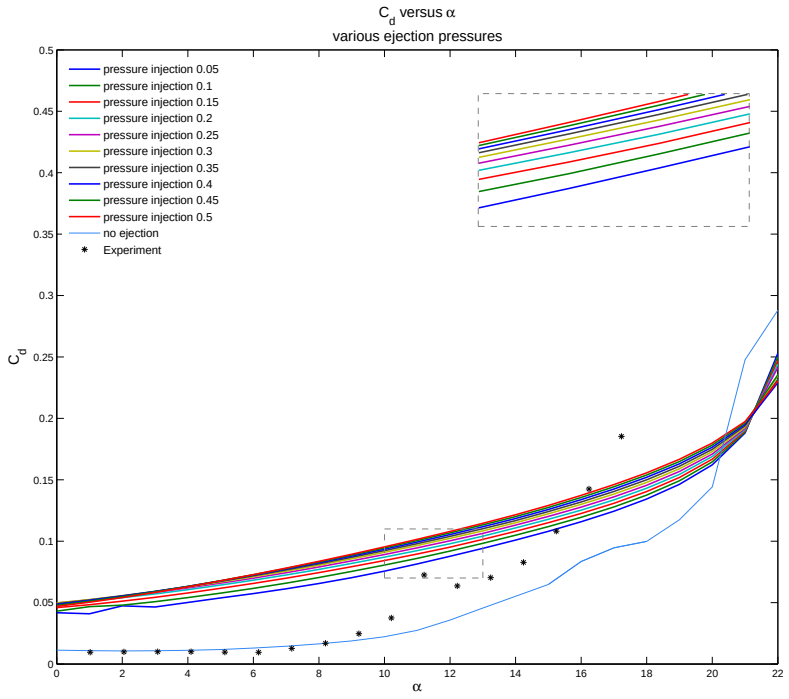

(a) C_{D} vs. α, ejections from 1, normal to surface, comparison with experiment

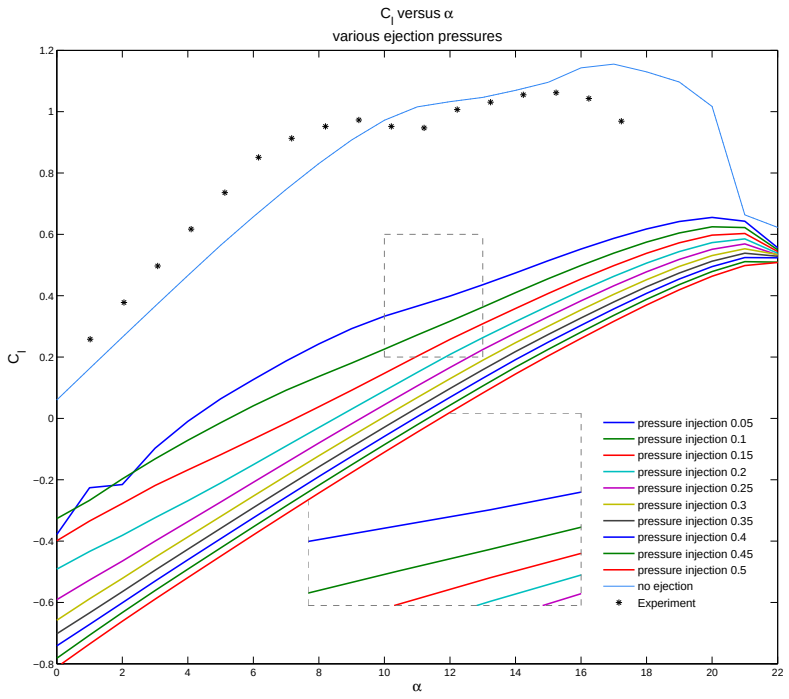

(b) C_{L} vs. α, ejections from 1 comparison with experiment

Fig. 4.2 lift and drag curves for ejections from location 1, normal to surface, compared with steady-state data

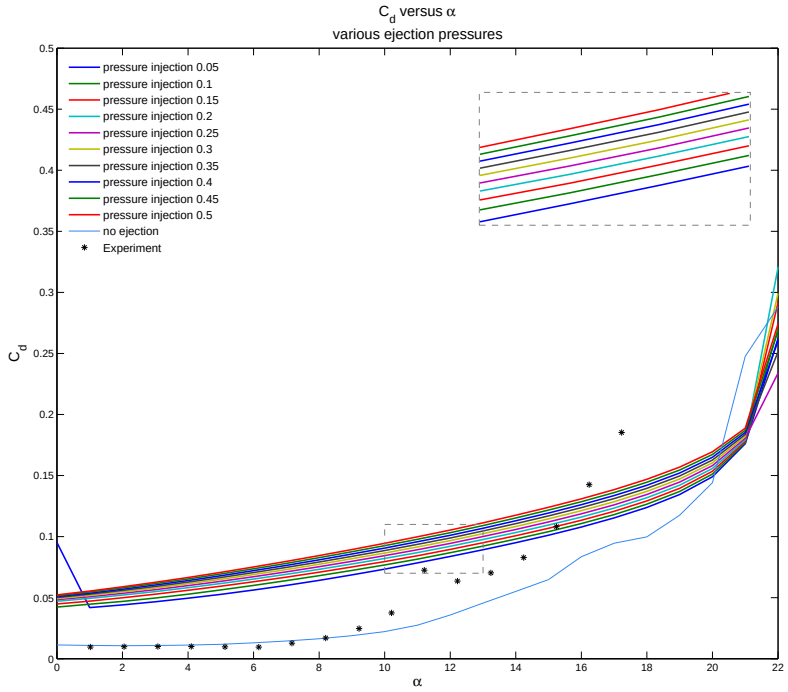

(a) C_{D} vs. α, ejections from 1, angled at 60°, comparison with experiment

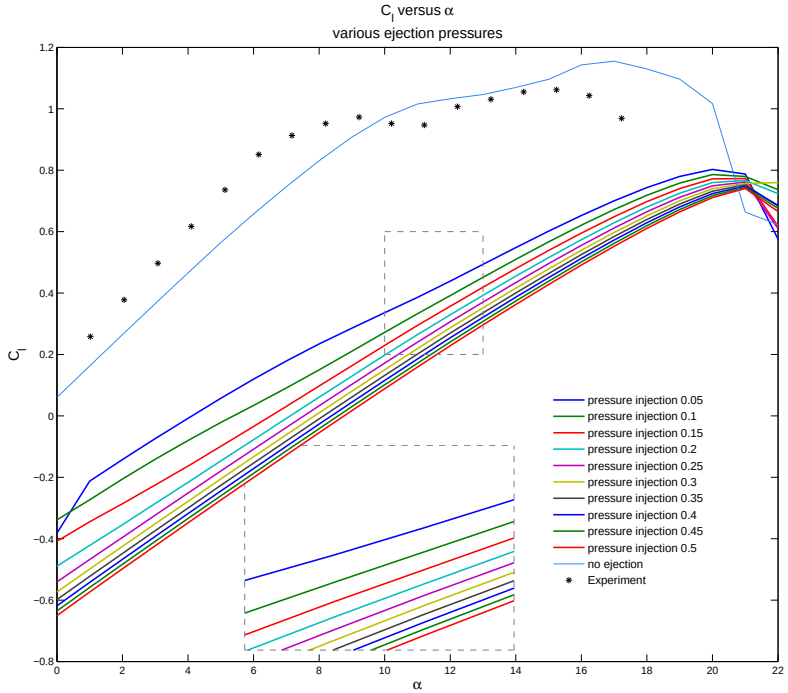

(b) C_{L} vs. α, ejections from 1, angled at 60°, comparison with experiment

Fig. 4.3 lift and drag curves for ejections from location 1, angled at 60° to the x-axis, compared with steady-state data

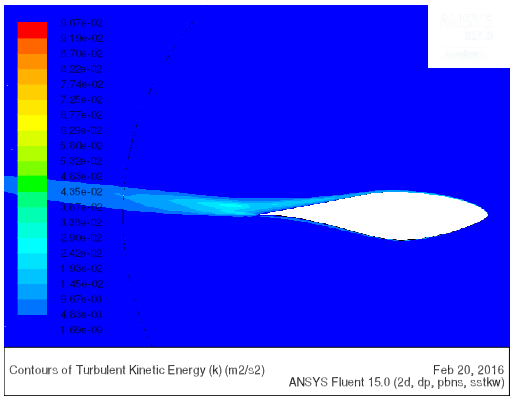

(a) TKE at $\alpha = 10°$, no ejection

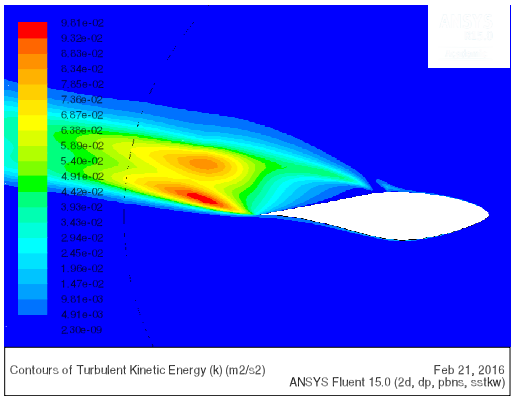

(b) TKE at $\alpha = 10°$, ejection pressure=0.5

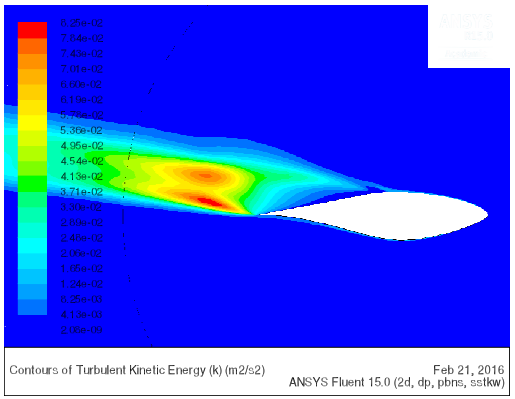

(c) TKE at $\alpha = 10°$, ejection pressure=0.05

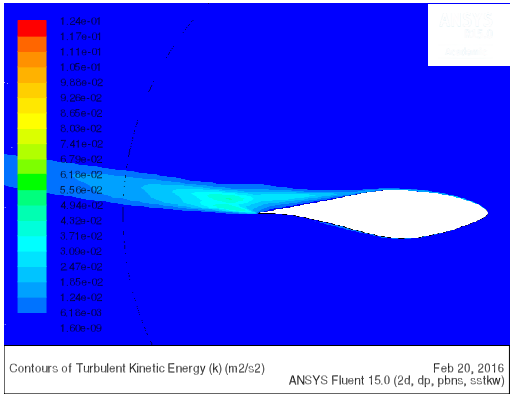

(d) TKE at $\alpha = 12°$, no ejection

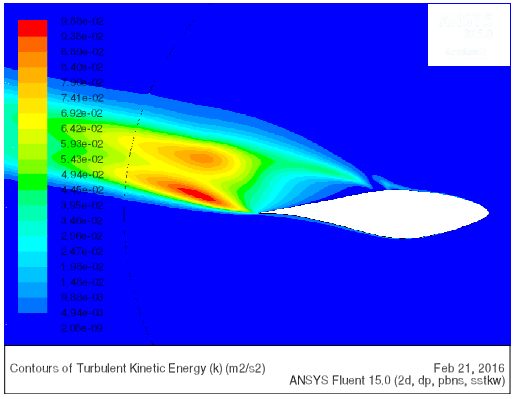

(e) TKE at $\alpha = 12°$, ejection pressure=0.5

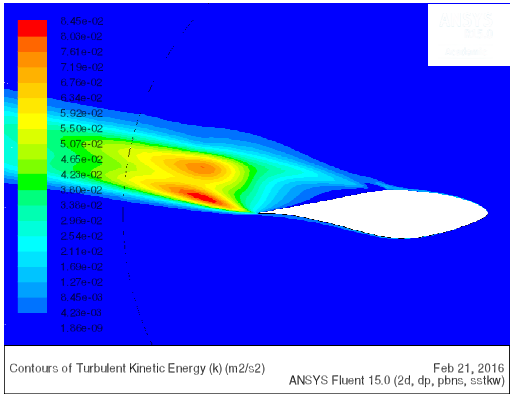

(f) TKE at $\alpha = 12°$, ejection pressure=0.05

Fig. 4.4 TKE contour plots for (a), (b), (c) $\alpha = 10°$ and (d), (e), (f) $\alpha = 12°$. Left to right: no ejection, ejection pressure=0.05 and 0.5, oriented 60° to the x-axis.

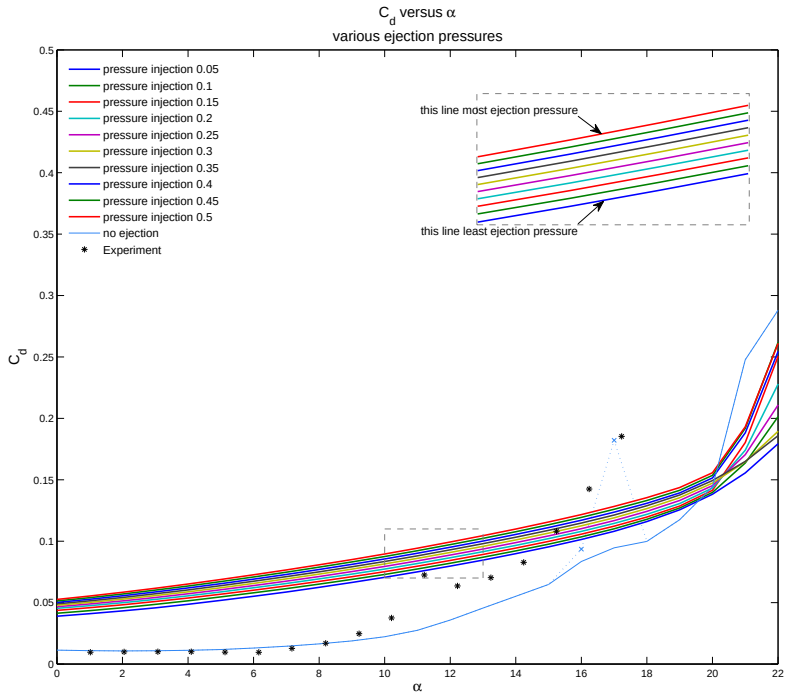

(a) C_{D} vs. α, ejections from 1, angled at 45°, comparison with experiment

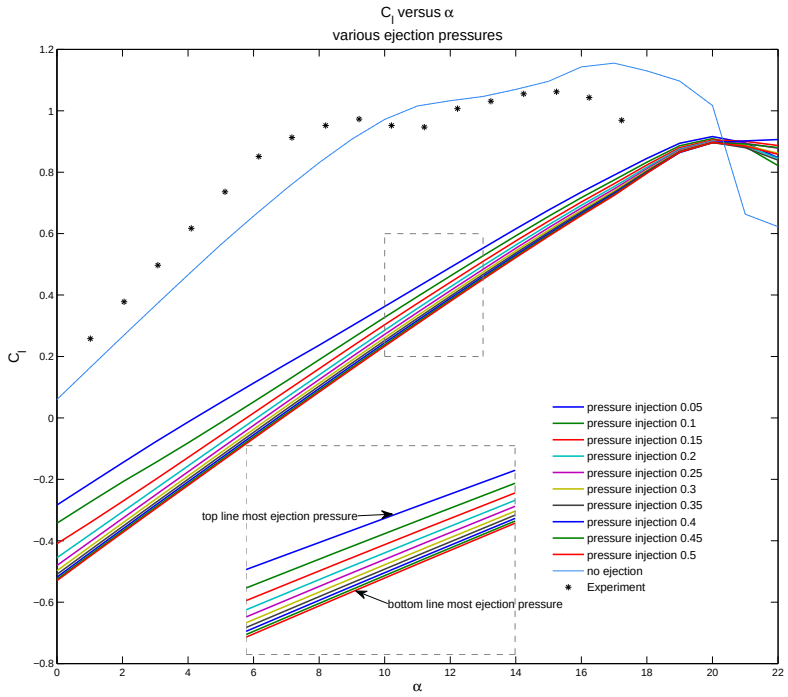

(b) C_{L} vs. α, ejections from 1, angled at 45°, comparison with experiment

Fig. 4.5 lift and drag curves for ejections from location 1, angled at 45° to the x-axis, compared with steady-state data

Ejection location 2 - TE

There is little variance in the effect of the individual pressures on the drag for the TE ejection. This is perhaps because there is sufficient mixing in the BL at the TE. For the lift there is the same decambering effect as previously for location 1.

The normal lift for location 2 (figure 4.6b) is not as reduced as for location 1 (figure 4.2b) and the slope is not as affected. There is production of negative lift but this lessens with increasing angle away from the normal until for 45° (figure 4.9b) there is a little negative lift but C_{Lmax} is the same value as for without the pressure ejection.

Figure 4.8shows the TKE for (going down) $\alpha = 10°$,6° and 12°, for (left to right) no ejection, the highest, then the lowest pressure ejection. There are again 2 counter-rotating vortices, but these are smaller compared to those in 4.4.

Figure 4.10 shows comparisons of the different locations of the ejection, and the different angles of orientation to the flow in plots where the pressure is held constant. There is more spread of the lines of the charts for the higher pressure (=0.5 Pa). This would indicate that, as is to be expected, the highest of the pressures will reveal most about the effect of an unsteady blowing device.

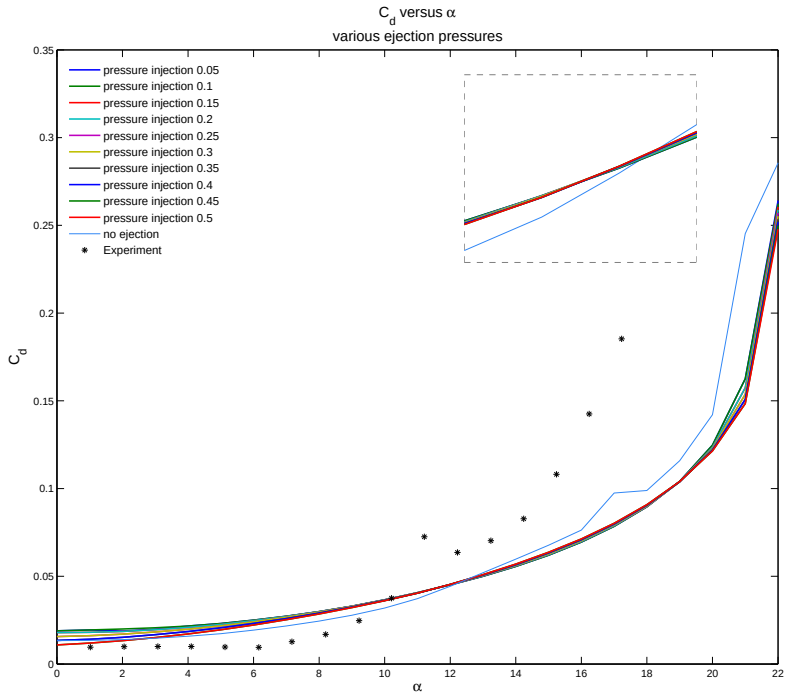

(a) C_{D} vs. α, ejections from 2, normal to surface, comparison with experiment

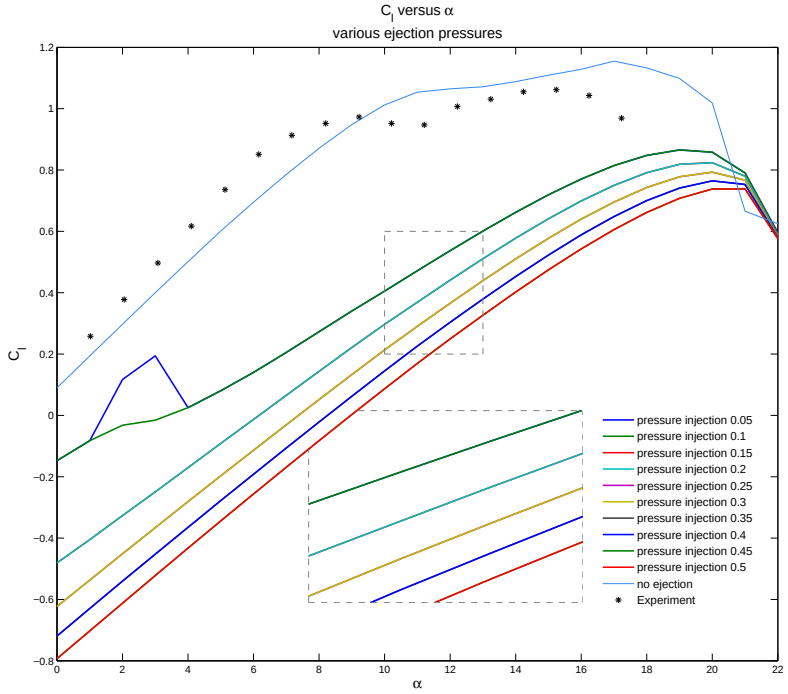

(b) C_{L} vs. α, ejections from 2, normal to surface, comparison with experiment

Fig. 4.6 lift and drag curves for ejections from location 2, normal to surface, compared with steady-state data

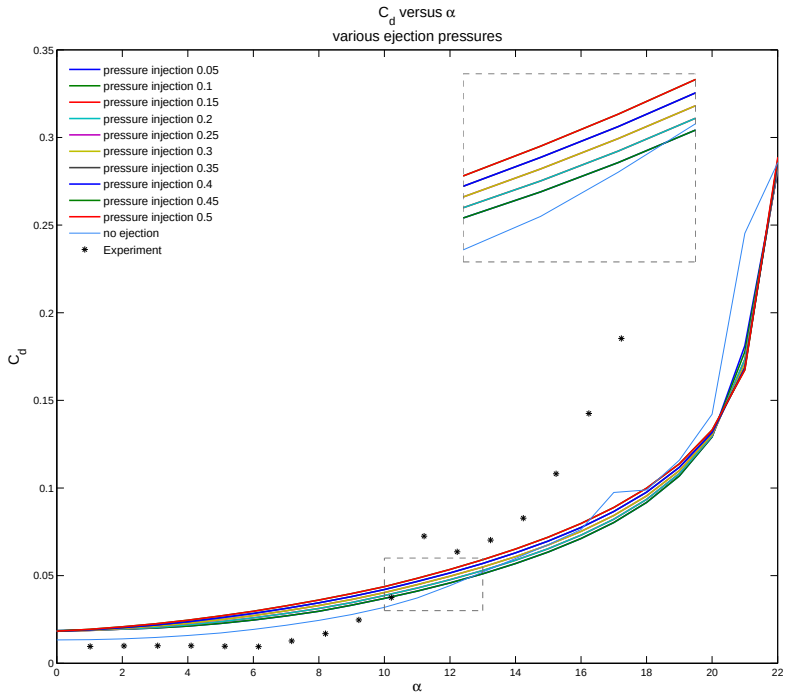

(a) C_D vs. α, ejections from 2, angled at 60°, comparison with experiment

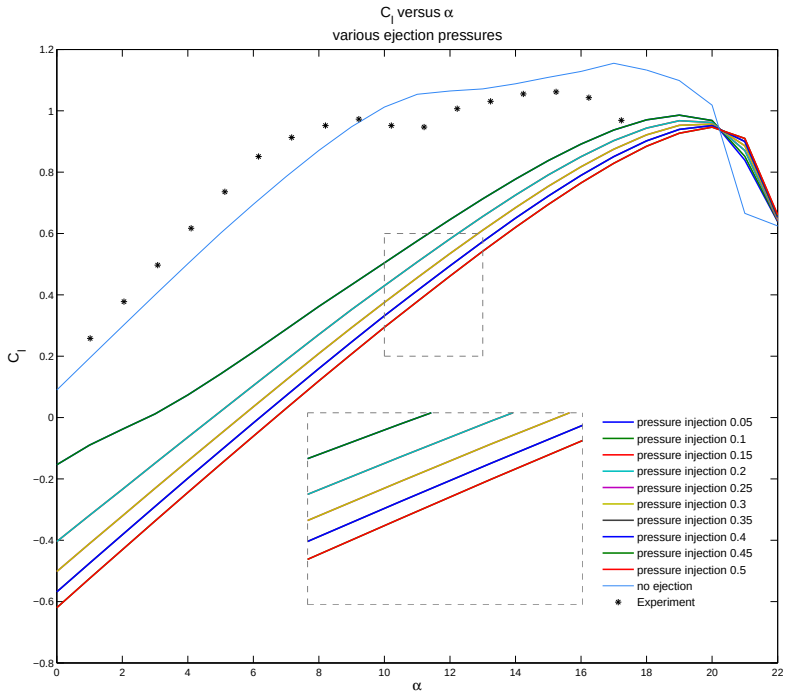

(b) C_L vs. α, ejections from 2, angled at 60°, comparison with experiment

Fig. 4.7 lift and drag curves for ejections from location 2, angled at 60° to the x-axis, compared with steady-state data

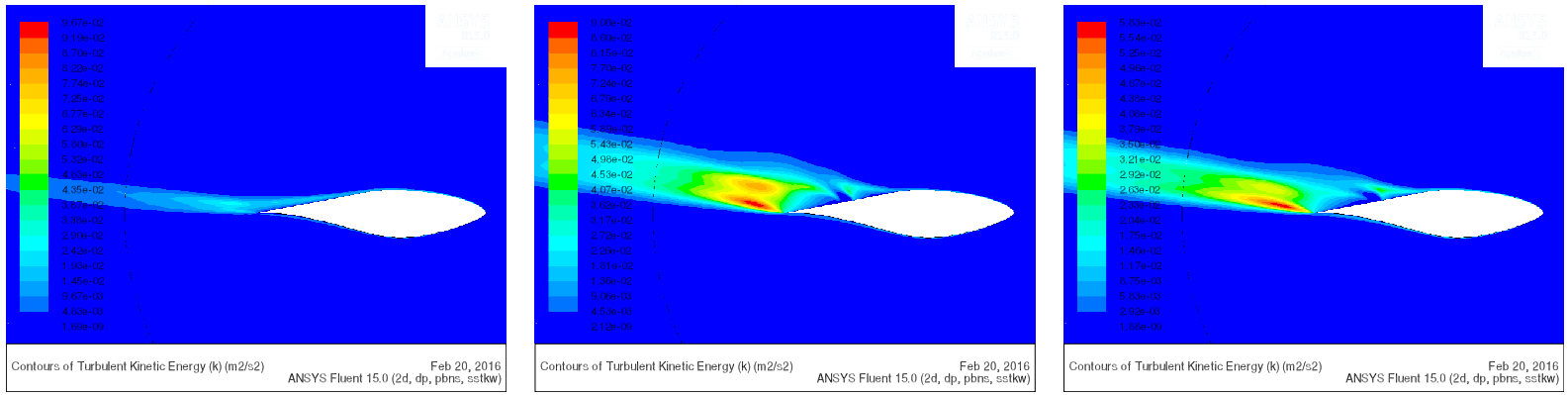

(a) TKE at $\alpha = 10°$, no ejection (b) TKE at $\alpha = 10°$, ejection pressure=0.5 (c) TKE at $\alpha = 10°$, ejection pressure=0.05

(d) TKE at $\alpha = 12°$, no ejection (e) TKE at $\alpha = 12°$, ejection pressure=0.5 (f) TKE at $\alpha = 12°$, ejection pressure=0.05

Fig. 4.8 TKE contour plots for (a), (b), (c) $\alpha = 10°$ and (d), (e), (f) $\alpha = 12°$. Left to right: no ejection, ejection pressure=0.05 and 0.5, from location 2, oriented at 60° to the x-axis.

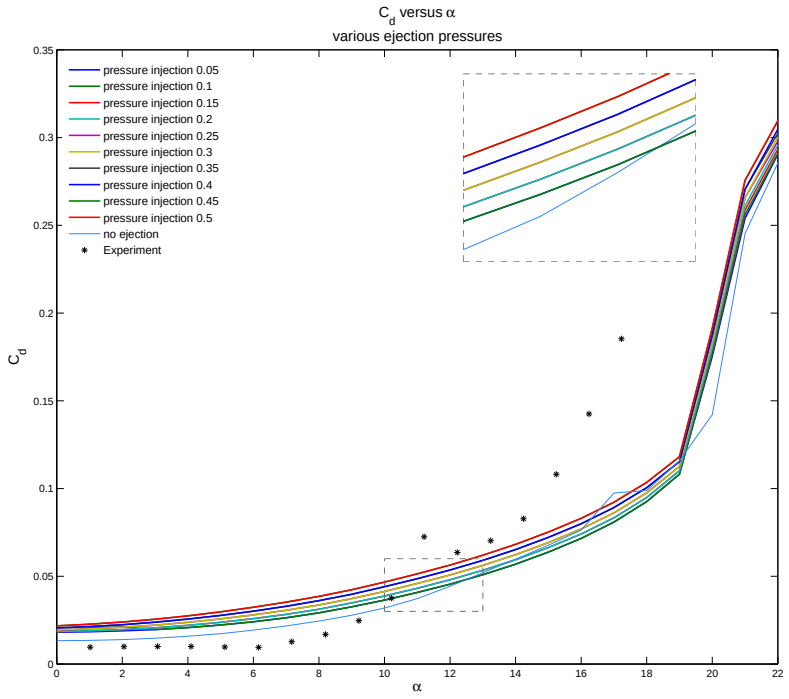

(a) C_D vs. α, ejections from 2, angled at 45°, comparison with experiment

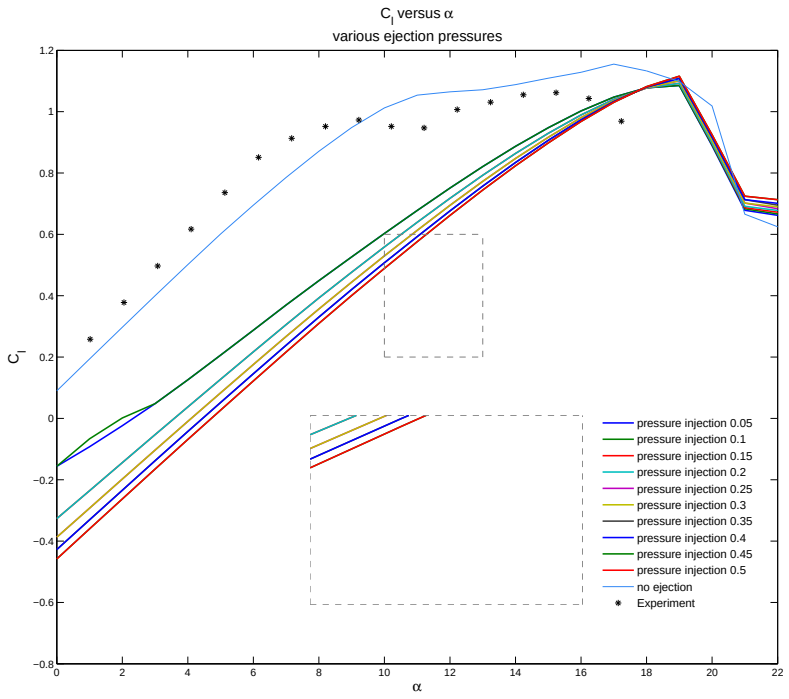

(b) C_L vs. α, ejections from 2, angled at 45°, comparison with experiment

Fig. 4.9 lift and drag curves for ejections from location 2, angled at 45° to the x-axis, compared with steady-state data.

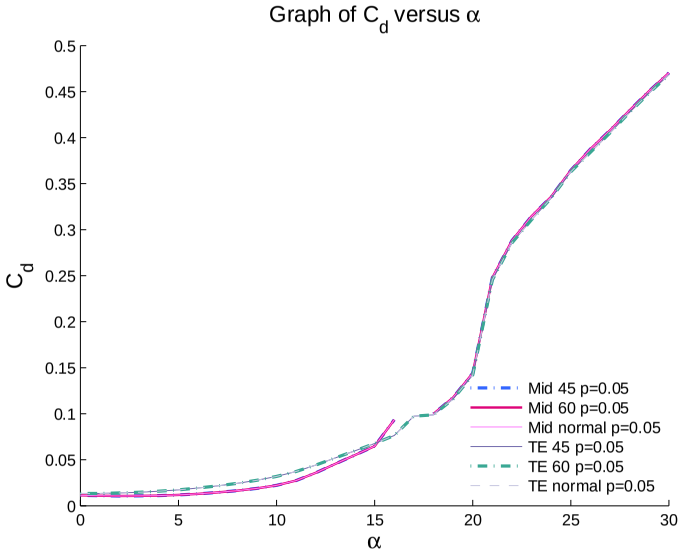

(a) C_D vs. α, ejections with guage pressure of 0.05

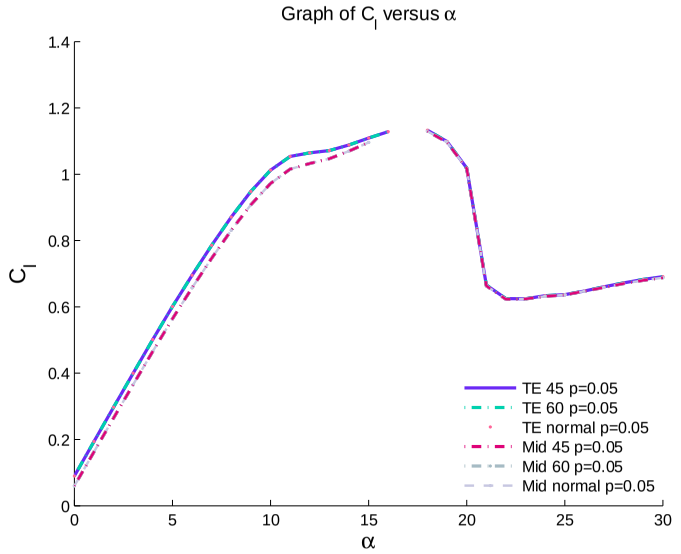

(b) C_L vs. α, ejections with guage pressure of 0.05

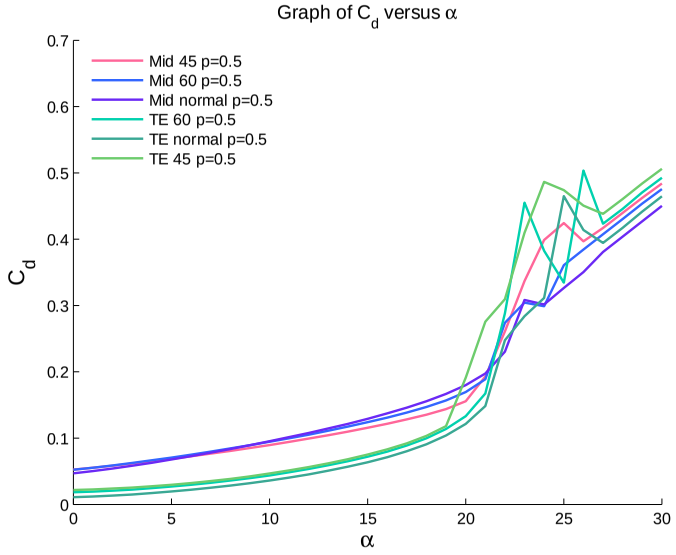

(c) C_D vs. α, ejections with guage pressure of 0.5

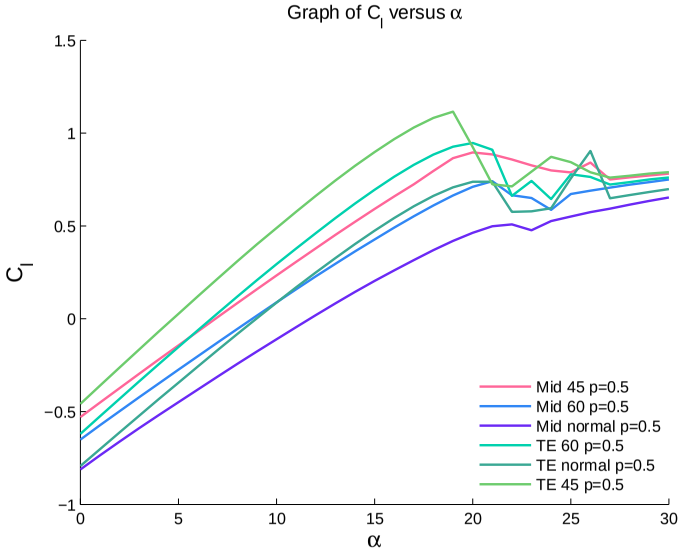

(d) C_L vs. α, ejections with guage pressure of 0.5

Fig. 4.10 Steady-state simulations: ejections with guage pressure of 0.5 and 0.05.

4.1.1 Flow-field observations

There are two regions of recirculating flow caused by the ejections near the suction side of the aerofoil: one has its locus before the ejection, the other just above the TE. These are regions of reversed, or separated, flow.

Velocity vector plots showed that the former was small and very close to the wall. The latter, a bit further from the wall, caused another recirculation point directly behind the TE where reverse flow from above met with flow from the pressure side of the aerofoil.

The loci and size of these regions of recirculating flow changed depending on the ejection *location*, but the second region was always just above the TE. It closely resembles the TE vortex that appears between 10° and 11° in the ejection-free steady-state results.

Both grew in size with increasing AoA, with P held constant, for any pressure P held constant. Increasing P moved the loci of the vortices. Due to the position of the second vortex for location 1 of the ejection, there was a reverse flow near to the wall over much of the rear half of the aerofoil (see figure 4.11) which increased the drag significantly more, as compared to location 2 - TE - as can be seen by comparing, e.g. figures 4.5a and 4.9a.

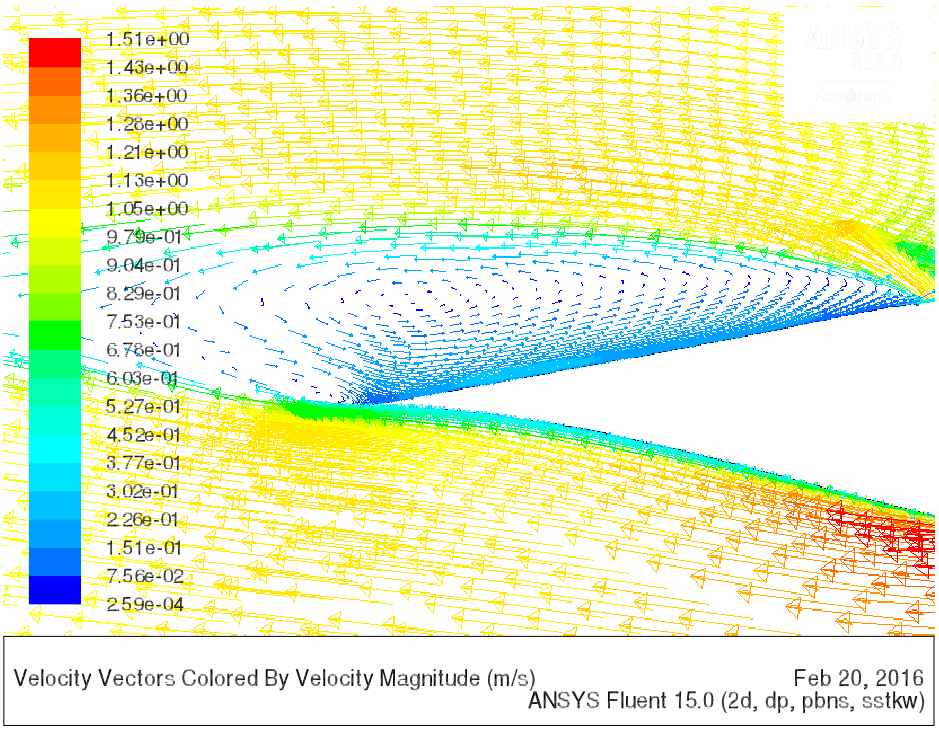

Fig. 4.11 Velocity vector plot showing reverse flow at $\alpha = 0°$, with ejection $P = 0.5$

For location 1, there was a larger second structure for all α at a certain P compared to the equivalent for location 2. The shape and size, and the strength, of the vortices also changed, as might be expected, due to the direction angle of the ejection.

The very small region of recirculating flow appears as a region of turbulence just before the ejection in the TKE plots. This smaller structure grew in size with increasing α. As an indicator of size, the estimated distances of these loci from the wall as a function of α are shown in figure 4.12 below.

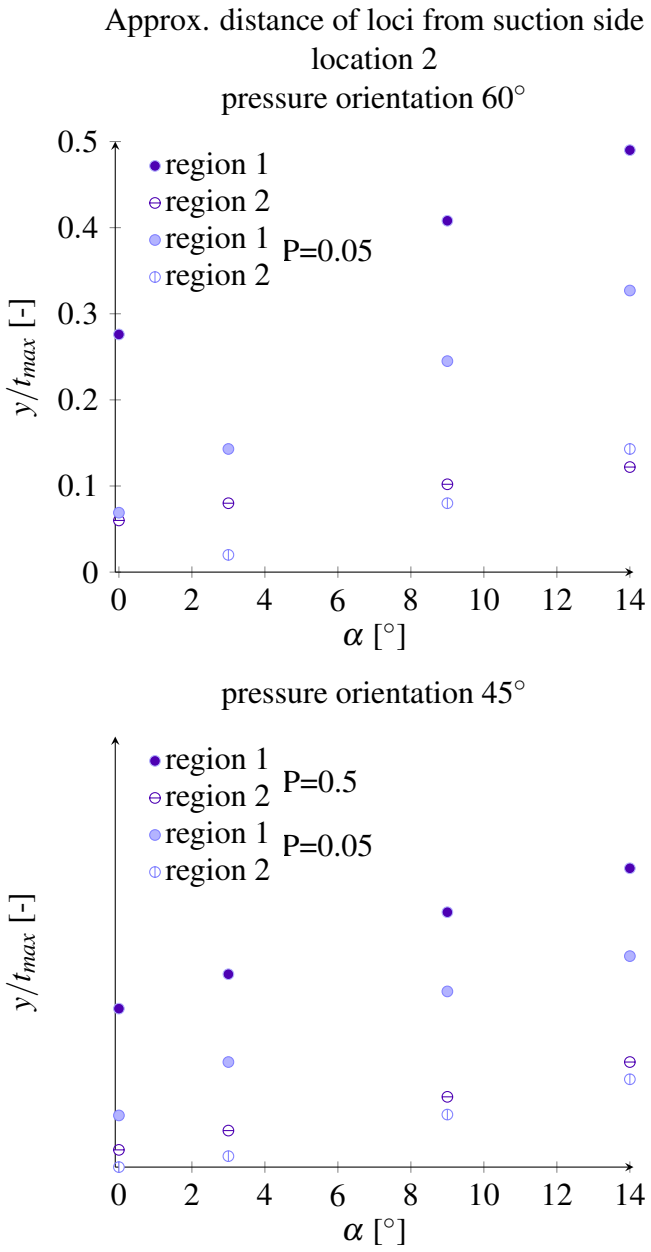

Fig. 4.12 Approximate distance of loci from suction side (fraction of $t_{\max}$)

Perring and Douglas [31] describe that their method to *delay* stall is to replenish a layer of fluid and thus re-energise it by injecting air into regions close to the wall where the

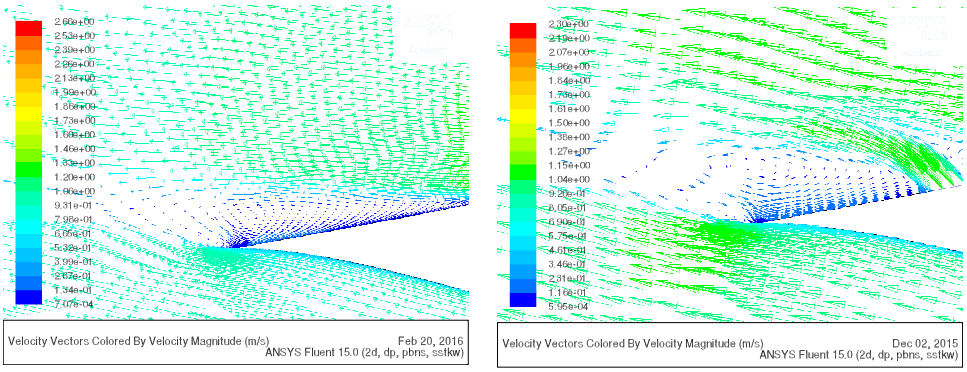

(a) Velocity vector plot showing TE vortex for $\alpha = 14°$, no ejection

(b) Velocity vector plot showing reverse flow for $\alpha = 14°$, with ejection location 2, $P = 0.5$, orientation 60°

Fig. 4.13 TE vortices comparison between no ejection and ejection location 2, $P = 0.5$, angled at 60° to the x-axis.

momentum is lower than in the regions near the free stream. Their study used tangential ejection (i.e. tangential to the surface) to delay stall. They also found a region of 'marked' turbulence just ahead of the slot, as seen in the TKE plots.

At about 14°, near to the static stall limit, the second recirculation region moves downstream. While it is smaller than the TE vortex in the case without ejection when at the same stage, the flow is more energetic.

Discussion

It was mentioned in 4.1.1 that there were 2 regions of reverse, or separated, flow on the suction side. Early indications all show that location 1 of the ejection worsens the scenario encountered with an LSB - of which a small LSB might not be of much consequence.

Figure 4.11 showed that there was a reverse flow near to the wall over much of the rear half of the aerofoil. Such a flow field with a thick area of separated flow causes a high drag and usually the lift breaks down. The same happens when the angle of attack is increased beyond the maximum lift.

The second structure for location 2 at the TE is similar to the TE vortex that develops between 10° and 11° for the steady case without ejection, and the eventual shedding of which triggers the TE stall. A visual comparison of the structures at 14° is seen in figure 4.13; it shows that the second vortex aft of the ejection closely resembles the TE vortex without ejection, but is slightly smaller as the ejection 'cuts through' the TE vortex, and supplies momentum which is quickly convected downstream.

Reversed flow occurs in regions of low KE. Large eddies, which bring outer-region momentum towards the wall, supply some downstream flow. The ejection supplies momentum to the near-wall region that, through turbulent diffusion and mixing, is quickly dissipated and convected downstream.

There is a recirculation region bounded by the flow coming from the pressure ejection. One could imagine drawing a 'dividing streamline' separating the recirculating flow from the main body of the ejection. What seems to happen is that the ejection 'splits' the separation into a small region before the ejection, and pushes the reverse flow by the action of the added adverse pressure gradient.

What can happen is that the separation occurs more towards the trailing edge and the flow, then, does not reattach. In this situation the separated region merges with the wake and may result in stall of the aerofoil (loss of lift). The second vortex induced a region of recirculating flow behind the TE. This may cause the aerofoil to stall with less force.

In general, the drag increases with increasing pressure of the ejection, as would be expected.

Effect on drag by ejection pressure

location 2 The plots show that for location 2 near the TE, the drag seems not to be much affected by the ejection pressure.

location 1 The ejection does increase the form drag significantly for location 1 of the ejection near mid-chord.

Effect on drag by angle of ejection

location 2 Any evidence of a relationship between the angle of the ejection to the flow and the drag would be hard to see since the ejection pressure itself has no significant bearing on the drag.

location 1 Between all the ejections drags there is very little evidence of a relationship between the angle of the ejection to the flow, and the excess drag.

Corresponding to the case of increasing drag with ejection pressure, the higher the pressure of the ejection, the less the lift.

Effect on lift by ejection pressure

location 1 $\frac{\Delta L}{\Delta \alpha}$ is significantly lessened.

This is most pronounced for the normal ejection. This effect dies away with increasing angle away from the normal.

Maximum lift $C_{\mathrm{L}\max}$ is significantly reduced.

Negative lift There is also creation of negative lift at low α - increasingly more so for increasing ejection pressure.
location 2 The lift-curve slope effect is less evident.

The extent to which the lift is decreased by the ejection pressure increases as the angle of ejection increases towards the normal; in other words the spread of the lift curves increases along with how much the ejection points into the normal direction.

4.2 Unsteady Simulations Results with Ejection

The flush jet ejection in the previous steady-state examples was not suitable for the unsteady case as it caused the simulation to become unstable. There needed to be a distance s for the flow from the ejection to develop. Therefore the geometry was changed to have an ejection 'channel', and the model was remeshed to this extent. The ejection channel for this study is shown in figure 4.14. Its location was chosen to be at the trailing edge location of figure 4.1 and 4.1 **Ejection location 2 - TE**, and at an angle of orientation of 20°. Its source location is the quarter-chord location $((0,0,0)$ on the domain) giving a distance s of $0.486c$.

The ejection pressure is formulated to correspond to the driving frequency in rad/s Ω, which in wind/marine turbine applications would relate to the combination of gust frequency and σ_w r.m.s. gust velocity. In application the force of the gust could be harnessed and used to generate the blowing.

Both sinusoidal and square wave forcing at a prescribed frequency were applied. The first ejection simulations run were with a simple sinusoid which peaks once per cycle. A sinusoidal-type ejection profile could be mathematically formulated to have a desired pulse width, remaining zero elsewhere. In this case the wave could be formulated to generate a specific temporal pulse width τ. A Gaussian functional form could be used to this end.

4.2.1 Sinusoidal ejection

The first tests are for a simple sinusoid.

$$P(t) = \begin{cases} 0 & \text{for } t < \tau \\ \frac{1}{2}P_0(1+\sin\omega((t-\tau)\pm\phi)) & \text{for } t \geq \tau \end{cases}$$

The pressure was formulated as above - the τ provides the time delay between the flow entering the velocity-inlet and reaching the LE of the aerofoil. The term ϕ is the phase applied to the ejection.

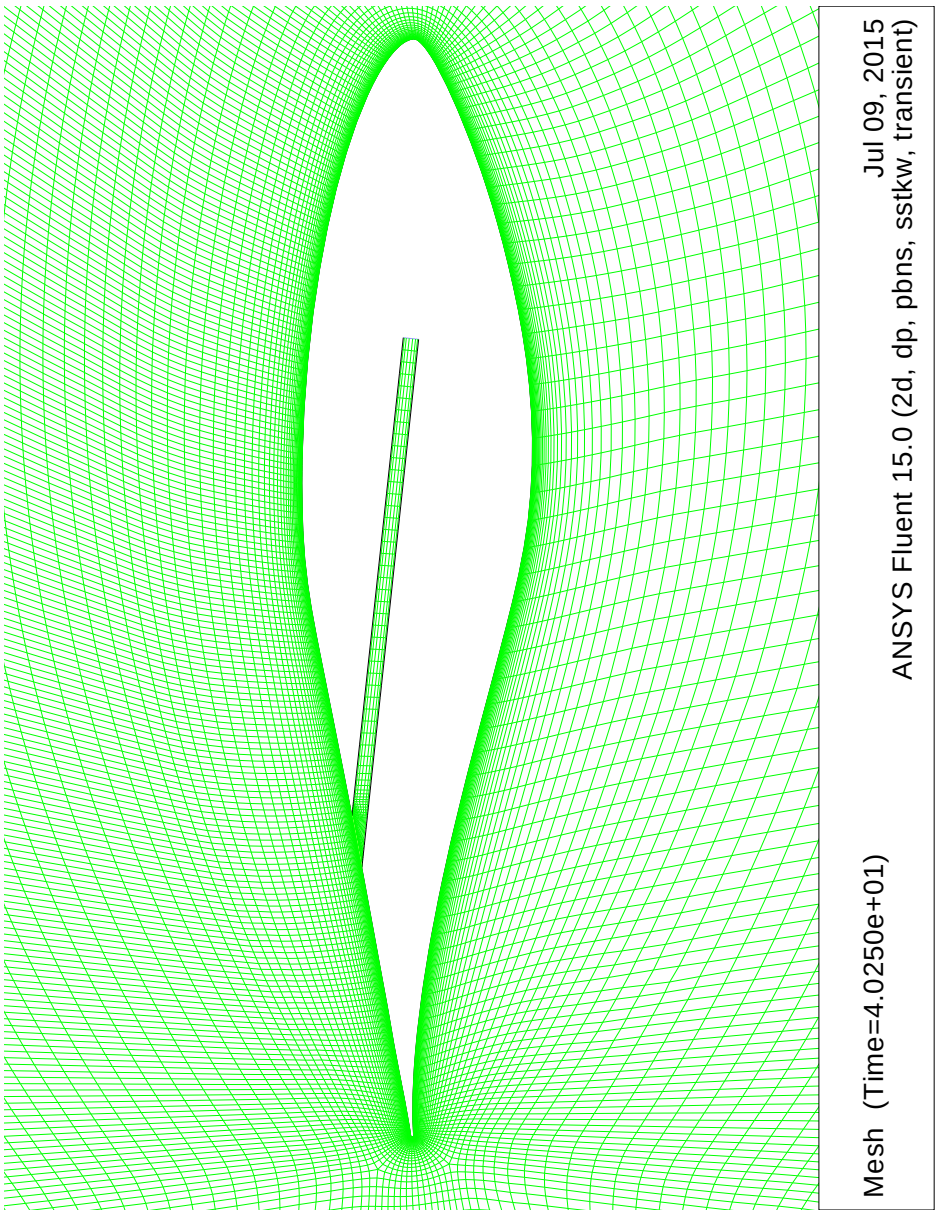

Fig. 4.14 Ejection channel

It was found, as detailed in Chapter 3, that the flow during the increasing angle branch was attached flow with small unsteadiness, higher lift and low drag, whereas during the decreasing angle-of-attack branch there was large unsteadiness, lower lift and higher drag. In other words, hysteresis is clockwise in the lift coefficient profiles and counter-clockwise in the drag coefficient profiles.

An oscillation cycle encompassing the range of angles of attack ordinarily encountered by a marine turbine was chosen on the advice of a team member. This cycle had a mean angle of attack α_0 of 5.5°, an oscillation amplitude α_1 of $\pm$2.5° and a reduced frequency k of 0.027.

The lift and drag hysteresis curves without the ejection are also shown in the figures. There is much less unsteadiness for the reason given in 3.3.2 that this loop terminates, or changes direction, before the angle of static stall. As such the hysteretic effect is less than some of the previous oscillation cycles studied in Chapter 3.

As mentioned before, aerodynamic hysteresis of an aerofoil refers to aerofoil aerodynamic characteristics as it becomes history-dependent, i.e. dependent on the sense of change of the angle of attack, near the static stall angle. Then, the coefficients of lift, drag and moment of the aerofoil are found to be multiple-valued, rather than single-valued functions of the angle of attack. Aerodynamic hysteresis is of practical importance because it produces widely different values of lift coefficient and lift-to-drag ratio for a given aerofoil at a given angle of attack.

As before, calculations start from an initial flow-field obtained from a well-converged steady-state computation where the aerofoil is positioned at the mean angle of attack and, in order to remove the influence of the initial flow-field, a sufficient number of cycles have elapsed so that a periodic solution is achieved.

Low pressure ejection

Figures 4.15a and 4.15b show the low pressure ejection simulations. The drag is still higher on the decreasing angle branch and the lift is still higher on the increasing angle branch, but the shape of the curves is altered. Phase is indicated in the legend entries.

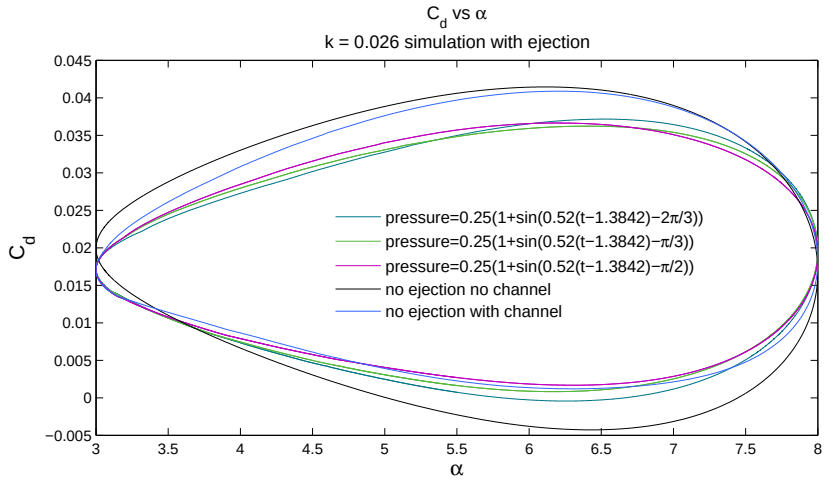

(a) C_{D} vs α for ejection pressure 0.25, varying phase through $-\frac{2\pi}{3}$,$-\frac{\pi}{2}$ and $-\frac{\pi}{3}$

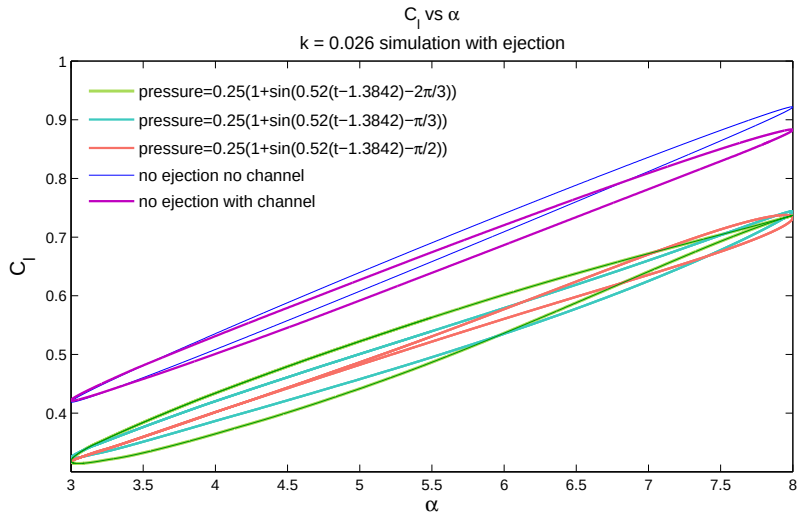

(b) C_{L} vs α for ejection pressure 0.25, varying phase through $-\frac{2\pi}{3}$,$-\frac{\pi}{2}$ and $-\frac{\pi}{3}$

Fig. 4.15 Low ejection pressure with phase delays of $-\frac{2\pi}{3}$,$-\frac{\pi}{2}$ and $-\frac{\pi}{3}$

Medium pressure ejection

Figure 4.16 shows the pressure ejection in action.

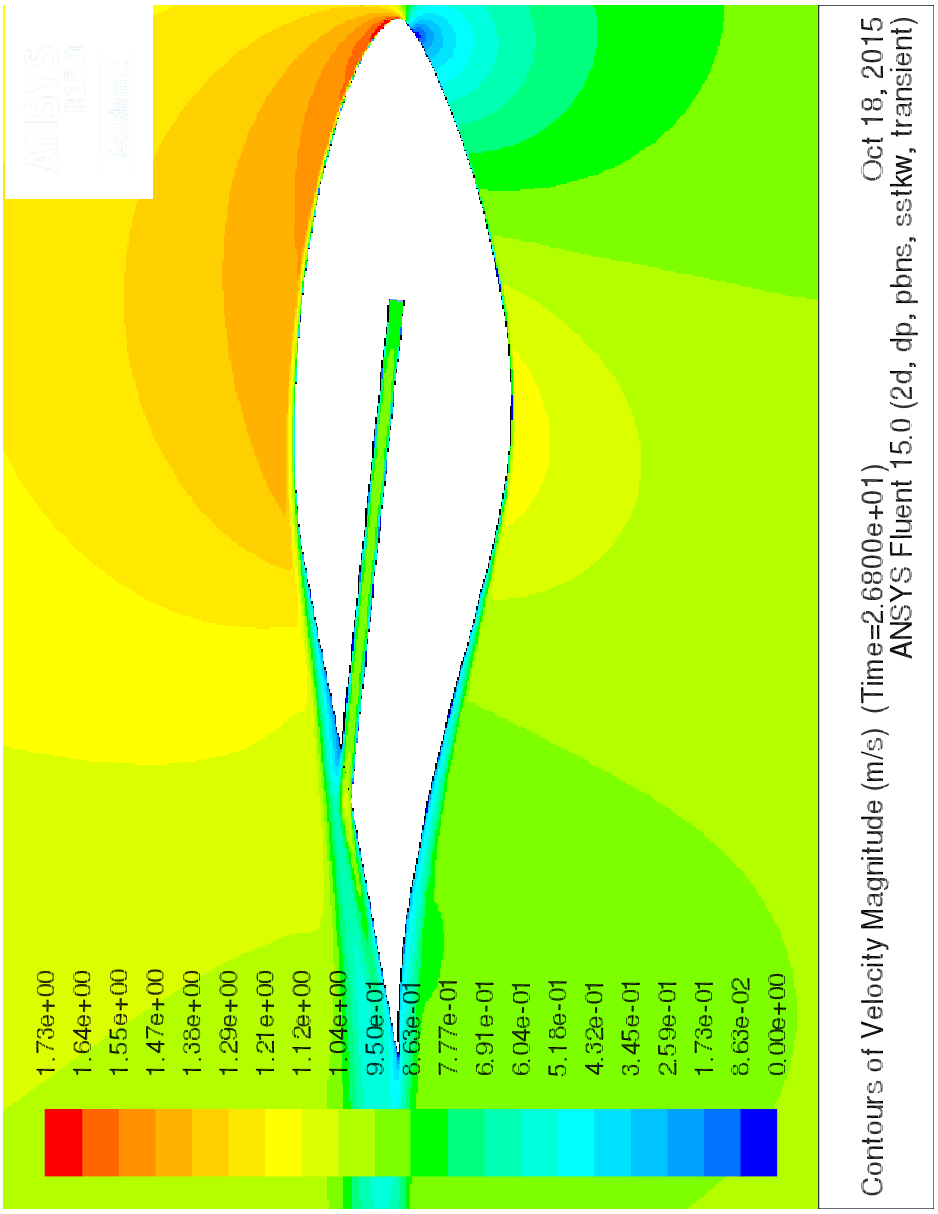

Fig. 4.16 Medium pressure ejection flow from channel at 7.05° on the upstroke

The plots of lift and drag corresponding to the medium pressure ejection, including phase of $-2\pi/3$, are shown in figures 4.17b and 4.17a respectively.

The unsteady C_p distributions for different phases of the ejection are shown in figures 4.19a - 4.19d. Figure 4.18 shows 'frames' of velocity magnitude contour plots through the cycle.

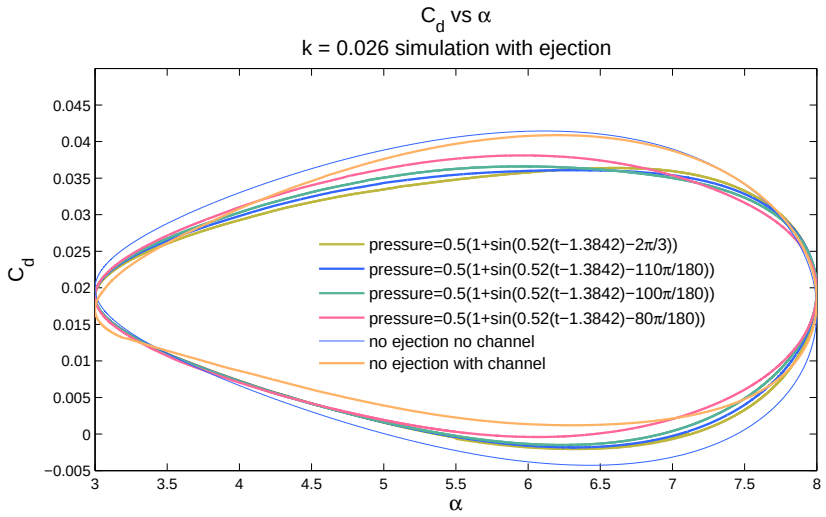

(a) C_{D} vs α for ejection pressure 0.5, phases through $-\frac{2\pi}{3}$,$-\frac{110\pi}{180} = 0.611\pi$, $-\frac{100\pi}{180} = 0.555\pi$ and $-\frac{80\pi}{180} = 0.444 \cdot \pi$

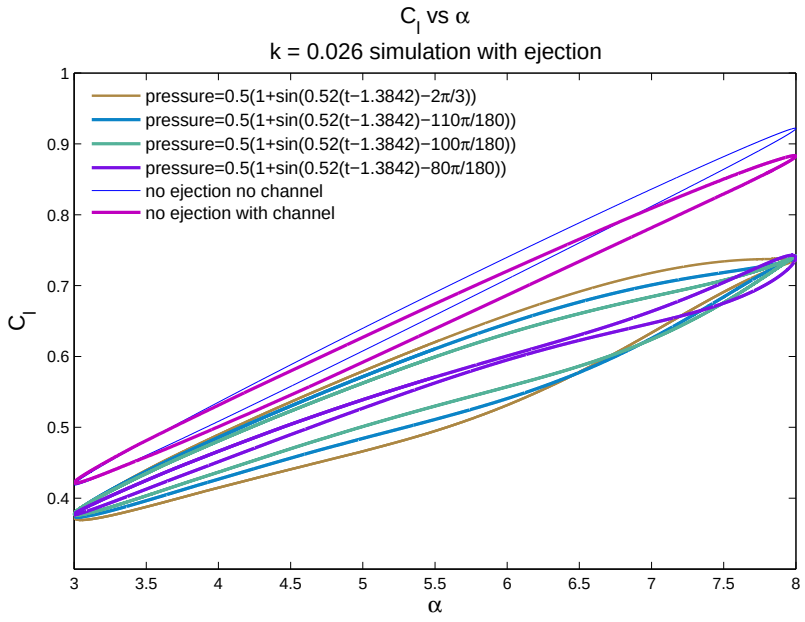

(b) C_{L} vs α for ejection pressure 0.5, varying phase through $-\frac{2\pi}{3}$,$-\frac{110\pi}{180} = 0.611\pi$, $-\frac{100\pi}{180} = 0.555\pi$ and $-\frac{80\pi}{180} = 0.444 \cdot \pi$

Fig. 4.17 Medium ejection pressure with phase delays of $-\frac{2\pi}{3}$,$-\frac{110\pi}{180}$, $-\frac{100\pi}{180}$ and $-\frac{80\pi}{180}$

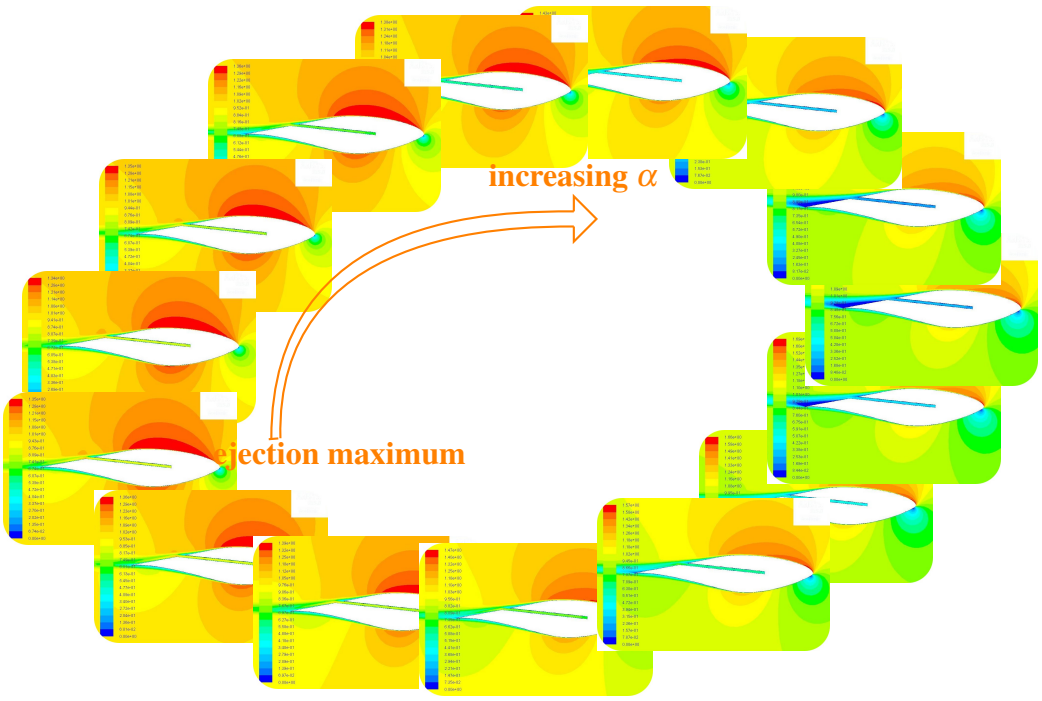

Fig. 4.18 Medium pressure ejection for phase delay of $-\frac{2\pi}{3}$

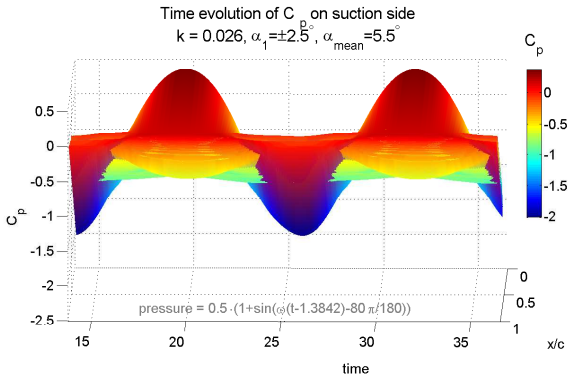

(a) C_p vs time for ejection pressure 0.5, phase $-\frac{80\pi}{180} = 0.444 \cdot \pi$

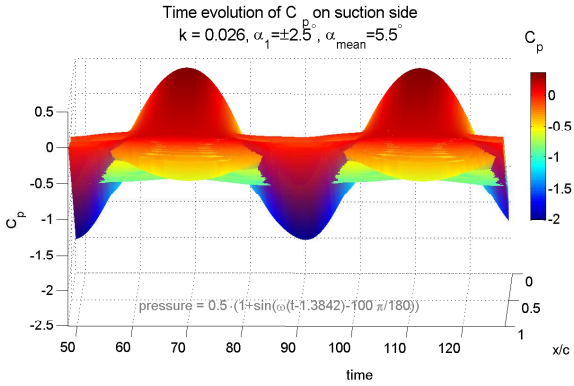

(b) C_p vs time for ejection pressure 0.5, phase $-\frac{100\pi}{180} = 0.555 \cdot \pi$

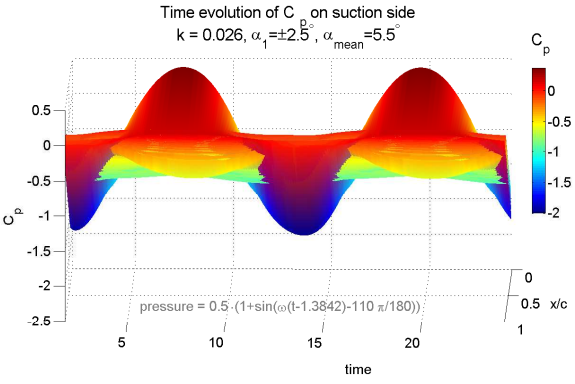

(c) C_p vs time for ejection pressure 0.5, phase $-\frac{110\pi}{180} = 0.611 \cdot \pi$

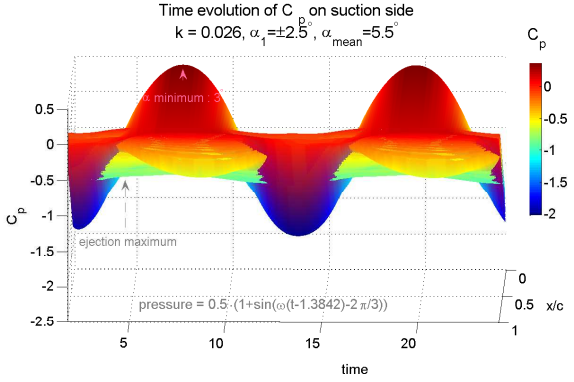

(d) C_p vs time for ejection pressure 0.5, phase $-\frac{2\pi}{3}$

Fig. 4.19 C_p vs time for medium ejection pressure for varying phase delays

High pressure ejection

The lift and drag for the high pressure ejection are shown in figures 4.20a and 4.20b.

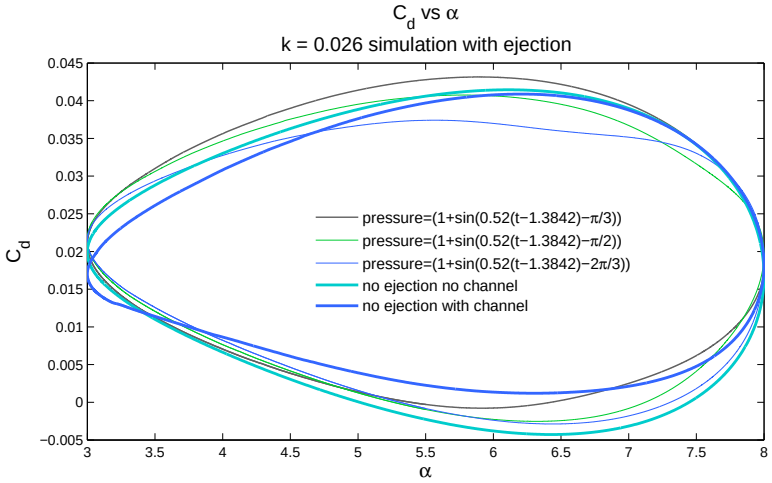

(a) C_{D} vs α for ejection pressure, varying phase $-\frac{2\pi}{3}$,$-\frac{\pi}{2}$ and $-\frac{\pi}{3}$

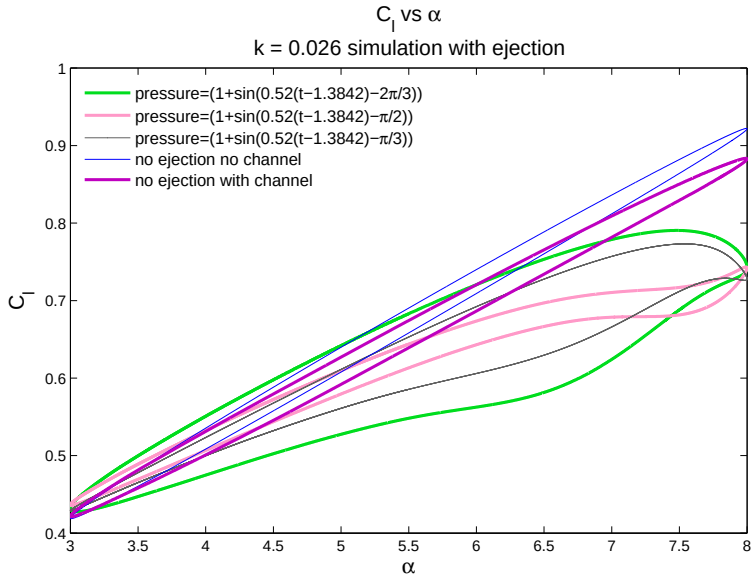

(b) C_{L} vs α for ejection pressure, varying phase $-\frac{2\pi}{3}$,$-\frac{\pi}{2}$ and $-\frac{\pi}{3}$

Fig. 4.20 High ejection pressure with phase delays of $-\frac{2\pi}{3}$,$-\frac{\pi}{2}$ and $-\frac{\pi}{3}$

4.2.2 Discussion

The animation of figure 4.21 shows the cycle and where the angle of attack, and ejection pressure, reach maximum - see also figure 4.18. This cycle is for a delay in phase of $-2\pi/3$,

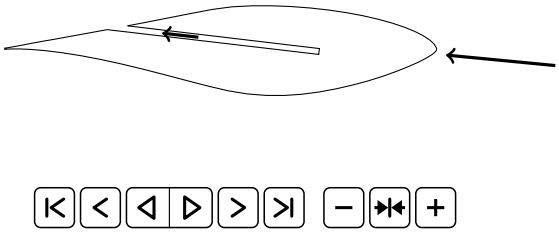

Fig. 4.21 Animation: pressure ejection for phase delay of $-\frac{2\pi}{3}$

which was determined to be close to the seeming best phase delay for the purpose. This is counter-intuitive, because the pressure ejection reaches maximum on the downstroke, yet this formulation of the pressure equation gave the results that were sought for the lift curve.

The ejection pressure reaches a maximum on the downstroke, but has been ejecting for most of the period. One explanation for how this works is that it is providing the boundary layer with extra energy and more fluid, off-setting the pressure vacuum that leads to increased lift.

The drag is also reduced in the low and medium pressure cases most noticeably. The high pressure ejection with a phase of phase of $-2\pi/3$ also reduced the drag. Much of the lift is also preserved at the lowest α. A slight but perceptible change between the unsteady C_p distributions for different phases of the ejection in figures 4.19a - 4.19d can be seen.

4.2.3 Square Wave ejection

A square wave ejection pulse was formulated, as well as a 'half'-square wave, as shown in figure 4.22, that would provide an ejection more targeted in relation to α.

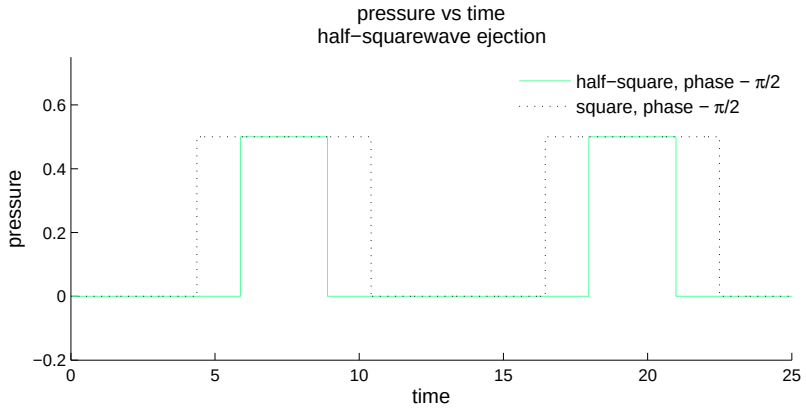

Fig. 4.22 Pressure vs. time, square wave and half square wave ejection with phase of $-\frac{\pi}{2}$

The equation for the square wave is:

$$\frac{P_0}{2}\left(1+\frac{\sin(\omega(t-\tau)-\phi)}{|\sin(\omega(t-\tau)-\phi)|}\right) \tag{4.1}$$

The equation for the half-square wave is:

$$\frac{P_{max}}{4}\left\{\left|\frac{sin(2\cdot\omega(t-\tau)-\phi)}{|sin(2\cdot\omega(t-\tau)-\phi)|}-\frac{sin(\omega(t-\tau)-\phi)}{|sin(\omega(t-\tau)-\phi)|}\right|-\ldots\right.$$
$$\left.\left(\frac{sin(2\cdot\omega(t-\tau)-\phi)}{|sin(2\cdot\omega(t-\tau)-\phi)|}-\frac{sin(\omega(t-\tau)-\phi)}{|sin(\omega(t-\tau)-\phi)|}\right)\right.$$

It was difficult to run the square wave ejections successfully in this way. It may be that the reason for this was the way the square wave was formulated: it would seem that the reason for this is that the simulation would fail unless pressure was non-zero at the time τ when the ejection begun. Figure 4.23 shows the graph of a simulation which ran successfully using this method.

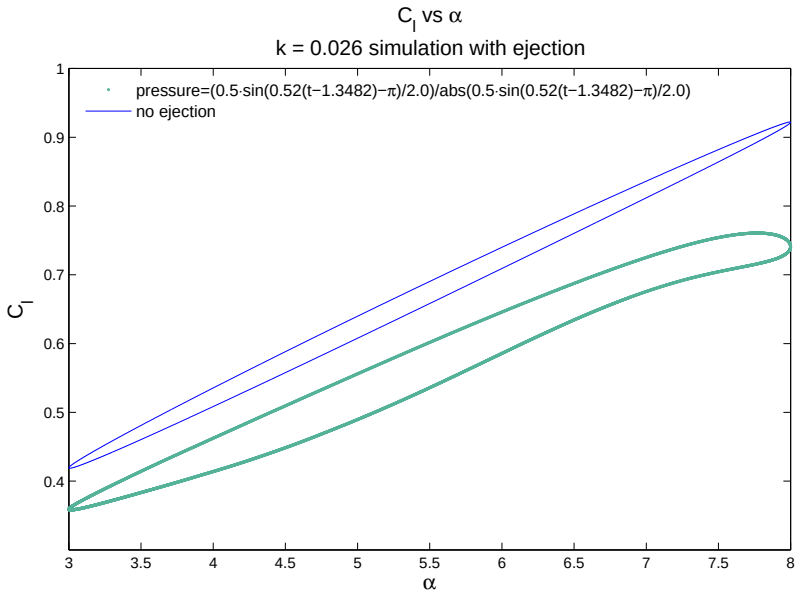

Fig. 4.23 C_L vs. α, square wave ejection with phase of $-\pi$

A conditional statement was found to work consistently and also to be simpler and more effective. The following conditional statement in the UDF was used to replicate a square wave profile:

```
DEFINE_PROFILE(blowing, thread, position)
{
face_t f;
real t = CURRENT_TIME;
real pressure;
 begin_f_loop(f, thread)
   {
      pressure = sin(0.52*(t-1.3482)-(5*PI/7));
       /* local variable */

      if(pressure > 0.75)
        {
           F_PROFILE(f, thread, position) = 0.5;
        }
      else
        {
           F_PROFILE(f, thread, position) = 0.0;
        }
   }
 end_f_loop(f, thread)
}
```

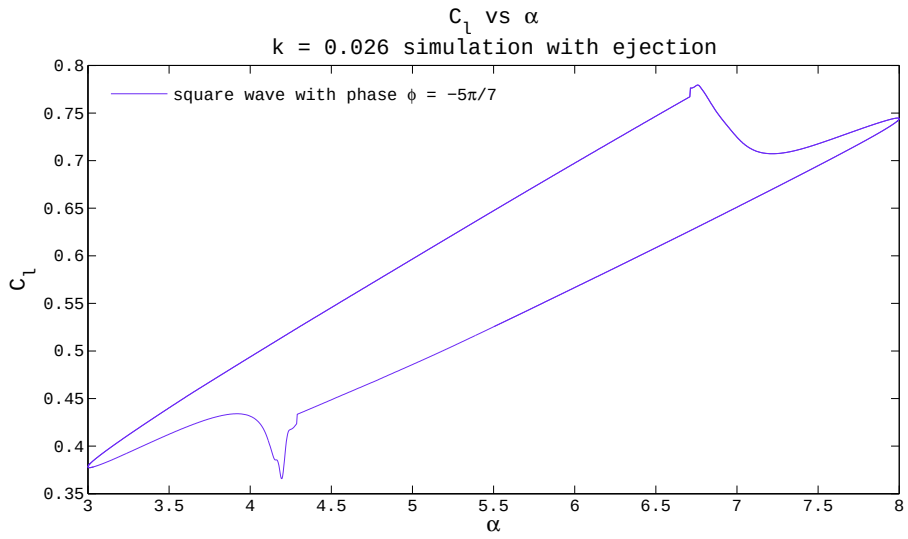

Fig. 4.24 C_L vs. α, square wave ejection with phase of $-\frac{5\pi}{7}$

In this simple example of a square wave, the peak pressure occurs before the peak in the sine profile. It occurs in figure 4.24 when $\sin(\omega(t-\tau)-\phi) > 0$. It can be seen that the immediate response of the ejection cancels much of the lift. There could be a single puff that issues forth to respond to a sudden change of incidence.

However, the conditional statement did not work as expected either. From the above UDF it should be that the ejection continues for only a quarter of the cycle, but the ejection has continued for longer than that. There was not enough time to investigate the cause of this.

Chapter 5

Conclusions and Future Recommendations

Section 5.1 presents an overarching, unified conclusion relating to the aims and objectives as laid out in Chapter 1.

Section 5.2 presents a summary of the main conclusions drawn from the validation study presented in chapter 3.

Section 5.3 presents a summary of the main conclusions drawn from the ejection-case study presented in chapter 4.

Suggestions for future work are given at the end of sections 5.2 and 5.3: 5.2.2 and 5.3.2.

5.1 Overarching Conclusion

The initial aim of the work was to use CFD to simulate a device to trigger dynamic stall (DS), and early on this device was chosen to be in the form of an ejection jet.

The ejection does not cause DS at a lower α. Instead, it is thought that as fluid is discharged from location 2 of figure 4.1 near the TE, the energised flow fills the wake and reduces the drag - in some cases. By a process of turbulent mixing a counter-rotating pair of vortices form. One of these occupies the same space as the TE vortex.

This TE vortex is slightly smaller than the one formed in the no-ejection case between 10° and 11°, which might account for the reduction in lift.

The ejection near the TE appears to simultaneously cut through the original TE vortex, of which the normal means of stall occurs by vortex-shedding, and push the reverse flow (or the locus of the TE vortex) towards the TE. If this separation occurs more towards the TE and

the flow, then, does not reattach, then the separated region may merge with the wake and this may result in stall of the aerofoil.

Another recirculation region was induced directly behind the TE for the ejection cases, and reverse flow from above met with flow from the pressure side of the aerofoil. This may cause the aerofoil to stall with less force.

It was an aim of this investigation to simulate dynamic stall in 2D and to produce a validation case. This was done by using CFD to model an aerofoil undergoing pitching oscillations or subjected to flow oscillation.

The following section summarises the qualititative aspects of the validation study and findings of a comparison between the two types of motion.

5.2 Validation Simulations

NREL performance data produced by the OSU - steady and unsteady - which are publicly available on the NWTC information portal [46], are used as a benchmark against which to validate the use of the commercial Fluent URANS code, in conjunction with the k-ω SST turbulence model for closure.

Static aerofoil simulations were compared to steady-state experimental data. Following this, unsteady simulations of oscillating flow and pitching aerofoil were both compared with pitching data, finding good agreement on the whole.

The following subsection, 5.2.1, gives an overview of some of the main findings and conclusions drawn from the validation study simulations.

5.2.1 Summary of validation tests run and findings

Static aerofoil results were shown in subsection 3.2.1 of Chapter 3, in figures 3.2a and 3.2b, and were plotted next to two sets of experimental data - compared to which the slope $\frac{\Delta L}{\Delta \alpha}$ was predicted quite well and the characteristic 'double-hump' of a TE-stalling aerofoil was reproduced by the simulation. The simulations were run steady below the static stall angle and unsteady above. Steady simulations had overall better agreement.

It was concluded that running unsteady is not enough to guarantee a real solution, presumably due to 3D effects being more prevalent at separated α and to turbulence effects introduced by the model at high AoA.

Two unsteady CFD tests were undertaken:

1. simulation of pitching aerofoil (PA)

2. simulation of oscillating flow (OF)

whereby the same sine waveform of the experiment for a pitching aerofoil in a wind tunnel - equation 3.1 - was written in C-syntax in a UDF to either oscillate the sliding mesh or the inlet-velocity vectors.
Case details of simulation runs were provided in section 3.3, table 3.1. Table 5.1 below scores the PA and OF simulations in terms of their closeness to the experimental data.

			best prediction of …								
			initial curve	$C_{L_{max}}$	α_{max}	stability at hi α	hysteresis	secondary vortex	reattachment	intersection	additional remarks
High AoAs table 3.1, r 1		k=0 .027									
	PA	L	x			x	x	x	x	x	hysteresis representative, tho
		D	x			x	x		x		loop as if translated upwards.
											PA lift excessive
	OF	L	x	x	x				x	x	and stall delayed more.
		D							x		poor prediction of 2 nd 'ry vortex
											suggests phase shift
table 3.1, r 2		k=0 .08									
	PA	L	x	x		x	x		x		Drag well-captured by PA
		D	x			x	x		x		inc. spike at highest α
	OF	L	x		x	x	x				More hysteresis with higher k.
		D									OF shows fluid reentrainment.
Moderate AoAs table 3.1, r 3		k=0 .026									
	PA	L	x	x	x				x		Much less unsteadiness
		D	x				x		x		loop reverses before
											angle of static stall.
	OF	L	x						x		less max AoA is from α_{max},
		D									the smaller the loop.
table 3.1, r 4		k=0 .077									More hysteresis with higher k.
	PA	L	x						x	x	
		D	x				x		x		
	OF	L		x	x		x				
		D									

= not applicable x = good agreement

Fig. 5.1 Table summarising agreement of simulations.

High AoA oscillation simulations

Substantial differences exist between the two types of motion - pitching aerofoil and oscillating flow - although each had, at times, better agreement of one over the other. PA is in best agreement overall.

Tables 3.1 and 5.1, simulation of first row (α_0 = 13.3°, α_1 = ±10.4° and k = 0.027)
There is an apparent *phase shift right* of the lift curve of both PA and OF, as compared to the experiment - OF more so - as apparent from the decreasing angle branch for the reasons that:

1. Sudden lift increase during downstroke attributable to secondary vortex occurs slightly in advance for the OF results as compared to the PA results, and occurs in advance of the corresponding increase in experimental lift.

2. The hysteresis lift C_{Lhys} for oscillating flow, rivals C_{Lmax} for flow on the upstroke.

The second 'hump' of the static aerofoil C_l seems to correspond to the spike in lift in the downstroke portion of the curve: the secondary vortex. The double-hump of an aerofoil lift characteristic has been linked in the literature to the existence of a secondary vortex. There seems to be a brief window of opportunity for the secondary vortex to be shed, and this is delayed until the downstroke portion of the curve when the aerofoil is in motion.

Tables 3.1 and 5.1, simulation of second row (α_0 = 12.65°, α_1 = ±10.35°, k = 0.08)

- More hysteresis with higher k in agreement with theory and experiment.
- OF displays a tendency to have larger hysteresis loops - could be explained in terms of inertial effects.
- C_{Lmax} and high α better replicated by PA in contrast to k = 0.027.
- The drag is very well captured by the PA simulation (even the spike at the highest α)
- Degree of reattachment lift and drag OF - poor agreement
  PA - good agreement

The flow would have to be oscillating at a lesser frequency to allow time for the fluid to settle, or adjust to its inputs, and this is seen by observing the closer agreement between PA and OF for the $k = 0.027$ case in figure 3.7 at low α.
The OF curve was rounded at the lowest part of its cycle; reattachment only occurred when the aerofoil terminated/changed direction at the lowest α. This was purported to be due to a delay in fluid re-entrainment: the flow will reattach to the surface due to the energy recovered from the entrainment in the turbulent shear layer.

Moderate AoA oscillation simulations

Tables 3.1 and 5.1, simulations of third row (α_0 = 8.45°, α_1 = ±5.05°, k = 0.026)

- Much less unsteadiness for these moderate AoA oscillations. No dynamic stall in this case.
- The simulation lift was concave on the decreasing angle branch (both PA and OF), while the experimental lift curve was convex - the simulation wrongly predicts the hysteresis and this appears to be due to an overprediction of reattachment during the decreasing angle branch.

Tables 3.1 and 5.1, simulations of fourth row (α_0 = 8.35°, α_1 = ±4.95°, k = 0.077)

- Lift curve for OF best predicts hysteresis, C_{Lmax} and α_{max}. This is the best agreement of the OF simulation in the validation study.

Pressure distributions

Differences are also visible from 'snapshot' surface pressure - C_p - plots, and from unsteady pressure distributions. There was a slightly raised pressure distribution around the aerofoil subjected to oscillating flow in 3.3.4, compared to pitching. The opposite was true for corresponding times during the downstroke at low α. This might be due to differences in shear stress at the wall and could be examined by looking at the near-wall velocity profile. C_p plots were also compared with the corresponding experimental data. Interestingly, figure 3.19d shows that at the high α of 16.7° while decreasing, the experimental pitching C_p is closer to 'oscillating flow' at this angle.

5.2.2 Future Recommendations

Data for oscillating flow impinging on an aerofoil should be collected from experiments to match test conditions of pitching aerofoil experiments in order to further examine the patterns of hysteresis.
In this case the hysteresis effect disappears as the input changes more slowly, i.e. the hysteresis loops get smaller with smaller reduced frequency. The loops seen may occur purely because of a dynamic lag between input and output. This effect meets the description of hysteresis, but is often referred to as rate-dependent hysteresis to distinguish it from hysteresis with a more durable memory effect.

Such a way of examining the nature of this hysteresis may be to create 'lag plots' which relate the present to the past, and which are used when trying to predict the present or future from past observations.
This is done by plotting the current value, say the lift, on the vertical axis, and the value from an earlier time on the horizontal axis. The first lag plot could be e.g. 45 seconds earlier, the second 90 seconds, the third 135 seconds and so on. Interesting patterns may emerge.
The idea is that one can predict the present value by, for example, rotating the lag 1 plot by 2 x 45 degrees horizontally, holding the vertical axis fixed.
The data seem to lie on a disk that exists in 2D lag-space. The lag-space of a given time series is used in scalar time series analysis. Looking at the edge of the disk, so that it looks like a straight line, will indicate that the present can be predicted by the past, with a few outliers, using observations via a simple inner equation. The field that looks at data in this way is known as scalar time series analysis.
This kind of hysteresis is often referred to as rate-dependent hysteresis. If the input is reduced to zero, the output continues to respond for a finite time. This constitutes a memory of the past, but a limited one because it disappears as the output decays to zero. The phase lag depends on the frequency of the input, and goes to zero as the frequency decreases. When rate-dependent hysteresis is due to dissipative effects like friction, it is associated with energy loss [52].

5.3 Ejection Simulations

Ejection locations for the steady ejection simulations are shown in figure 4.1. The ejection channel used in the unsteady simulations is shown in figure 4.14.

Steady Simulations with Ejection

- Initial/total guage pressure was varied in increments of 0.05 (Pa) and the steady-state simulations for each α were cycled through for each pressure value.

- This was repeated for each of the two pressure ejection locations in figure 4.1, leading to six charts each for C_l and C_d, three charts each for either location corresponding to a certain angle of orientation of the ejection.

- The ejection tests appear to reduce the lift curve slope, $\frac{\Delta L}{\Delta \alpha}$ - referred to as a *decambering* effect - as well as reducing the $C_{\mathrm{L}\max}$.

- For all the ejection simulations there are a counter-rotating pair of vortices behind the ejection

as observed from velocity vector plots and streamlines. These increase the turbulent wake. One indication of the relative size of the vortices was by measuring the distance from the aerofoil wall of the loci of these vortices. This was crudely done using a ruler, while maintaining the same focal plane, and reading into Fluent the different solution data files. From these observations it was seen that: *The counter-clockwise-rotating vortex with its locus above the TE for the location 2 ejection bore the most relation to the TE vortex that develops between* 10° *and* 11° *for the steady case without ejection, and the eventual shedding of which triggers the TE stall. This caused another recirculation point directly behind the TE where reverse flow from above met with flow from the pressure side of the aerofoil and this rotated clockwise.*
What seems to happen is that the ejection 'splits' the separation into a small region before the ejection, and pushes the reverse flow by the action of the added adverse pressure gradient.

- **The separation may occur more towards the trailing edge and the flow may not reattach: in this situation the separated region will merge with the wake and this may result in stall of the aerofoil.**

A shortcoming of this section is that the pressure was not incremented for each α as per the sinusoidal ejections to follow.

5.3.1 Unsteady Simulations with Ejection

The flush jet ejection in the previous steady-state examples was replaced by an ejection channel. The ejection channel is shown in figure 4.14. Its location was chosen to be at the TE location 2 of figure 4.1. There needed to be a distance s for the flow from the ejection to develop. The flow developed from the origin to the point of exit.

- Both sinusoidal and square wave forcing at a prescribed frequency equal to the oscillation frequency were applied for the pressure. The first ejection simulations run were with a simple sinusoid - formulated as 4.2.1.

- A delay in phase of the ejection ϕ of $-2\pi/3$ was determined to be close to the seeming best phase delay for the purpose.

- The ejection pressure reaches a maximum on the downstroke (see the animation of figure 4.21).

It has been ejecting for most of the period. One explanation is that it is providing the boundary layer with extra energy and more fluid, offsetting the pressure vacuum that leads to increased lift.

- For the square wave ejections, a square wave and a half square wave were formulated, but these simulations had limited success due to the fact that they appeared to fail unless pressure was non-zero at the time τ.
- A conditional statement was simpler and more effective.

5.3.2 Future Recommendations

The following questions arise from the conclusions of this study:

1. Whether the present location is optimum
2. The ejection works at low frequency - will that scale up to high frequency?
3. With increasing AoA will ejection be engulfed by the recirculation flow?
4. Will there be significant change of effectiveness due to local flow state?

A change in effectiveness due to local flow state was also observed in [30] which employs a microtab, located on the suction side for lift-mitigation.
It would have been preferable to run further unsteady ejection simulations, contrasting different k and taking in a different, higher range of α. The results also depend on how well the RANS model predicts the mixing process. A more high-fidelity CFD model should be used before the model phase.
The ejection alters the pressure difference between the pressure side and the suction side of the aerofoil. While passive FC by continuous blowing by way of LE slots and TE flaps on aircraft leads to a significant increase in lift with a large drag penalty, for the ejection presented in this study the opposite seems to be true; there is a significant decrease in lift with low drag penalty and in some cases a decrease in drag (e.g. figure 4.17a) by energising flow in the wake.
A sinusoidal-type ejection profile could be mathematically formulated to have a desired pulse width, remaining zero elsewhere. In this case the wave could be formulated to generate a specific temporal pulse width τ. This would perform a duty cycle $\Delta\alpha = \frac{\tau}{T}$ - where T is the period of oscillation - for a more precise targeting of lift reduction.
Therefore, a next step might be to formulate, for the ejection, a Fourier decomposition for a pulse. Due to time constraints it was not possible to embark on this investigation for the

current study. This would provide an ejection more targeted in relation to α in the simulation.
A 3D mesh for the steady ejections was made as shown in figure 5.2 for location 1 of the steady-state ejections in 4.1. There was to be assigned a periodic BC on the surface of the mesh that has the ejection. Periodic BCs are often chosen for approximating a large (infinite) system. This would enable us to examine the 3D effects of a sequence of equally-spaced ejections and their influence on one another.

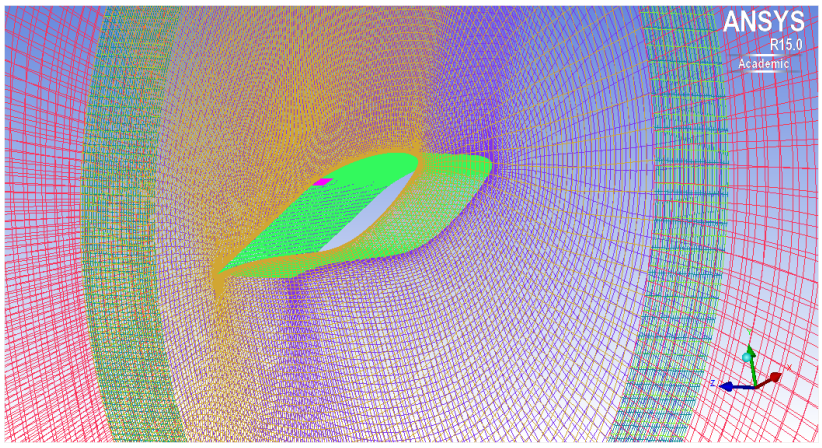

Fig. 5.2 3D mesh with ejection.

The ejection holds promise for the low-frequency case presented. Perhaps even negative lift caused by stronger ejecting could be exploited to use as a brake.
Further modelling in 3D would be desirable to investigate different locations of the ejection along the span of a turbine blade. How to implement it as a design would be the next challenge. Passive devices are generally preferred for low-cost and easier maintenance. On the downside, most engineering flows consist of complex, unsteady motions that limit the ability to use passive control. If the gust strength could be harnessed in some way to produce the ejection that would be an interesting and convenient breakthrough.
The final stage would be to use a Blade Element Momentum (BEM) method to calculate the theoretical loads on the blade and then estimate the power production of a turbine fitted with such a device.

References

[1] L. Carr, "Progress in Analysis and Prediction of Dynamic Stall," *J. of Aircraft*, vol. 25, pp. 6–17, January 1988.

[2] L. Prandtl and O. Tietjens, *Applied Hydro-and Aeromechanics: Based on the Lectures of L. Prandtl*. New York: Courier Dover Publications, 1973.

[3] D. M. Somers, "Design and Experimental Results for the S809 Airfoil," SERI Subcontract Report HK-6-06075-1, NREL, 1997.

[4] R. Mayle, "Transition in a separation bubble," *J. Turbomach.*, vol. 118, p. 752–759, 1996.

[5] S. Mittal and P. Saxena, "Prediction of Hyteresis Associated with the Static Stall of an Airfoil," *AIAA*, vol. 38, no. 5, pp. 933–935, 1999.

[6] J. Hoffmann, "Effects of Freestream Turbulence on the Performance Characteristics of an Airfoil," *AIAA*, vol. 29, no. 9, pp. 1353–1354, 1991.

[7] M. M. Zifeng Yang, Hirofumi Igarashi and H. Hu, "An Experimental Investigation on Aerodynamic Hysteresis of a Low-Reynolds Number Airfoil, 46th aiaa aerospace sciences meeting and exhibit," *AIAA*, January 2008.

[8] J. Russell, "Length and Bursting of Separation bubbles: A Physical Interpretation," in *Science and Technology of Low Speed Motorless Flight, NASA Conference Publication*, vol. 2085 Part 1, 1979.

[9] G. G. R. Reuss Ramsay, M.J. Hoffman, "Effects of Grit Roughness and Pitch Oscillations on the S809 Airfoil: Airfoil Performance Report," NREL Contract Report DE-AC36-83CH10093, National Renewable Energy Laboratory [NREL], 1999.

[10] K. M. W. McCroskey, L. Carr, "Dynamic Stall Experiments on Oscillating Airfoils," *AIAA J.*, vol. 14, no. 1, 1976.

[11] G. S. R. Pereira and M. D. Pavel, "Validation of the Beddoes-Leishman dynamic stall model for horizontal axis wind turbines using MEXICO data," *Wind Energy*, vol. 16, pp. 207–219, August 2013.

[12] R. G. W. Sheng and F. Coton, "Modifield Dynamic Stall Model for Low-Mach Numbers," *Journal of the Society of Solar Energy Engineering*, vol. 130, no. 3, 2008.

[13] G. B. McCullough and D. E. Gault, "Examples of three representative types of airfoil-section stall at low speed," Technical Note 2502, National Advisory Committee for Aeronautics, 1951.

[14] J. B. Melvill, "An Experimental Study of the Stalling of Wings," Reports and Memoranda No. 1588, British A.R.C., 1933.

[15] L. M. M. P. Shengyi Wang, Derek B. Ingham and Z. Tao, "Numerical investigations on dynamic stall of low reynolds number flow around oscillating airfoils," *Computers and Fluids*, vol. 39, pp. 1529–1541, 2010.

[16] M. R. Philippe Wernert, Wolfgang Geissler and J. Kömpenhans, "Experimental and Numerical Investigations of Dynamic Stall on a Pitching Airfoil," *AIAA*, vol. 279, no. 5, pp. 982–989, 1996.

[17] D. Greenblatt and I. Wygnanski, "Effect of Leading Edge Curvature and Slot Geometry on Dynamic Stall Control," *J. of Aircraft*, vol. 40, May-June 2003.

[18] T. Lee and P. Gerontakos, "Investigation of flow over an oscillating airfoil," *J. Fluid Mech*, vol. 512, pp. 313–341, 2004.

[19] K. Tchon, "Flow Visualisation Investigation of Dynamic Stall on a Pitching Aerofoil," *AIAA*, vol. 27, no. 89-0842, 1989.

[20] P. R. A. Patterson and B. R. Ramaprian, "Surface Pressure Measurements on a Pitching Swept Wing in a Water Channel," *AIAA*, vol. 33, no. 10, pp. 1871–1879, 1995.

[21] E. Bossanyi, "The Design of Closed Loop Controllers for Wind Turbines," *Wind Energy*, vol. 3, pp. 149–163, 2000.

[22] *Developments in Individual Blade Pitch Control*, DUWIND, 2004.

[23] H. M. T.J Larsen and K. Thomsen, "Active Load Reduction Using Individual Pitch, Based on Local Blade Flow Measurements," *Wind Energy*, vol. 8, pp. 67–80, 2004.

[24] C. C. v. D. Scott J. Johnson and D. E. Berg, "Active Load Control Techniques for Wind Turbines," Report 2008-4809, Sandia National Laboratories, 2008.

[25] R. Wood, "A Discussion of Aerodynamic Control Effectors (ACEs) for Unmanned Air Vehicles UAVs," *AIAA*, vol. 40, no. 2002-3495, 2002.

[26] S. Farthing, "Optimal, robust, and benign horizontal and vertical axis wind turbines," *Proc. IMechE Vol. 221 Part A: J. Power and Energy*, May 2007.

[27] N. K. Jaesuk Yang, Balakrishnan Ganesh, "Radial Flow Measurements Downstream of Forced Dynamic Separation on a Rotor Blade," *AIAA*, vol. 2006-3377, 2006.

[28] *Vortex Blades*, (Los Angeles, CA), June 4 2007.

[29] *Computational Investigations of Small Deploying Tabs and Flaps for Aerodynamic Load Control*, vol. 75, 2007.

[30] K. S. J.P. Baker and C. van Dam, "Two-Dimensional Wind Tunnel and Computational Investigation of a Microtab Modified Airfoil," *J. of Aircraft*, vol. 44, pp. 563–572, Mar-Apr 2007.

[31] W. Perring and G. Douglas, "Wind tunnel experiments on the effect on the maximum lift of withdrawing and discharging air from the upper surface of an aerofoil," Reports and Memoranda 1100 (Ae. 278), Aeronautical Research Committee, April 1927.

[32] A. de Graffenried, "Boundary-Layer-Growth Suppression: 18th Applied Aerodynamics Conference (Denver, Colorado, 14-17 August 2000)," *AIAA*, vol. 38, August 2000.

[33] A. A. Hassan and E. A. Munts, "Transverse and Near-tangent Synthetic Jets for Aerodynamic Flow Control: 18th Applied Aerodynamics Conference (Denver, Colorado, 14-17 August 2000)," *AIAA*, August 2000.

[34] T. Fric and A. Roshko, "Vortical structure in the wake of a transverse jet," *J. Fluid Mech*, vol. 279, pp. 1–47, 1994.

[35] M. H. D. Simms, S. Schreck and L. Fingersh, "NREL Unsteady Aerodynamics Experiment in the NASA-Ames Wind Tunnel: A Comparison of Predictions to Measurements," Reports and Memoranda TP-500-29494, NREL, June 2001.

[36] G.-H. Y. Jiyuan Tu and C. Liu, *Computational Fluid Dynamics: A Practical Approach*. Oxford, U.K.: Elsevier, 2012.

[37] J. Boussinesq, "Essai sur la théorie des eaux courantes," *Journal de mathématiques pures et appliquées*, vol. série 4, pp. 335–376, 1878.

[38] J. S. P.J. Wiles, T.P. Rippeth and P. Hendricks, "A novel technique for measuring the rate of turbulent dissipation in the marine environment," *Geophys. Res. Lett.*, 2006.

[39] *Turbulent Boundary Layer Separation*, vol. 21, Annual Reviews Inc., 1989.

[40] R. L. F.R. Menter and S. Völker, "Transition Modelling for General Purpose CFD Codes," *Flow, Turbulence and Combustion*, vol. 77, pp. 277–303, 2006.

[41] *The Modelling of Turbulent Flow Around Stationary and Vibrating Square Cylinders*, 1993.

[42] H. L. Langhaar, *Dimensional Analysis and Theory of Models*. John Wiley and Sons, Inc., 1951.

[43] W. S. Diehl, "The Variation of Aerofoil Lift and Drag Coefficients with Changes in Size and Speed," Technical Report NACA-TR-111, NACA, 1923.

[44] F. M. White, *Fluid Mechanics 5th ed.* McGraw-Hill, 1979.

[45] Y. Gu and Y. Ju, "Numerical simulation and analysis of periodically oscillating pressure characteristics of inviscid flow in a rolling pipe," *Frontiers in Energy*, vol. 6, no. 1, pp. 21–28, 2012.

[46] "NREL National Renewable Energy Laboratory NWTC Information Portal." https://wind.nrel.gov/airfoils/AirfoilData.html. Accessed: 2014-04-12.

[47] C. Carpenter, *Flightwise: Principles of Aircraft Flight*, vol. 1. The Crowood Press Ltd., 1996.

[48] W. McCroskey, "The Phenomenon of Dynamic Stall," Technical Memorandum 81264, NASA, March 1981.

[49] S. P. Grace, "Predicting Unsteady Aerodynamic Parameters from Airfoil Surface Pressure Measurements," tech. rep., Aerospace and Mechanical Engineering Dept., Boston University, 2011.

[50] *A Semi-Empirical Theory for the Growth and Bursting of Laminar Separation Bubbles*, vol. 1073, June 1969.

[51] S. S. O. Walter P. Wolfe, "Predicting Aerodynamic Characteristics of Typical Wind Turbine Airfoils Using CFD," Technical Report SAND96-2345, Sandia National Laboratories, September 1997.

[52] G. Bertotti, *Hysteresis in magnetism: For physicists, materials scientists, and engineers*. Academic Press, Elsevier Inc., 1998.